NTNU – Trondheim
Norwegian University of
Science and Technology

Behaviour and Modelling of Self-piercing Screw and Self-piercing Rivet Connections

An Experimental and Numerical Investigation

Petter Henrik Holmstrøm
Johan Kolstø Sønstabø

Master of Science in Mechanical Engineering
Submission date: June 2013
Supervisor: Magnus Langseth, KT
Co-supervisor: David Morin, KT

Norwegian University of Science and Technology
Department of Structural Engineering

Department of Structural Engineering
Faculty of Engineering Science and Technology
NTNU- Norwegian University of Science and Technology

ACCESSIBILITY:
OPEN

MASTER THESIS 2013

SUBJECT AREA:	DATE:	NO. OF PAGES:
CONNECTORS AND JOINTS	10062013	158

TITLE:

BEHAVIOUR AND MODELLING OF SELF-PIERCING SCREW AND SELF-PIERCING RIVET CONNECTIONS

Åtferd og modellering av sambindingar med sjølvgjengande skruar og sjølvpenetrerande naglar

BY:

Petter Henrik Holmstrøm and
Johan Kolstø Sønstabø

SUMMARY:

Accurate and reliable models of connections are essential for the design of aluminium parts in cars. Today, there exist a few models customized for self-piercing rivets (SPR), but none for self-piercing screws (SPS). This thesis presents an experimental and numerical study on the behaviour of SPR and SPS connections for different loading situations.

For the rolled base material, AA6016 in the T4 condition, uniaxial tension, plane strain tension and in-plane single shear tests were performed. The Voce isotropic hardening rule and the YLD-2004-18P anisotropic yield function were calibrated using MatPrePost. The calibration was validated by simulations of the material tests.

Cross tests in three directions, single lap-joint tests and peeling tests were performed for SPR and SPS, and a point-connector model developed for self-piercing rivets was calibrated by a reverse engineering approach based on the cross tests. Single lap-joint and peeling tests were used for validation. Forming process simulations were performed to account for initial plastic deformations in bent specimens. In all tests except for pure normal loading, failure of SPR was initiated from the top sheet, while failure of SPS was caused by pull-out from the bottom sheet in all cases. For SPR, good predictions were found, except for over-prediction of the peeling resistance. The model was not able to describe mixed tension and shear loading accurately for SPS, but other tests were well reproduced.

Static and dynamic crash box tests were performed and deformation and failure modes of SPR and SPS were characterized. The same progressive buckling mode was found in all tests. Higher force was observed for riveted crash boxes compared to the screwed. Relative movement between the sheets was observed for SPS. During dynamic testing, 7 % of the SPR and 19 % of the SPS connections failed.

Simulations of dynamic crash box tests investigated effects of forming history, yield surface and mesh size. The deformation mode was well reproduced, but the force was under-predicted with 5 % to 20 %. The simulations predicted some connection failure for SPS, but not for SPR. A more fundamental understanding of the behaviour of SPS connections is required to develop a new point-connector model. Further studies could include investigation of the effects of screw diameter, sheet thickness, sheet material, screw material and dynamic effects of the connection.

RESPONSIBLE TEACHER: Prof. Magnus Langseth

SUPERVISORS: Prof. Magnus Langseth and Dr. David Morin

CARRIED OUT AT: SIMLab, Department of Structural Engineering

SAMANDRAG PÅ NORSK:

Presise og pålitelege modellar av sambindingar er svært viktig under utviklinga av bildelar av aluminium. Nokre få modellar skreddarsydde for sjølvpenetrerande naglar (SPR) finst, men ingen for sjølvgjengande skruar (SPS). Denne oppgåva presenterar ei eksperimentell og numerisk studie på åtferda til sambindingar med SPR og SPS for ulike lastsituasjonar.

Einaksielle strekktestar, strekktestar med plan tøyning og plane skjærtestar vart gjennomførte på platematerialet, som var AA6016 med varmehandsaming T4. Voce sin isotropiske herdingsregel og den anisotropiske flytefunksjonen YLD-2004-18P vart kalibrerte med bruk av MatPrePost. Kalibreringa vart validert ved å simulere materialtestane.

Krysstestar i tre retningar, testar på enkeltoverlappa sambindingar og skrelletestar vart utførte for SPR og SPS, og ein punktsambindingsmodell som er utvikla for sjølvpenetrerande naglar vart kalibrert basert på krysstestane gjennom ei omvend utviklingsprosedyre. Testane på dei enkeltoverlappa prøvestykka og skrelletestane vart brukte til validering. Simuleringar av formingsprosessen vart gjennomførte for å ta omsyn til initielle plastiske deformasjonar i bøygde prøvestykker. Brot vart starta i topplata i alle testane med SPR, med unntak av for rein normallast, medan brot skjedde ved utdraging frå botnplata i alle testane med SPS. Gode prediksjonar vart sett for SPR, med unntak av skrellemotstanden. Modellen evna ikkje å skildre blanda strekk- og skjærlast presist for SPS, men andre testar vart godt attgjevne.

Statiske og dynamiske kræsjbokstestar vart gjennomførte og deformasjons- og feilmodar vart karakteriserte for SPR og SPS. Den same knekningsmoda vart observert i alle testane. Dei nagla kræsjboksane gav høgare kraft enn dei skrudde. I dei dynamiske testane feila 7 % av nagle- og 19 % av skruesambindingane.

Simuleringar av dei dynamiske kræsjbokstestane vart gjennomførte for å utforska effekten av formingshistoria, flytefunksjon og elementstorleik. Deformasjonsmoden vart godt attgjeven, men krafta vart under-predikert med 5 % til 20 %. Simuleringane predikerte noko brot av sambindingar for SPS, men ikkje noko for SPR. Ei meir fundamental forståing av åtferda til sambindingar med sjølvgjengande skruar er naudsynt for å utvikle ein ny punktsambindingsmodell. Vidare studiar kan mellom anna inkludere utforsking av effekten av skruediameter, platetjuknad, platematerial, skruematerial og dynamiske effektar i sambindinga.

Department of Structural Engineering
FACULTY OF ENGINEERING SCIENCE AND TECHNOLOGY
NTNU – Norwegian University of Science and Technology

MASTER THESIS 2013

for

Johan Kolstø Sønstabo and Petter Henrik Holmstrøm

Behaviour and modelling of self-piercing screw and self-piercing rivet connections

During a car accident, the body structure of a vehicle has to maintain its integrity such that minimal forces are transferred to the occupants. This means that all structural elements in the car body and the connections between them have to behave in a controlled and reliable manner. Seam or spot welding, riveting, clinching or self-piercing screws are some of the joining techniques used today by the car makers.

In the design process numerical simulations are extensively used by the automotive industry to optimise the performance of a vehicle. This requires, however, robust and reliable models of the connectors between the different elements in order to reproduce real life behaviour of the car body for instance in a crash situation. However, for self-piercing screws no models for large scale shell analyses are available which represent the behaviour under a combination of axial and shear loading. Thus a fundamental study is needed based on tests, modelling and numerical simulations to establish a basis for improved engineering models of self-piercing screw connectors.

The experimental and numerical results for self-piercing screws will be compared with data obtained using self-piercing rivets. In this study focus will be placed on connections between aluminium sheets.

The following plan for the project is proposed:

Material testing of the chosen aluminium alloys.
Single screw/rivet specimen tests in order to reveal the mechanical behaviour at different loading conditions.
Calibration and validation of engineering models for large scale shell analyses.
Validation of the model by using benchmark tests.

Supervisors: Magnus Langseth and David Morin from SIMLab

The thesis must be written according to current requirements and submitted to the Department of Structural Engineering, NTNU, no later than June 10th, 2013.

NTNU, January 14th, 2013

Magnus Langseth
Professor

Preface

This master's thesis was written for the Centre for Research-Based Innovation (CRI) SIMLab hosted by Department of Structural Engineering, Norwegian University of Science and Technology. The extent of the work was 20 working weeks and 30 educational points.

The objective of the work was firstly to investigate the behaviour of self-piercing screw and self-piercing rivet connections for different loading situations. Secondly, finite element models of the tests were established, and simulations were compared to experimental data using an existing point-connector model developed for self-piercing rivets.

Firstly, we would like to thank our main supervisor Professor Magnus Langseth, for his constructive and encouraging response to our work. A special thank is directed to our co-supervisor Dr. David Morin, for his massive support and enthusiastic approach to our work. We are looking forward to further collaboration in the future. We would also like to thank Chief Engineer Trond Auestad and Mechanic Tore Wist for their support in the laboratory. Additionally, the help from Dr. Hoang Hieu on the experimental work has been much appreciated.

The aluminium sheets were provided by Hydro Aluminium Bonn (Germany).

Contents

List of Figures

List of Tables

List of Abbreviations

C test	Cross test
C-0 test	Cross test in 0 degree loading direction
C-45 test	Cross test in 45 degree loading direction
C-90 test	Cross test in 90 degree loading direction
CB	Crash box
EqB	Equi-biaxial
HT	Heat treatment
ISS test	In-plane single shear test
P test	Peeling test
PST test	Plane strain tensile test
R-ratio	Strain ratio
r-ratio	Flow stress ratio
SLJ test	Single lap-joint test
SPR	Self-piercing rivet
SPS	Self-piercing screw
UT test	Uniaxial tension test
WOHT	Without heat treatment

Chapter 1

Introduction

Self-piercing rivet and self-piercing screw connections are extensively used to join aluminium parts of load bearing structures in cars. Under impact loading, the behaviour and fracture of connections play an important role of the energy absorption process and the subsequent passenger safety. Therefore, comprehension of the behaviour of the connections is crucial for designing safe cars. Finite element simulations are vital in this design process. To accurately predict the behaviour of the connections, the designers are depending on reliable models.

Many experimental and theoretical studies have been performed on the mechanical properties and behaviour of connections, e.g. [1–7]. For self-piercing rivets and particularly self-piercing screws, only a limited amount of publications concerning the behaviour and fracture is found in the literature. Experimental and numerical investigation of the self-piercing riveting procedure [8] and the behaviour of self-piercing rivet connections under various loading conditions [9–11] have been carried out. Among experimental studies on screw connections are [1, 3], but none concerning self-piercing screws. Hence, a fundamental study on the behaviour of self-piercing screw connections is needed.

In the automotive industry, shell formulations are usually adopted to keep the computational time at acceptable levels. Different techniques are used to represent point-connections for crash applications. According to Hanssen [12], these include node-to-node, node-to-surface and surface-to-surface constraints using contact formulations, or a more direct approach using discrete elements, beam elements or brick elements. Sommer et al. [13] investigated the possibility of modelling self-piercing rivets using implemented models in LS-DYNA, and found one hexahedron element combined with a specific material model as the most promising choice. Among the studied models were a spotweld model proposed by Seeger et al. [14] and a model customized for self-piercing rivet connections proposed by Hanssen et al. [12]. For self-piercing screw connections, however, no specifically designed model currently exists.

In this work an extensive experimental investigation was performed on the behaviour and fracture of self-piercing rivets and self-piercing screws under different loading conditions. Subsequently, the ability of the self-piercing rivet model of Hanssen et al. [12] to describe

the behaviour of the self-piercing rivet and self-piercing screw connections was assessed.

The experimental program was divided into three parts. In the first part, material tests were carried out in order to calibrate and validate the constitutive model used to model the base material. The 18 parameter anisotropic yield criterion proposed by Barlat et al. [15] was used together with the 7 parameter Voce isotropic hardening rule and isotropic elasticity. The second part consisted of tests of the self-piercing rivet and self-piercing screw connections at the unit level. The results from these tests were used to calibrate and validate the rivet model of Hanssen et al. [12] for both rivets and screws. In the third part, component tests were performed. The component tests consisted of static and dynamic crushing of top-hat sections connected with self-piercing rivets or self-piercing screws. The motivation for the component tests was firstly to investigate the behaviour and fracture of self-piercing rivet and self-piercing screw connections in a complex dynamic non-controlled loading situation, and secondly to investigate the ability of the combined material and point-connector model to reproduce the experimental tests.

The novelty of this work is related to self-piercing screws, including experimental tests, calibration of a point-connector model and an extensive comparison with self-piercing rivets. Results from this study may be used in further work in development of point-connector models.

Chapter 2

Theory

In this chapter the theory most relevant for this thesis is presented. Firstly, a brief presentation of some joining techniques commonly used by the automotive industry is given, with emphasis on the techniques used in this work. Secondly, the point-connector model used for self-piercing rivet (SPR) and self-piercing screw (SPS) connections is described in detail. The third part covers the base material, and the chapter is concluded by a presentation of theory relevant for modelling of materials, and details of applied models.

2.1 Connections

In this section some joining techniques commonly used to join aluminium parts in the body structure of cars are presented. In general, this includes mechanical and thermal joining techniques, as well as adhesive bonding technology. Emphasis is put on self-piercing riveting and self-piercing screwing, which are the joining techniques used in this study. Some other techniques are briefly presented.

In Figure 2.1, some joining techniques used in the body of the Audi A8 '10 are shown. As illustrated, the choice of joining technique depends on the particular joining problem. All techniques have different advantages and disadvantages with respect to assembly, strength, ductility, durability, corrosion, cost etc. The following presentation of joining techniques is mainly based on [16].

Welding is traditionally the most common way to join sheets in the automotive industry. Many welding techniques exist, and a few are highlighted here. Resistance welding is a group of welding techniques which utilize the heat generated by resistance to electrical current. No fillers or fluxes are used. Spot welding is the most common resistance welding technique for aluminium. In general, resistance welding of aluminium is a challenge due to low electrical and thermal resistance. Another family of welding techniques is called arc welding, where the two materials are heated and melted by an electrical arc between the electrode and the material. In the automotive industry, metal inert gas (MIG) welding

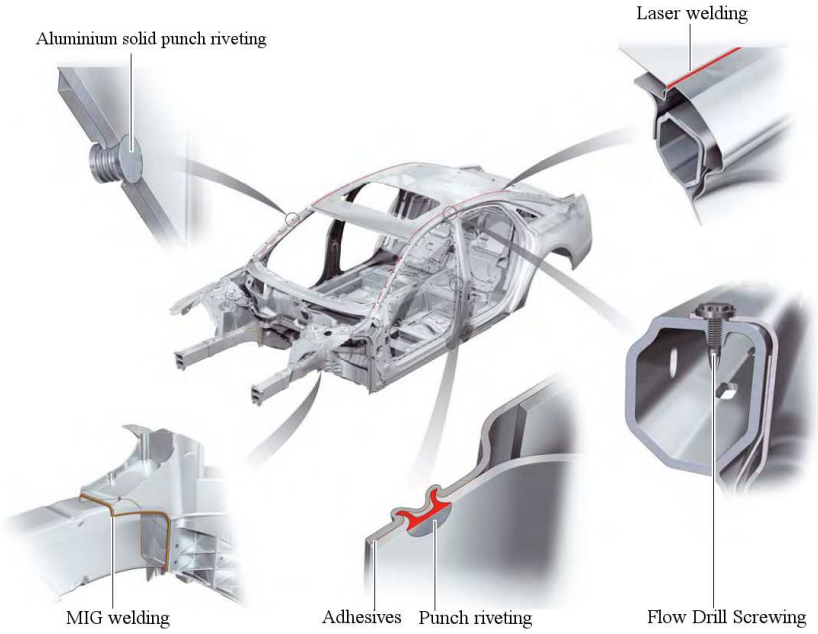

Figure 2.1: Joining techniques used to join the body in Audi A8 '10 [17].

(see Figure 2.1) with a consumable electrode is often applied. Advantages of this technique include one-sided access and high strength of the connection. Among the disadvantages are heat affected material and slow process speed. A third technique is laser welding (see Figure 2.1), where a beam provides a concentrated heat source. The technique allows for narrow and deep welds, and is suitable for large-scale production. Advantages include high static and dynamic strength, one-sided access and improved structural stiffness.

Adhesive bonding technology is increasingly used for sheet joining, often combined with resistance spot welds and mechanical fastening (see Figure 2.1). The main advantages are increased stiffness and fatigue strength. Additionally, adhesive bonding is effective for corrosion protections, as the materials in contact are superficially insulated. This is particularly important when joining dissimilar materials. Adhesive bonding is also used for strengthening of seem joints and noise reduction [18].

Examples of mechanical fastening techniques for sheets include punch riveting, solid punch riveting, screwing, bolting, clinching and press joining. Clinching is a technique where the two sheets are pressed by a punch into a die such that the material form an interlocking joint. The technique is most often used in parts were strength is not a major concern, such as around the rear wheel [18]. In solid punch riveting (see Figure 2.1), the rivet is pressed through both sheets, which makes the technique well-suited for thin metal components.

The first joining technique used in this study is self-piercing riveting (denoted punch riveting in Figure 2.1). The technique is an increasingly adopted alternative to spot welding, and has become important in joining aluminium parts in modern cars. Advantages of this technique include no need for pre-drilling, high strength, water and air tightness,

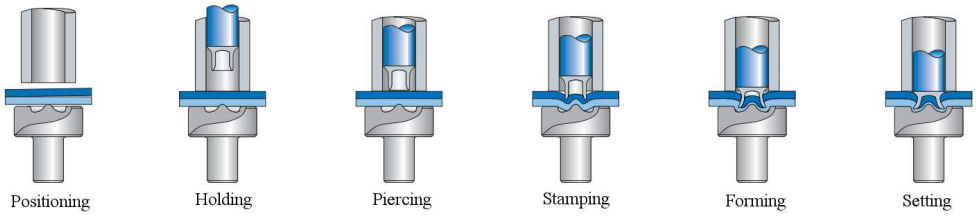

Figure 2.2: Stages of the self-piercing riveting process [19].

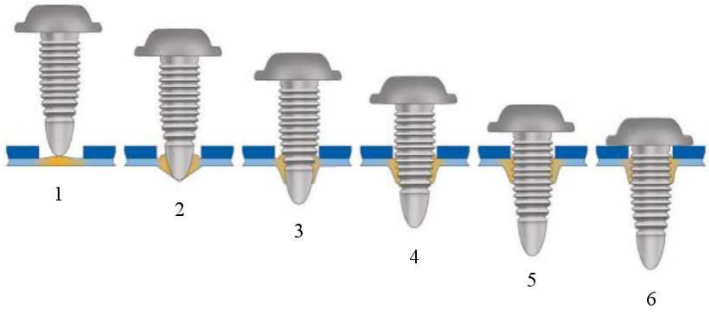

Figure 2.3: Stages of the self-piercing screwing process [20].

no thermal influence and possible joining of dissimilar materials with various strengths and thicknesses [19]. A disadvantage is that two-sided access is necessary in the joining process. The six stages of the self-piercing riveting procedure are illustrated in Figure 2.2.

The second joint used in this study is self-piercing screws (denoted flow drill screws in Figure 2.1). This is a rather new joining technique in the automotive industry, but is frequently adopted for certain applications. Advantages include no need for pre-drilling of the bottom sheet, one-sided assembly, free positioning, high strength, possible disassembly and torque resistance [20]. The screwing process consists of six stages which are shown in Figure 2.3. Explanation of the different stages are listed below.

1. Warming the sheet metal by end load and high rotational speed
2. Penetration into the material
3. Forming of the draught on the reverse side of the material stack
4. Thread forming of the material (rotational speed reduced)
5. Full thread engagement
6. Tightening

2.2 Modelling of connections

Accurate and reliable modelling of connections is important for the automotive industry. An essential concern is the computational time compared to accuracy and reliability. The point-connector model used to model the self-piercing rivets and the self-piercing screws is a state of the art large-scale finite element model developed for self-piercing rivets at SIMLab at NTNU, proposed by Hanssen et al. [12]. Throughout this thesis, the model is referred to as *the point-connector model*.

2.2.1 A point-connector model for self-piercing rivets

The point-connector model is a local model that describes the resistance of the rivet for the given loading condition. The user specifies which sheets to connect, the total thickness of the two sheets, a node defining the centre of the connection and a numerical diameter. The diameter should approximately equal the diameter of the rivet. The algorithm then searches for a set of nodes on the opposing shell segments within the user-specified diameter from the centre node. These nodes constitute the domain of influence, according to Figure 2.4. The forces and moments transferred between the nodes on the opposing shell segments are computed according to the local model at each time step. Some illustrations of the SPR configuration are shown in Figure 2.5.

Two assumptions concerning the description of the local model are made. Firstly, a single-sheet rivet system is assumed. That is, the movement (translation and rotation) of the rivet follows the movement of the master sheet. The slave sheet is the sheet of which the rivet is torn out, the master sheet is the sheet to which it is attached, see Figure 2.5a. Note that the top sheet is not necessarily the master sheet. Secondly, all considerations of the local model are done in the plane of maximum opening, defined by the unit normal vector $\hat{\boldsymbol{n}}_0 = \hat{\boldsymbol{n}}_s \times \hat{\boldsymbol{n}}_m$, where $\hat{\boldsymbol{n}}_s$ and $\hat{\boldsymbol{n}}_m$ are the unit normal vectors of the slave and master sheets, respectively. The plane of maximum opening and the unit vectors are shown in Figure 2.5a, together with the slave and master sheet.

The kinematics of the SPR connection are shown in Figure 2.5b and 2.5c. The tangential unit normal vector of the rivet $\hat{\boldsymbol{n}}_t$ is defined as $\hat{\boldsymbol{n}}_t = \hat{\boldsymbol{n}}_0 \times \hat{\boldsymbol{n}}_m$. The position vector of the

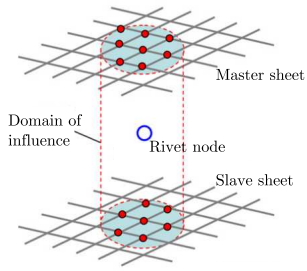

Figure 2.4: Rivet node between master and slave sheet.

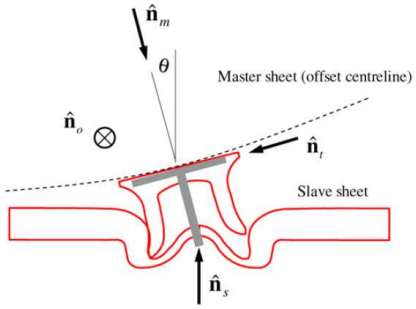

(a) Plane of maximum opening with unit vectors.

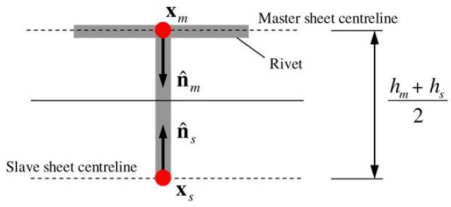

(b) Simplified SPR illustration.

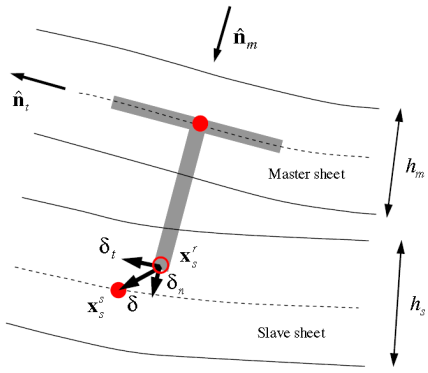

(c) Deformation measures of local point-connector model.

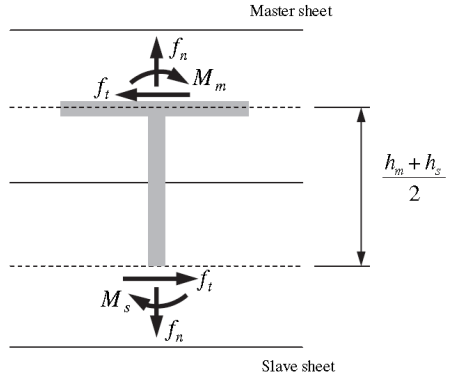

(d) Forces acting on the rivet in the plane of maximum opening.

Figure 2.5: Illustration of the SPR configuration. [12]

rivet's master end is denoted $\boldsymbol{x}_m$ and the initial position vector of the rivet's slave end is denoted $\boldsymbol{x}_s$. The rivet's master end is fixed to the deformation of the master sheet while the slave end can move relative to the slave sheet. The position vector of the rivet's slave end in the deformed configuration is denoted $\boldsymbol{x}_s^r$ while the position vector of the slave sheet in the deformed configuration is denoted $\boldsymbol{x}_s^s$. For time $t = 0$, $\boldsymbol{x}_s^r = \boldsymbol{x}_s^s = \boldsymbol{x}_s$.

According to Figure 2.5c, three local deformation vectors are defined; the normal stretch $\boldsymbol{\delta}_n$, the tangential stretch $\boldsymbol{\delta}_t$ and the total stretch $\boldsymbol{\delta} = \boldsymbol{\delta}_n + \boldsymbol{\delta}_t$. The total stretch is given by $\boldsymbol{\delta} = \boldsymbol{x}_s^r - \boldsymbol{x}_s^s$, which means that the lengths (magnitudes) of the normal and tangential stretch may be computed as $\delta_n = \boldsymbol{\delta}_n \cdot \hat{\boldsymbol{n}}_m$ and $\delta_t = \boldsymbol{\delta}_t \cdot \hat{\boldsymbol{n}}_t$, respectively.

The resultant forces and moments are reduced to zero when the rivet fails. The forces acting on the rivet are shown in Figure 2.5d. The normal and tangential resultant forces are denoted f_n and f_t, and the moments at the master and slave ends are denoted M_m and M_s, respectively. A simple moment balance gives that the relation

$$M_s = \frac{h_m + h_s}{2} f_t - M_m \tag{2.1}$$

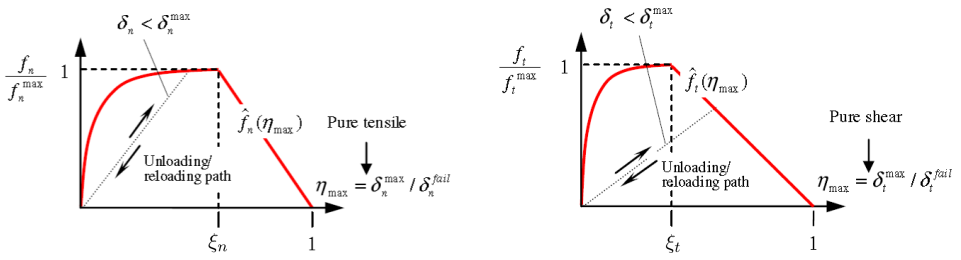

(a) Pure normal deformation. (b) Pure shear deformation.

Figure 2.6: Local force-displacement relationship for pure normal and pure shear deformation. [12].

must hold at all times. Here, h_m and h_s are the thickness of the master and slave sheet, respectively.

A local force-deformation relationship for pure normal and pure shear deformation in the plane of maximum opening is defined as

$$\frac{f_n}{f_n^{max}} = \frac{\delta_n}{\eta_{max}\delta_n^{fail}}\hat{f}_n(\eta_{max}) \tag{2.2}$$

$$\frac{f_t}{f_t^{max}} = \frac{\delta_t}{\eta_{max}\delta_t^{fail}}\hat{f}_t(\eta_{max}) \tag{2.3}$$

The parameters f_n^{max} and f_t^{max} are the maximum forces acting on the rivet when failure occurs for pure normal and pure shear loading, respectively. δ_n^{fail} and δ_t^{fail} are the corresponding deformations at failure. η_{max} is a damage measure defined by Equation (2.6) through (2.10). The dimensionless force-deformation functions $\hat{f}_n(\eta_{max})$ and $\hat{f}_t(\eta_{max})$ are defined by

$$\hat{f}_n(\eta_{max}) = \begin{cases} 1 - \left(\frac{\xi_n - \eta_{max}}{\xi_n}\right)^8 & \text{for} \quad \eta_{max} \leq \xi_n \\ 1 - \frac{\eta_{max} - \xi_n}{1 - \xi_n} & \text{for} \quad \eta_{max} > \xi_n \end{cases} \tag{2.4}$$

$$\hat{f}_t(\eta_{max}) = \begin{cases} 1 - \left(\frac{\xi_t - \eta_{max}}{\xi_t}\right)^8 & \text{for} \quad \eta_{max} \leq \xi_t \\ 1 - \frac{\eta_{max} - \xi_t}{1 - \xi_t} & \text{for} \quad \eta_{max} > \xi_t \end{cases} \tag{2.5}$$

The parameters ξ_n and ξ_t define where softening starts. Equation (2.2) and (2.3) are plotted in Figure 2.6.

For pure normal loading $\eta_{max} = \frac{\delta_n^{max}}{\delta_n^{fail}}$ and for pure shear loading $\eta_{max} = \frac{\delta_t^{max}}{\delta_t^{fail}}$, such that η_{max} grows from 0 to 1. δ_n^{max} and δ_t^{max} are the maximum values that have ever occurred for δ_n and δ_t, respectively. Thus, monotonic loading is defined by $\delta_n = \delta_n^{max}$ and $\delta_t = \delta_t^{max}$. In this case the multipliers $\frac{\delta_n}{\eta_{max}\delta_n^{fail}}$ and $\frac{\delta_t}{\eta_{max}\delta_t^{fail}}$ in Equation (2.2) and (2.3) are unity. For monotonic pure normal and pure shear loading, Equation (2.4) and (2.5) therefore provide the non-linear capacities of the rivet. For non-monotonic loading

conditions, e.g. unloading, the model provide a linear force-deformation behaviour. In this case η_{max}, $\hat{f}_n(\eta_{max})$ and $\hat{f}_t(\eta_{max})$ are constant in addition to the fixed parameters δ_n^{fail} and δ_t^{fail}.

The damage measure η_{max} is calculated at every time step and provides the rivet's resistance in terms of the orthogonal normal and shear forces. Generally, the damage measure is given by

$$\eta_{max}(t) = \max(\eta(t)) \tag{2.6}$$

where $\eta(t)$ is called the effective displacement. Thus, η_{max} is the largest value η has taken in the simulation.

Hanssen et al. [12] observed the deformation capacity of the rivet to be dependent of the loading angle. Of this reason they argued that a loading angle dependency should be included in the expression for the effective damage measure η. In the model η is defined as

$$\eta = \left[\xi + \frac{1-\xi}{\alpha}\right]\sqrt{\left(\frac{\delta_n}{\delta_n^{fail}}\right)^2 + \left(\frac{\delta_t}{\delta_t^{fail}}\right)^2} \tag{2.7}$$

Here, ξ is a loading angle dependent parameter calculated by

$$\xi = 1 - \frac{27}{4}\left(\frac{2\theta}{\pi}\right)^2 + \frac{27}{4}\left(\frac{2\theta}{\pi}\right)^3 \tag{2.8}$$

where θ is the loading angle given by

$$\theta = \arctan\left(\frac{\delta_n}{\delta_t}\right) \tag{2.9}$$

In order to increase the model flexibility, an accumulated damage dependency is included such that the loading angle dependency gets damage dependent. This is done through the parameter α in Equation (2.7). The α parameter is defined by the piecewise linear relationship

$$\alpha = \begin{cases} \frac{\xi_t - \eta_{max}}{\xi_t}\alpha_1 + \frac{\eta_{max}}{\xi_t}\alpha_2 & \text{for} \quad \eta_{max} < \xi_t \\ \frac{1-\eta_{max}}{1-\xi_t}\alpha_2 + \frac{\eta_{max}-\xi_t}{1-\xi_t}\alpha_3 & \text{for} \quad \eta_{max} \geq \xi_t \end{cases} \tag{2.10}$$

As seen, the α parameter first grows from an initial value α_1 to a value α_2 when softening starts and then to the final value α_3.

In Figure 2.7 iso-lines for $\eta(\theta) = const.$ is illustrated in the δ_n-δ_t plane. This shows the evolution of effective displacement η as function of loading direction θ and current value of the damage measure η_{max}. Ultimate failure of the rivet is reached when η_{max} reaches unity. At this point Equation (2.2) and (2.3) give no resistance to deformation.

Before softening starts in Equation (2.2) and (2.3) the moments are equally distributed to the master and slave ends. However, when the damage grows the moment is gradually transferred from the slave end to the master end. This is governed by the relations

$$M_m = \begin{cases} \frac{h_m + h_s}{4} f_t & \text{for} \quad \eta_{max} < \xi_t \\ \frac{h_m + h_s}{4}\left(1 + \frac{\eta_{max} - \xi_t}{1-\xi_t}\right) f_t & \text{for} \quad \eta_{max} \geq \xi_t \end{cases} \tag{2.11}$$

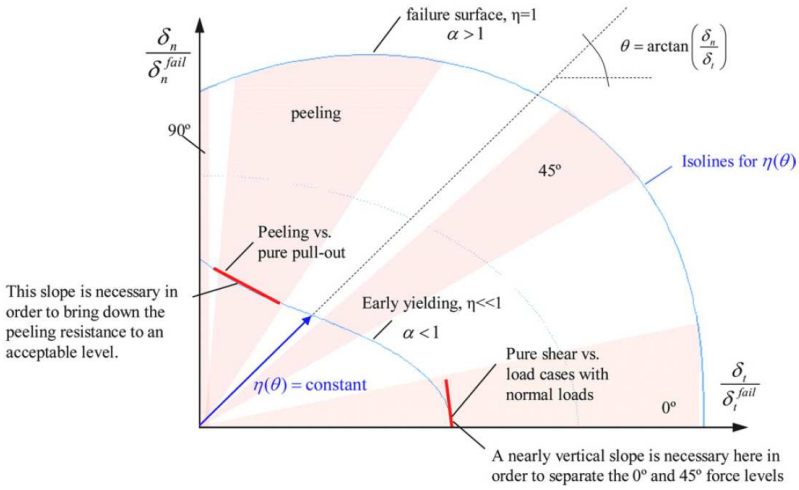

Figure 2.7: Discussion of effective displacement [12].

Table 2.1: Parameters of the point-connector model.

Symbol	Description
f_n^{max}	Maximum pure normal force
f_t^{max}	Maximum pure shear force
δ_n^{fail}	Deformation at failure for pure normal deformation
δ_t^{fail}	Deformation at failure for pure shear deformation
ξ_n	Where softening starts for pure normal deformation
ξ_t	Where softening starts for pure shear deformation
α_1	Initial value of the damage parameter α
α_2	Value of α when softening starts
α_3	Final value of α

and

$$M_s = \begin{cases} \frac{h_m+h_s}{4} f_t & \text{for} \quad \eta_{max} < \xi_t \\ \frac{h_m+h_s}{4} \left(1 - \frac{\eta_{max}-\xi_t}{1-\xi_t}\right) f_t & \text{for} \quad \eta_{max} \geq \xi_t \end{cases} \tag{2.12}$$

which satisfy Equation (2.1).

This concludes the local model description. The parameters to be determined are summarized in Table 2.1, and are identified using a reverse engineering approach. In reverse engineering simulations are performed iteratively, and the model parameters are adjusted such that the simulation results fit the experimental data. Experimental data constrain the fracture locus in Figure 2.7 during the calibration.

Table 2.2: Chemical composition of the AA6016 aluminium alloy.

Element	wt%
Si	$1.0 - 1.5$
Fe	< 0.50
Cu	< 0.20
Mn	< 0.20
Mg	$0.25 - 0.6$
Cr	< 0.10
Zn	< 0.20
Ti	< 0.15
Others	< 0.15
Al	Rem.

2.3 Base material

The material used in this work is an AA6016-T4 aluminium alloy, where the denotion T4 indicates that the material has been solution heat treated and naturally aged. Aluminium alloys typically have high ductility, relatively high strength, excellent corrosion resistance and low density [21]. Due to these properties, aluminium alloys have in the recent years been increasingly used by the automotive industry in energy-absorbing structures and more recently also in load-carrying structures, motivated by increasing concerns for economy, environment and functionality [22].

Aluminium is a polycrystalline material with a face-centred cubic (FCC) crystal structure. The FCC crystal structure has 12 unique slip systems where dislocation motion is most likely to occur, which explains aluminium's relatively high ductility [21]. The chemical composition of the AA6016 alloy, according to [23], is given in terms of weight percent (wt%) in Table 2.2.

Mechanical properties such as resistance against plastic deformation depend to some extent on the size and shape of the grains in the crystalline material. The AA6016 sheets were obtained by a rolling process. During rolling grains are elongated in the rolling direction and compressed in the thickness direction. For this reason rolled materials often exhibit different mechanical response for different loading directions; they are anisotropic. According to [24], the strain rate sensitivity of AA6016 in the T4 condition is negligible.

2.4 Modelling of base material

This section concerns the theory relevant for modelling the base material. Firstly, the general concepts of a yield function is discussed with emphasis on features relevant for this work. Subsequently, the particular yield function chosen to represent the behaviour of the base material is presented. Then, some general considerations concerning work hardening and the chosen hardening rule is presented. The section is finalized with some comments on the yield function.

2.4.1 The concepts of a yield function

Deformations occur when a body is subjected to forces. Depending on the stress level the deformations are either elastic or plastic. Irreversible plastic deformations start to occur at a certain stress level limit, which is called the yield stress. Stresses below the yield stress are elastic. The yield stress is defined by the yield criterion, which is mathematically formulated as

$$f(\boldsymbol{\sigma}) = 0 \tag{2.13}$$

where f is the yield function. The fulfilment of the yield criterion is a required condition for yielding of the material. Generally, the yield function is assumed to be a continuous function of the Caucy stress tensor $\boldsymbol{\sigma}$ and takes on negative values for elastic deformations. For some applications, the yield function may be dependent of certain parts rather than the complete stress tensor. For instance, if the yield function is assumed to be independent of hydrostatic pressure, it exclusively becomes a function of the deviatoric part of the stress tensor.

Geometrically, f may be considered as a surface enclosing the elastic domain of the six-dimensional stress space. This surface is called the yield surface, and is often visualized in the two- or three-dimensional principal stress space. The elastic domain is defined by $f(\boldsymbol{\sigma}) < 0$, the plastic domain is defined by $f(\boldsymbol{\sigma}) = 0$, while $f(\boldsymbol{\sigma}) > 0$ is inadmissible for rate-independent plasticity.

For convenience, the yield criterion may be written on the form

$$f(\boldsymbol{\sigma}) = \phi(\boldsymbol{\sigma}) - \sigma_Y = 0 \tag{2.14}$$

where $\phi(\boldsymbol{\sigma}) = \sigma_{eq}$ is a scalar measure of the current stress state, denoted the equivalent stress, and σ_Y is the yield stress.

Generally, the stress tensor $\boldsymbol{\sigma}$ is a function of the strain tensor $\boldsymbol{\epsilon}$. The strain tensor is, however, often decomposed additively into an elastic and a plastic part,

$$\boldsymbol{\epsilon} = \boldsymbol{\epsilon}^e + \boldsymbol{\epsilon}^p \tag{2.15}$$

where $\boldsymbol{\epsilon}^e$ and $\boldsymbol{\epsilon}^p$ are the elastic and plastic strain tensors.

To not violate the second law of thermodynamics, the plastic dissipation must be ensured non-negative. That is,

$$\mathfrak{D}_p = \boldsymbol{\sigma}\dot{\boldsymbol{\epsilon}}^p \geq 0 \tag{2.16}$$

where $\mathfrak{D}_p$ is the plastic dissipation and $\dot{\boldsymbol{\epsilon}}^p$ is the rate of change of the plastic strain tensor. The superimposed dot implies time differentiation. $\mathfrak{D}_p$ is assumed to be dissipated as heat.

While Equation (2.14) constitutes the conditions for plastic flow, the direction of the plastic strain increment must be determined in order to ensure fulfilment of Equation (2.16). The plastic flow rule defines the plastic strain rate tensor $\dot{\boldsymbol{\epsilon}}^p$ as

$$\dot{\boldsymbol{\epsilon}}^p = \dot{\lambda}\boldsymbol{h} \tag{2.17}$$

where $\dot{\lambda}$ is the plastic multiplier and $\boldsymbol{h}$ is the so-called flow function. $\dot{\lambda}$ is a non-negative scalar which adjusts the size of the plastic strain increment. It is common to assume

that $\boldsymbol{h}$ may be derived from a plastic potential function G, such that the flow function $\boldsymbol{h}$ equals the gradient of the potential function in the stress space,

$$\boldsymbol{h} = \frac{\partial G}{\partial \boldsymbol{\sigma}} \tag{2.18}$$

The potential function $G \geq 0$ is assumed to be a scalar valued function of the stress tensor $\boldsymbol{\sigma}$. Equation (2.17) now reads

$$\dot{\boldsymbol{\epsilon}}^p = \dot{\lambda}\frac{\partial G}{\partial \boldsymbol{\sigma}} \quad \Leftrightarrow \quad \mathrm{d}\boldsymbol{\epsilon}^p = \mathrm{d}\lambda\frac{\partial G}{\partial \boldsymbol{\sigma}} \tag{2.19}$$

Hence, the plastic strain increment $\mathrm{d}\boldsymbol{\epsilon}^p$ has the same direction as the gradient of the of the plastic potential function $\frac{\partial G}{\partial \boldsymbol{\sigma}}$. The length of the increment is adjusted by $d\lambda$. Drucker [25] (as cited by [26]) proved that in order to ensure non-negative plastic dissipation, the plastic potential function must constitute a convex surface.

In many cases the yield function itself may be used as plastic potential. In this case, the flow is called associated, and the flow rule takes the form

$$\dot{\boldsymbol{\epsilon}}^p = \dot{\lambda}\frac{\partial f}{\partial \boldsymbol{\sigma}} \quad \Leftrightarrow \quad \mathrm{d}\boldsymbol{\epsilon}^p = \mathrm{d}\lambda\frac{\partial f}{\partial \boldsymbol{\sigma}} \tag{2.20}$$

Since a strain increment in Equation (2.20) is proportional to the gradient of the yield function in the stress space, the associated flow rule implies normality. That is, the plastic strain increment vector is directed along the outward normal vector of the yield surface. To ensure that the scalar product of all possible combinations of $\boldsymbol{\sigma}$ and $\dot{\boldsymbol{\epsilon}}^p$ is non-negative (Equation (2.16)), the yield function f must constitute a convex surface. However, if the yield function is not used as plastic potential, the flow rule retains on the form in Equation (2.19). In this case the flow is called non-associated.

The physical phenomenon causing plastic flow in metals is mainly dislocation motion in slip systems in the material. Bishop and Hill [27] (as cited by [15]) showed that for a single crystal where dislocation glide occurs when the resolved shear stress on a slip system reaches a critical value (Schmid law), the resulting yield surface was convex and the associated strain increment was normal to it. It is noteworthy that Spitzig et al. [28,29] (as cited by [15]) conducted experiments under hydrostatic confinement and concluded that plastic flow was not normal to the yield surface; the flow was non-associated. However, the differences observed were negligible compared to results were associated flow was assumed. Thus, normality is assumed to be a good approximation for low to medium strength metals and low hydrostatic pressures.

For a stress state located on the yield surface it is necessary to distinguish between elastic unloading and plastic loading. The Kuhn-Tucker conditions constitutes the constraints for when plastic flow may occur. They read

$$f \leq 0, \quad \dot{\lambda} \geq 0, \quad \dot{\lambda} f = 0 \tag{2.21}$$

For elastic loading $f < 0$ and $\dot{\lambda} = 0$. Plastic flow may only occur when the stress state is located on the yield surface, i.e. $f = 0$ and $\dot{\lambda} \geq 0$. The case $f = 0$ and $\dot{\lambda} = 0$ occurs

for elastic unloading from a plastic state. During plastic flow f is constantly equal zero, which implies $\dot{f} = 0$. This leads to the consistency condition

$$\dot{\lambda}\dot{f} = 0 \tag{2.22}$$

For rate-independent plasticity, the consistency condition is used to derive expressions for the plastic multiplier $\dot{\lambda}$. The plastic strain increment is then computed by applying the flow rule.

In the case of associated flow, the plastic multiplier $\dot{\lambda}$ may be interpreted as an equivalent plastic strain rate $\dot{\epsilon}^p_{eq}$. The equivalent, or accumulated, plastic strain may then be computed as $\epsilon^p_{eq} = \int \dot{\epsilon}^p_{eq} dt$. The equivalent plastic strain ϵ^p_{eq} is defined to be work conjugate to the equivalent stress σ_{eq}, such that

$$\sigma_{eq}\dot{\epsilon}^p_{eq} = \boldsymbol{\sigma}\dot{\boldsymbol{\epsilon}}^p \tag{2.23}$$

A material where the mechanical properties are identical in all directions is called isotropic. If this is not the case, the material is anisotropic. An anisotropic yield function takes on unequal values of the yield stress for different material orientations.

For further details on material mechanics and plasticity theory, the readers are encouraged to look up e.g. Lubliner [30].

2.4.2 YLD-2004-18P anisotropic yield function

The YLD-2004-18P yield function proposed by Barlat et al. [15] was chosen to represent the behaviour of the aluminium sheets. Henceforth, the YLD-2004-18P yield function is referred to as *the Barlat yield function*. The yield function is rate independent and pressure insensitive, and orthotropic anisotropy is taken into account. As stated by Moore et al. [24], the strain rate sensitivity of AA6016-T4 is negligible, which justifies the choice of applying rate independent plasticity. Orthotropy is a special case of anisotropy, often seen in rolled and extruded materials, where three mutually orthogonal symmetry planes are present. The yield function is based on linear transformations of the stress deviator and depends on 18 coefficients.

In general, a pressure independent, isotropic yield function takes the form

$$f = f(\boldsymbol{S}) \tag{2.24}$$

where $\boldsymbol{S}$ represents the principal values of the stress deviator $\boldsymbol{s}$. A tensor $\tilde{\boldsymbol{s}}$ is obtained by a linear transformation of the deviator $\boldsymbol{s}$, such that

$$\tilde{\boldsymbol{s}} = \boldsymbol{C}\boldsymbol{s} \tag{2.25}$$

where the transformation tensor $\boldsymbol{C}$ has constant coefficients. The coefficients of $\boldsymbol{C}$ weigh the components of $\boldsymbol{s}$ to account for anisotropy. The principal values of $\tilde{\boldsymbol{s}}$ are denoted $\tilde{\boldsymbol{S}}$ and may be found by solving for the roots of the characteristic equation of $\tilde{\boldsymbol{s}}$. Details of this are found in [15]. By substituting $\tilde{\boldsymbol{S}}$ for $\boldsymbol{S}$ in Equation (2.24), an anisotropic yield

function $f = f(\tilde{\boldsymbol{S}})$ is defined. Generally, an arbitrary number of linear transformations could be included to increase the number of anisotropy coefficients.

For the Barlat yield function, two such linear transformations are done,

$$\tilde{\boldsymbol{s}}' = \boldsymbol{C}'\boldsymbol{s} \tag{2.26a}$$

$$\tilde{\boldsymbol{s}}'' = \boldsymbol{C}''\boldsymbol{s} \tag{2.26b}$$

By performing two linear transformations, the yield function has six arguments,

$$f = f\left(\tilde{\boldsymbol{S}}', \tilde{\boldsymbol{S}}''\right) = f\left(\tilde{S}'_1, \tilde{S}'_2, \tilde{S}'_3, \tilde{S}''_1, \tilde{S}''_2, \tilde{S}''_3\right) \tag{2.27}$$

Again, the principal values $\tilde{S}'_i$ and $\tilde{S}''_i$ are found by solving the characteristic equations of the tensors $\tilde{\boldsymbol{s}}'$ and $\tilde{\boldsymbol{s}}''$. The proposed yield function reads

$$\begin{aligned} f = f\left(\tilde{\boldsymbol{S}}', \tilde{\boldsymbol{S}}''\right) = &|\tilde{S}'_1 - \tilde{S}''_1|^m + |\tilde{S}'_1 - \tilde{S}''_2|^m + |\tilde{S}'_1 - \tilde{S}''_3|^m \\ &+ |\tilde{S}'_2 - \tilde{S}''_1|^m + |\tilde{S}'_2 - \tilde{S}''_2|^m + |\tilde{S}'_2 - \tilde{S}''_3|^m \\ &+ |\tilde{S}'_3 - \tilde{S}''_1|^m + |\tilde{S}'_3 - \tilde{S}''_2|^m + |\tilde{S}'_3 - \tilde{S}''_3|^m \end{aligned} \tag{2.28}$$

where m is an exponent which determines the curvature of the function. As described in [15], the yield function fulfils the requirement of convexity. Additionally, expressions needed for computing the gradient of the potential, $\frac{\partial f}{\partial \boldsymbol{\sigma}}$, are derived. The anisotropic deviatoric stresses $\tilde{\boldsymbol{s}}'$ and $\tilde{\boldsymbol{s}}''$ are obtained by transforming the deviatoric stress tensor $\boldsymbol{s}$ by using the following transformation matrices,

$$\boldsymbol{C}' = \begin{bmatrix} 0 & -c'_{12} & -c'_{13} & 0 & 0 & 0 \\ -c'_{21} & 0 & -c'_{23} & 0 & 0 & 0 \\ -c'_{31} & -c'_{32} & 0 & 0 & 0 & 0 \\ 0 & 0 & 0 & c'_{44} & 0 & 0 \\ 0 & 0 & 0 & 0 & c'_{55} & 0 \\ 0 & 0 & 0 & 0 & 0 & c'_{66} \end{bmatrix} \tag{2.29a}$$

$$\boldsymbol{C}'' = \begin{bmatrix} 0 & -c''_{12} & -c''_{13} & 0 & 0 & 0 \\ -c''_{21} & 0 & -c''_{23} & 0 & 0 & 0 \\ -c''_{31} & -c''_{32} & 0 & 0 & 0 & 0 \\ 0 & 0 & 0 & c''_{44} & 0 & 0 \\ 0 & 0 & 0 & 0 & c''_{55} & 0 \\ 0 & 0 & 0 & 0 & 0 & c''_{66} \end{bmatrix} \tag{2.29b}$$

The 18 coefficients c'_{ij} and c''_{ij} have no physical meaning and are determined through an optimization method. The exponent m is either specified by the user in advance or included in the optimization. The value $m = 1$ or a high value of m corresponds to Tresca's yield criterion while the value $m = 2$ or $m = 4$ corresponds to von Mises'. According to [15], $m = 6$ and $m = 8$ give good approximations for BCC and FCC metals, respectively.

An anisotropic yield function should have the possibility to become isotropic for a certain set of parameters. The proposed yield function reduces to von Mises' yield function for $c'_{ij} = c''_{kl} = 1$ and $m = 2$ or $m = 4$. The reduction to isotropy may be illustrated by showing that $\tilde{\boldsymbol{s}}' = \boldsymbol{s}$ for $c'_{ij} = 1$. Applying $c'_{ij} = 1$ to Equation (2.26a) gives

$$\tilde{\boldsymbol{s}}' = \boldsymbol{C}'\boldsymbol{s} = \begin{bmatrix} 0 & -1 & -1 & 0 & 0 & 0 \\ -1 & 0 & -1 & 0 & 0 & 0 \\ -1 & -1 & 0 & 0 & 0 & 0 \\ 0 & 0 & 0 & 1 & 0 & 0 \\ 0 & 0 & 0 & 0 & 1 & 0 \\ 0 & 0 & 0 & 0 & 0 & 1 \end{bmatrix} \begin{bmatrix} s_{xx} \\ s_{yy} \\ s_{zz} \\ s_{yz} \\ s_{zx} \\ s_{xy} \end{bmatrix} = \begin{bmatrix} -s_{yy} - s_{zz} \\ -s_{xx} - s_{zz} \\ -s_{xx} - s_{yy} \\ s_{yz} \\ s_{zx} \\ s_{xy} \end{bmatrix} = \begin{bmatrix} s_{xx} \\ s_{yy} \\ s_{zz} \\ s_{yz} \\ s_{zx} \\ s_{xy} \end{bmatrix} = \boldsymbol{s} \tag{2.30}$$

since the trace of the deviatoric stress tensor is zero per definition, i.e. $\mathrm{tr}(\boldsymbol{s}) \overset{\text{def}}{=} s_{xx} + s_{yy} + s_{zz} = 0$.

2.4.3 The concepts of work hardening

The concept of work hardening is presented in general terms with emphasis on the aspects relevant for the current work. The section is concluded by a presentation of the specific hardening rule used to represent the base material.

The strength of a metal is usually increased when plastic deformations occur. The physical mechanism is explained by an increase of the dislocation density with deformation in the crystal lattice [21]. Plastic deformations are caused by motion of dislocations, which is hindered by the presence of other dislocations. As the dislocation density increases, the resistance to dislocation motion by other dislocations becomes more pronounced, and the strength of the material is increased. This phenomenon is called work hardening.

In order to describe work hardening, internal variables with evolution equations must be introduced, which reflect the changes of the micro structure of the material as a result of plastic straining.

Two of the most common ways to account for work hardening are called isotropic hardening and kinematic hardening. Kinematic hardening corresponds to a translation of the elastic domain (i.e. the yield surface) in the direction of the plastic flow. Isotropic hardening corresponds to an isotropic expansion of the elastic domain. In this thesis isotropic hardening is assumed.

For isotropic hardening it is common to introduce a strain dependent hardening variable R to describe the expansion of the elastic domain. The yield stress becomes a function of R, given by $\sigma_Y = \sigma_Y(R) = \sigma_0 + R$. Here, σ_0 is the initial yield stress and $R = R(\epsilon^p_{eq})$ is the strain-dependent increase of the yield stress where ϵ^p_{eq} is the equivalent plastic strain. Henceforth, σ_Y and σ_0 are denoted the flow stress and yield stress, respectively.

With isotropic hardening the yield function takes the form

$$f(\boldsymbol{\sigma}, R) = \phi(\boldsymbol{\sigma}) - \sigma_Y(R) \leq 0 \tag{2.31}$$

As plastic deformations evolve, the hardening parameter R, and thereby the flow stress σ_Y, increase, resulting in an expansion of the elastic domain.

2.4.4 Voce isotropic hardening rule

A common model used to include isotropic work hardening is the Voce rule. The 7 parameter Voce rule is used in this thesis and is given by the formula

$$\sigma_Y = \sigma_0 + R(\epsilon_{eq}^p) = \sigma_0 + \sum_{n=1}^{3} Q_{Rn} \left[1 - \exp(-C_{Rn}\epsilon_{eq}^p)\right] \tag{2.32}$$

where the six constants Q_{R1}, C_{R1}, Q_{R2}, C_{R2}, Q_{R3} and C_{R3} are parameters which must be fitted to the experimental data.

2.4.5 Concerning the yield surface

In this thesis isotropic elasticity is assumed, which together with the yield function and the hardening rule form the constitutive model. A yield surface with intersections for constant shear stress σ_{xy} is visualized for plane stress in Figure 2.8a. The same yield surface is plotted in the σ_{xy} vs. $\frac{\sigma_x+\sigma_y}{\sqrt{2}}$ plane with intersections with planes with normal vectors along the line $\sigma_x+\sigma_y = 0$ in Figure 2.8b. The location of yield stress states induced in some common material tests are indicated. The indicated angles refer to the loading direction in the tests relative to the reference direction of the anisotropic material. The reference direction is usually the rolling direction. In this particular case the x-direction is the reference direction for the material.

In the case of uniaxial tension the yield stress state is in Figure 2.8a located on the abscissa and ordinate axis for material orientations of 0 and 90 degrees, respectively. For directions between 0 and 90 degrees a shear component is introduced, which moves the stress state into the σ_{xy}-dimension of the stress space. The location of the yield stress state for a material orientation of 45 degrees is shown in both Figure 2.8a and 2.8b. The uniaxial yield stress states for all material orientations are located on a curve along the yield surface which is a straight line when projected onto the $\sigma_{xy} = 0$ plane. This curve is denoted the UT-curve and its projection is denoted the UT-line in this thesis.

For a plane strain tension state in a plane stress condition, the plastic strain increment is zero in one direction. According to the associated flow rule in Equation (2.20) this implies that the plastic strain increment is directed parallel to the axis of the driving stress. Thus, the plane strain yield stress state is located where the normal of the yield surface is directed parallel to the abscissa or ordinate axis as shown in Figure 2.8a.

In the in-plane single shear tests a pure shear stress state is induced. For a material orientation of 0 (or 90) degrees this stress state is located along the line where $\sigma_x = \sigma_y = 0$. The yield stress state is thus located in the origin in Figure 2.8a and on the top in Figure 2.8b. The yield stress state for a material orientation of 45 degrees is also shown in both figures.

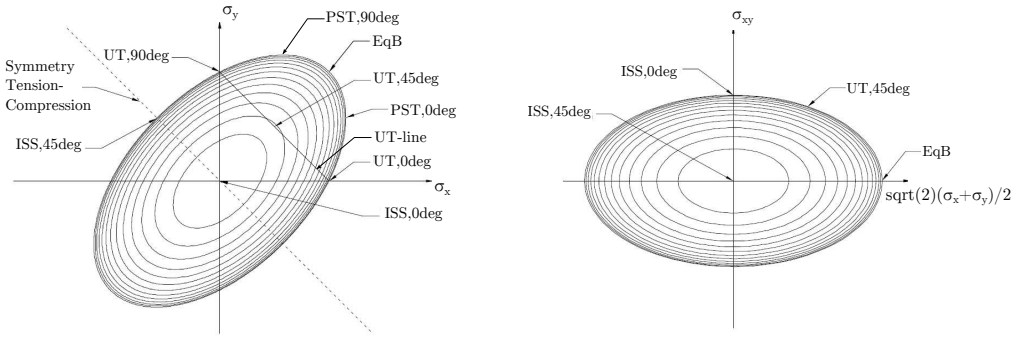

(a) Intersections for constant shear stress σ_{xy}.

(b) Intersections of planes with normal vectors along the line $\sigma_x + \sigma_y = 0$.

Figure 2.8: Different stress states on the yield surface. The material reference direction is the x-direction.

For an equi-biaxial (EqB) stress state in tension, $\sigma_x = \sigma_y$ and $\sigma_{xy} = 0$. This stress state is shown in both figures.

One of the sets of parameters used to calibrate the yield function in this thesis is the flow stress ratios (r-ratios). The r-ratio is defined as the uniaxial flow stress for a material direction α normalized to the uniaxial flow stress in a reference direction for a certain amount of plastic work W^p. That is,

$$r_\alpha\left(W^p\right) = \frac{\sigma_\alpha\left(W^p\right)}{\sigma_{ref}\left(W^p\right)} \tag{2.33}$$

where σ_α and σ_{ref} are the flow stresses in the α and the reference directions, respectively. The r-ratios are measures of the anisotropy of the material with respect to the flow stress. For isotropic materials the r-ratios are unity.

If isotropic hardening is assumed, the r-ratios become independent of W^p. Recall that isotropic hardening corresponds to an isotropic expansion of the yield surface. Thus, the length ratio of two vectors from the origin to two arbitrary points in the stress space is preserved during hardening. σ_α and σ_{ref} may be interpreted as the magnitudes of two such vectors, implying that the ratio $\frac{\sigma_\alpha}{\sigma_{ref}}$ is constant during hardening. Thus, in the case of isotropic hardening, the r-ratio may be interpreted as the magnitude of the yield stress in the direction α normalized to the yield stress in the reference direction for all levels of plastic work.

Although the material model predicts constant r-ratios, they may be varying when measured experimentally. The average values of the measured r-ratios, r_α^{avg}, from uniaxial tension tests are used in the calibration of the yield function in this thesis. r_α^{avg} is calculated through the equation

$$r_\alpha^{avg} = \frac{1}{W_{max}^p}\int_0^{W_{max}^p} r_\alpha\left(W^p\right)\mathrm{d}W^p \tag{2.34}$$

where W^p_{max} is the amount of plastic work at the onset of diffuse necking. In the calibration of the yield function the r-ratios predicted by the model are fitted to r-ratios found from uniaxial tension tests. The magnitude of the yield stress along the UT-curve is thereby determined.

The second set of parameters used in the calibration is the strain ratios (R-ratios). The R-ratio is defined as the ratio of the plastic strain increments in the width and thickness directions. The definition reads

$$R_\alpha = \left.\frac{\dot{\epsilon}^p_w}{\dot{\epsilon}^p_t}\right|_\alpha = \left.\frac{\mathrm{d}\epsilon^p_w}{\mathrm{d}\epsilon^p_t}\right|_\alpha \tag{2.35}$$

where $\dot{\epsilon}^p_w$ and $\dot{\epsilon}^p_t$ are the plastic strain rates and $\mathrm{d}\epsilon^p_w$ and $\mathrm{d}\epsilon^p_t$ the infinitesimal plastic strain increments in the width and thickness directions, respectively. For isotropic materials the R-ratios are unity.

As isotropic hardening is assumed, the R-ratios for uniaxial tension are determined using the relation

$$R_\alpha = \left.\frac{\mathrm{d}\epsilon^p_w}{\mathrm{d}\epsilon^p_t}\right|_\alpha = \left.\frac{\Delta\epsilon^p_w}{\Delta\epsilon^p_t}\right|_\alpha \tag{2.36}$$

where $\Delta\epsilon^p_w$ and $\Delta\epsilon^p_t$ are calculated based on measurements of the width and thickness of the specimens before and after the UT tests. The R-ratios are measures of the anisotropy of the material with respect to the plastic strains.

If plastic incompressibility is assumed, the plastic strain increments in the length, width and thickness directions are related through the equation

$$\mathrm{d}\epsilon^p_l + \mathrm{d}\epsilon^p_w + \mathrm{d}\epsilon^p_t = 0 \tag{2.37}$$

where $\mathrm{d}\epsilon^p_l$ is the infinitesimal plastic strain increment in the length direction. Thus, if the R-ratio and the strain in the length direction are measured in uniaxial tension tests, all the strain increments are completely defined. As the incremental plastic strain increments are equivalent to the plastic strain rates, all the components of the plastic strain rate tensor $\dot{\boldsymbol{\epsilon}}^p$ are thereby determined. The direction of the gradient of the yield surface is then completely constrained through the associated flow rule (Equation (2.20)). Equivalently, the shape of the yield function along the UT-curve is constrained. In the calibration of the material model the R-ratios predicted by the model constrained to fit the R-values found from uniaxial tension tests in different directions.

As explained above, by constraining the r- and R-ratios to fit experimental data from uniaxial tension tests, the magnitude of the yield stress and shape of the yield function along the UT-curve are determined. This leaves a substantial region of the yield surface uncalibrated. For this reason, the EqB point may have great significance. Optimally, values for the EqB point should be constrained to experimental data in the calibration.

The biaxial plastic strain ratio R_{EqB} is defined as

$$R_{EqB} = \frac{\dot{\epsilon}^p_y}{\dot{\epsilon}^p_x} \tag{2.38}$$

where $\dot{\epsilon}^p_y$ and $\dot{\epsilon}^p_x$ are the plastic strain rates in the x- and y-directions, respectively. R_{EqB} is related to, and thus constrain, the gradient of the yield surface at the equi-biaxial

point. The equi-biaxial stress ratio r_{EqB} defines the yield stress in biaxial tension (and compression). For $r_{EqB} = 1$, yield occurs when $\sigma_x = \sigma_y = \sigma_0$. r_{EqB} and R_{EqB} may be determined experimentally by through-thickness compression tests, assuming that the plastic deformation is independent of hydrostatic pressure.

Chapter 3

Experimental setup

In this chapter the experimental setup is presented. Material tests were performed for the AA6016 sheets. Single connector tests and component tests were performed for both self-piercing rivets (SPR) and self-piercing screws (SPS). The material and single connector tests were carried out under quasi-static conditions, while the component tests were performed for both dynamic and quasi-static loading conditions. The static tests were intended to serve as a reference to the dynamic tests. All specimens were machined from sheets coming from the same batch. The sheets were rolled aluminium with thickness 2 mm. An overview of the experimental program is found in Table 3.1.

The material tests were performed in order to calibrate and validate the anisotropic material model. The material test program included uniaxial tension (UT) tests in seven material directions. Additionally, plane strain tension (PST) tests and in-plane single shear (ISS) tests were performed in the longitudinal and transverse directions compared to the rolling direction of the sheets. All material tests were performed for material without and with heat treatment (HT). In addition, UT tests with pre-straining and subsequent heat treatment were carried out for three levels of pre-straining.

In the automotive industry, a combined paint curing and heat treatment process is often applied. At the same time as the paint cures, the material is brought to a higher temper. The motivation for the tests on heat treated material was to investigate the effect of the heat treatment on the behaviour of the material, as well as on pre-strained material. The results are presented and discussed, but not further used in this work.

Three single connector tests were performed in order to calibrate and validate the point-connector model for SPR and SPS connections. The single connector test program consisted of cross (C), single lap-joint (SLJ) and peeling (P) tests. In the C tests pure normal loading, pure shear loading and a combination of normal and shear loading were applied to the connection in order to calibrate the point-connector model. SLJ and P tests were performed to validate the calibrated model.

The component tests concluded the experimental program and consisted of quasi-static and dynamic crash box (CB) tests. The CB tests were performed for both SPR and SPS connections.

Table 3.1: An overview of the experimental program. The notation N-M in the *Material orientation* column indicates the orientation of the material in the top and bottom sheet of connected specimens, respectively. *Loading angle* is related to the specimen orientation and HT means heat treatment.

	Test type	Material orientation	Loading angle	Repetitions	Date, 2013
Material	Uniaxial tension	0, 15, 30, 45, 60, 75, 90	0	3	20.02
	Uniaxial tension with HT	0, 15, 30, 45, 60, 75, 90	0	3	25.02
	3 % pre-strained uniaxial tension	90	0	3	26.02
	6 % pre-strained uniaxial tension	90	0	3	26.02
	10 % pre-strained uniaxial tension	90	0	3	26.02
	Plane strain tension	0, 90	0	3	22.02
	Plane strain tension with HT	0, 90	0	3	25.02
	In-plane single shear	0, 90	0	3	21.02
	In-plane single shear with HT	0, 90	0	3	26.02
Single connector	Cross (riveted)	90-0	0, 45, 90	3-5	13.05
	Cross (screwed)	90-0	0, 45, 90	3-5	24.05
	Single lap-joint (riveted)	0-0, 90-90	0	5	07.05
	Single lap-joint (screwed)	0-0, 90-90	0	5	24.05
	Peeling (riveted)	90-90	0	5	07.05
	Peeling (screwed)	90-90	0	5	24.05
Component	Crashbox, static (riveted)	0-90	Axial	3	22.05
	Crashbox, static (screwed)	0-0	Axial	2	22.05
	Crashbox, dynamic (riveted)	0-90	Axial	7	14.05
	Crashbox, dynamic (screwed)	0-0	Axial	3	16.05

The intention of the CB tests was firstly to understand the behaviour and fracture of the SPR and SPS connections in a complex dynamic non-controlled loading situation. Secondly, to investigate the ability of the combined material and point-connector model to describe the same loading situation both for SPR and SPS.

The rolling direction of the sheets is referred to as the 0 degree direction, where 0 degrees indicates the angle between the rolling direction and the longitudinal direction of the specimens. The transverse direction is thus referred to as the 90 degree direction.

3.1 Material tests

Quasi-static UT, PST and ISS tests were performed until the specimens fractured. Depending on the test, nominal strain rates of $\dot{\epsilon}_{\text{nom}} = 4 \cdot 10^{-3}$ s^{-1} and lower ensured the tests to be quasi-static.

In order to investigate the effect of heat treatment of the specimens, an identical set of tests was performed on specimens heat treated at 170 °C for 45 minutes. After heat treatment the specimens cooled in room temperature for at least 48 hours. In addition, the effect of heat treatment on pre-straining was investigated with UT specimens.

The name system assigned in the material test program follows the syntax XX-YY-ZZ-NN. XX refers to the test type, YY indicates whether the specimen was heat treated or not, ZZ is the angle between the longitudinal direction of the specimen and the rolling direction of the sheet, and NN refers to the repetition number. As an example the test UT-WOHT-15-02 is the second uniaxial tension test without heat treatment in the 15 degree direction.

A slightly different name system is used for the pre-strained UT specimens. Here XX refers to test type (PRE), YY to the amount of pre-strain, ZZ to the angle and NN to the repetition number. As all the pre-strained specimens were heat treated after the pre-straining, PRE implies heat treatment. As an example PRE-06-90-03 is the third specimen in the 90 degree direction pre-strained up to 6 % nominal strain followed by heat treatment.

Details of the experimental setup from the material tests are found in Appendix A.1.

3.1.1 Uniaxial tension

The geometry of the UT specimens is shown in Figure 3.1 and a picture from the experiments is found in Figure 3.2. The nominal length of the primary deformation area was 20 mm, the nominal width was 5 mm, the nominal thickness was 2 mm and the overall nominal length of the specimens was 60 mm. The exact measurements of the thickness and width in the primary deformation area were measured at three locations along the length, identified by the lines with different colours in Figure 3.1. The average values of the three measurements were used in the computation of engineering stress. After fracture, the width and thickness were measured at the same locations. Post-test measurements in

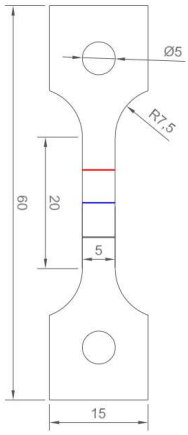

Figure 3.1: Nominal geometry of the UT specimens.

Figure 3.2: UT test setup.

parts of the specimen clearly affected by necking were ignored. Geometry measurements before and after the UT tests are found in Table B.1 and B.2.

All UT tests were performed with a cross head velocity of 1.2 mm/min, except for in UT-WOHT-00-01 and UT-WOHT-00-02 where the velocity was set to 0.6 mm/min. This corresponds to nominal strain rates of $\dot{\epsilon}_{\text{nom}} = 10^{-3}$ s^{-1} and $\dot{\epsilon}_{\text{nom}} = 5 \cdot 10^{-4}$ s^{-1}, respectively. The gauge length of the extensometer was 10 mm, except for in UT-WOHT-00-01 where it was 15 mm. For some tests localization occurred outside the extensometer gauge. The specimens were simply supported with a pin through the hole on each side.

3.1.2 Pre-strained uniaxial tension

In addition to the standard UT tests, some specimens were exposed to pre-straining followed by heat treatment and then tested until fracture. The specimen geometry and cross head velocity were the same as for the standard UT tests. The specimens were pre-strained to either 3, 6 or 10 % nominal strain before heat treatment at 170 °C for 45 minutes. All pre-strained UT specimens were oriented in the 90 degree direction. Measurements of the specimens are found in Table B.3 and B.4.

3.1.3 Plane strain tension

The geometry of the PST specimens is shown in Figure 3.3 and a picture of the experimental setup is shown in Figure 3.4. The thickness and the minimum width of the centre area were measured before the tests were performed. The nominal measures were 2.0 mm and 17.33 mm, respectively. The measurements of the PST specimens are found in Table B.5 and B.6.

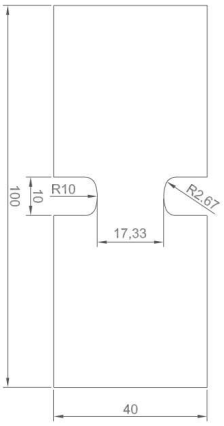

Figure 3.3: Nominal geometry of the PST specimens.

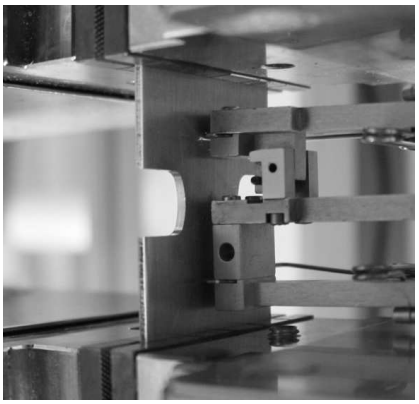

Figure 3.4: PST test setup.

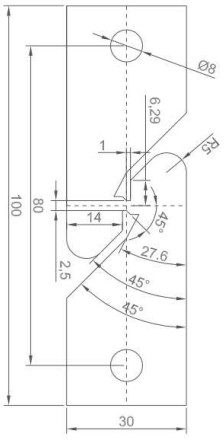

Figure 3.5: Nominal geometry of the ISS specimens.

Figure 3.6: ISS test setup.

In the PST tests the cross head velocity was set to 0.6 mm/min, which was assumed to ensure quasi-static conditions. The gauge length of the extensometer was 25 mm. Pneumatic clamps were used for gripping. When the clamps tightened, a compressive force due to contraction raised in the specimens. The force was well within the elastic range.

3.1.4 In-plane single shear

The geometry of the ISS specimens is shown in Figure 3.5 and a picture from the experiment is shown in Figure 3.6. The thickness and the smallest length of the central area of the specimen were measured before the test. The nominal values were 2.0 mm and 2.5 mm, respectively. Geometry measurements of the ISS specimens are found in Table B.7 and B.8.

All ISS tests were performed with a cross head velocity of 0.6 mm/min, except for ISS-WOHT-00-01 where the velocity was 0.15 mm/min. This was assumed to ensure quasi-static conditions. The gauge length of the extensometer was 40 mm. The specimens were simply supported with a pin through the hole on each side. The diameter of the pins was smaller than the holes in the specimens.

ISS tests were performed on specimens cut from both the 0 degree and the 90 degree directions. However, if the specimen shape in Figure 3.5 produce a pure shear state, the results from ISS tests with the material oriented in the 0 and 90 degree directions should be equal due to the symmetry of shear stresses.

3.2 Connections

The single connector and component tests were assembled by use of either self-piercing rivets or self-piercing screws. In this section the assembly of the connections is described.

3.2.1 Self piercing rivets

The rivets were of Böllhof type C-SKR made of a high strength steel with nominal diameter 5 mm and length 6.5 mm. The nominal cross section of the rivets is illustrated in Figure 3.7a, and as shown in Figure 3.7b, a flat die was used. The rivet and tool geometries were based on the Böllhof standards [19].

In order to investigate the details and to control the quality of the connection, a rivet connection was cut in half. The cross section of the cut rivet connection is shown in Figure 3.8. A gap is observed under the rivet head and the mechanical interlock is acceptable.

The riveted specimens were assembled in a laboratory at NTNU using a Böllhof RIVSET Vario machine, with a pressure of 190 bar. Due to the manual riveting procedure, some randomness in the position of the rivets was inevitable. For this reason the locations of the rivets were measured for each specimen together with the specimen geometries. The measurements are given in Section B.2 and B.3.

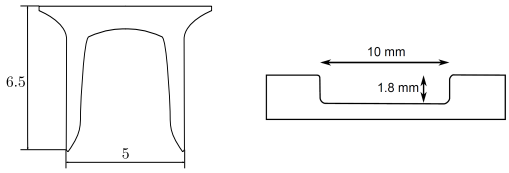

(a) Rivet. (b) Die.

Figure 3.7: Nominal geometry of rivet and die.

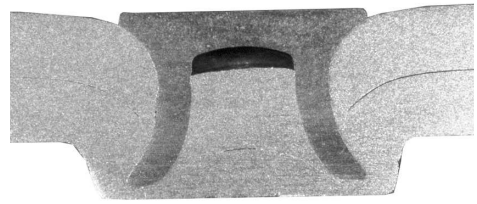

Figure 3.8: Cross section of assembled rivet.

Porcaro et al. [8] performed an extensive experimental and numerical investigation of the riveting procedure. The effects of different combinations of rivet length, die shape, sheet material and sheet thickness were studied, and interested readers are encouraged to look up the paper.

3.2.2 Self-piercing screws

The screws were of Ejot type WN-2152 M4 with standard tip made of case hardened mild steel, and is illustrated in Figure 3.9a. To avoid material between the plates, a hole with a diameter of 4 mm was drilled in the top sheet (where the screw entered) before assembly. An example of material between the plates is shown in Figure 3.9b. A picture of the formed draught on the reverse side of the material stack is shown in Figure 3.9c.

The cross section of a assembled screw is shown in Figure 3.10. It is observed that the head is stamped into the top sheet and there is no contact between the screw and sheet near the head. Threads are engaged in the top sheet in addition to the bottom sheet.

The screwed specimens were assembled by the company Torp in Oslo. Two of the screws were fractured prior to testing, probably due to over torque during assembly. Geometrical measurements of the screw positions are given in Section B.2 and B.3.

3.3 Single connector tests

Quasi-static C, SLJ and P tests were performed until the connections ruptured. A cross head displacement of 10 mm/min was assumed to ensure quasi-static conditions.

A similar name system as for the material tests was applied for the single connector tests. The syntax is XX-T-YY-ZZ-NN, where XX refers to the test type, T indicates whether it was an SPR or an SPS connection, YY and ZZ indicate the material orientation of the top and bottom sheets, respectively, and NN refers to the repetition number. The top sheet is the sheet into which the rivet or screw entered. As an example SLJ-S-00-00-01 is the first SLJ test with SPS, where the material of the plates are oriented in the longitudinal direction. In addition, a short name system was adopted for the C tests. The short

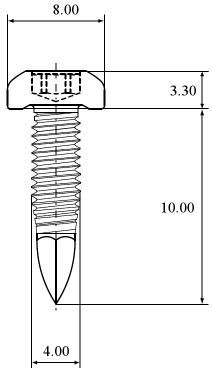

(a) Nominal geometry.

(b) Material between the plates.

(c) Underside of bottom plate.

Figure 3.9: Details of screw connection.

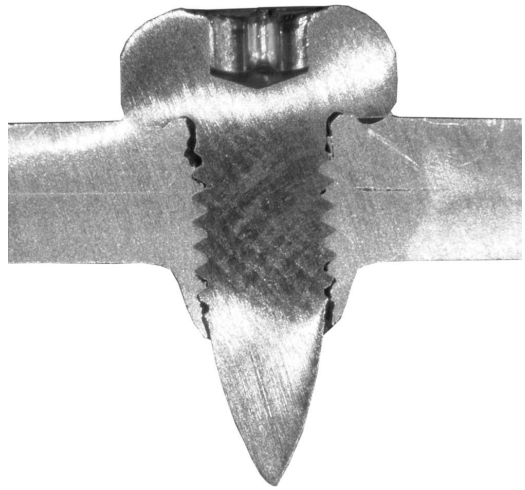

Figure 3.10: Cross section of assembled screw connection.

Table 3.2: Placement of connections on C specimens. Measurements are given in mm and related to Figure 3.11.

Connection	Value	Measure 1	Measure 2
Rivet	Nominal	60.0	20.0
	Average	59.9	20.1
	Max. deviation from average	0.6	0.6
Screw	Average	59.9	19.9
	Max. deviation from average	0.5	0.3

name syntax was C-X, where X indicates the loading angle in the tests. Details of the experimental setup in the single connector tests are found in Section A.2.

3.3.1 Cross

The geometry of the C specimens is shown in Figure 3.11. For all C tests, the material of the top plate was oriented in the 90 degree direction and the material of the bottom plate was oriented in the 0 degree direction.

The exact length and width of both plates, as well as the connection position were measured for each specimen before the tests. The measured geometry for riveted and screwed specimens is found in Table B.9 and B.10, respectively. Characteristic information of the positioning of the rivets and screws is summarized in Table 3.2. The position of the connection was measured as the distance from the left and top edge of the top plate to the centre of the rivet or screw, as indicated with red stippled lines in Figure 3.11.

The holes in the plates indicated in Figure 3.11 were needed in order to clamp the specimens. A special designed clamping rig was used in order to obtain the different loading modes. The clamping rig and a picture of the test setup is shown for a 45 degree loading angle in Figure 3.12 and 3.13, respectively. The clamping rig consisted of a clamping device where the specimens were attached using massive metal blocks with bolts through the holes of the specimen, two lock plates that could be rotated to produce different loading angles and two pull bars. For the tests with SPR, the pull bars were clamped to the test machine using hydraulic clamps. For the tests with SPS the pull bars were attached to the machine using screws. The cross head displacement was recorded during the tests.

3.3.2 Single lap-joint

The geometry of the SLJ specimens and a picture of the experimental setup is shown in Figure 3.14 and Figure 3.15, respectively. The extensometer gauge length was 50 mm and mechanical grips were used to fasten the specimens. The specimens were constructed by connecting two rectangular sheets with nominal dimensions 120 mm $\times$ 40 mm with an overlap of 40 mm. The nominal position of the connection was in the centre of the overlap area. The tests were carried out with the material oriented both in the 0 and the 90 degree directions.

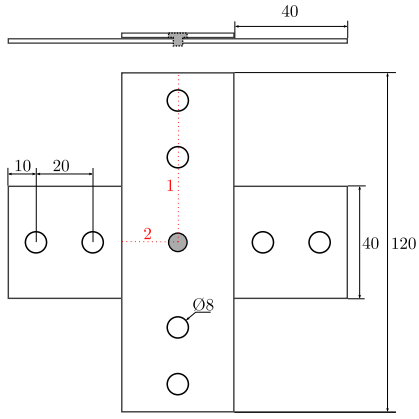

Figure 3.11: Nominal geometry of the C specimens.

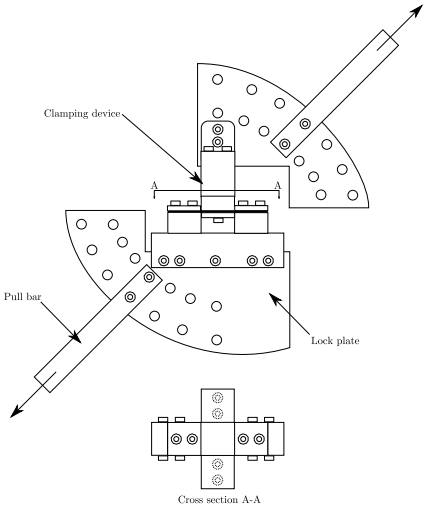

Figure 3.12: Clamping rig used in the C tests.

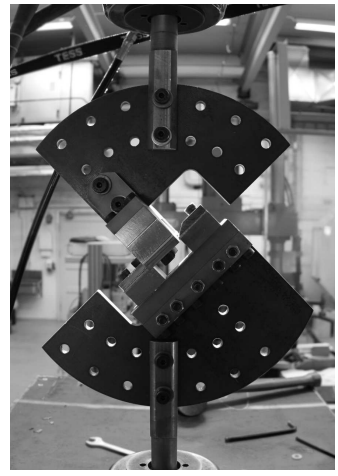

Figure 3.13: Test setup in the C tests.

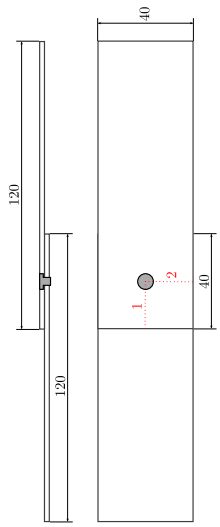

Figure 3.14: Nominal geometry of the SLJ specimens.

Figure 3.15: SLJ test setup.

Table 3.3: Placement of rivets and screws on SLJ specimens. Measurements are given in mm and related to Figure 3.14.

Connection	Value	Measure 1	Measure 2
Rivet	Nominal	20.0	20.0
	Average	20.3	20.2
	Max. deviation from average	1.0	0.4
Screw	Average	19.7	19.8
	Max. deviation from average	0.7	0.4

The exact total length and width of the specimens, as well as the location of the connections, were measured before the tests were performed. Geometrical measurements of the riveted and screwed SLJ specimens are found in Table B.11 and B.12, respectively. In the tables, the location of the connections are given in terms of the distances from the centre of the rivet or screw to the top and left edge of the top sheet, as shown with red stippled lines in Figure 3.14. Characteristic information of the positioning of the rivets and screws is found in Table 3.3.

During testing the extensometer was applied as long as possible to minimize the effect of the stiffness of the test rig, as well as possible sliding of the specimen in the grips, in the displacement measure. However, the extensometer was removed either when the maximum opening of 4 mm was reached or when out-of-the-plane deformations of the specimen disturbed the measurement. After the extensometer was removed the cross head displacement was used as displacement measure.

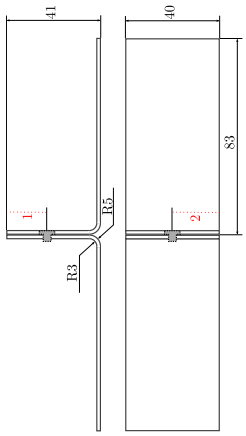

Figure 3.16: Nominal geometry of the P specimens.

Figure 3.17: P test setup.

Table 3.4: Placement of rivets and screws on P specimens. Measurements are given in mm and related to Figure 3.16.

Connection	Value	Measure 1	Measure 2
Rivet	Nominal	-	-
	Average	15.9	20.4
	Max. deviation from average	0.6	0.5
Screw	Average	14.4	20.5
	Max. deviation from average	0.5	0.3

3.3.3 Peeling

In Figure 3.16 the nominal geometry of the P specimens is shown and a picture of the experimental setup is presented in Figure 3.17. The specimens were prepared by bending plates of the same geometry used for the C and SLJ specimens. The test was performed for material oriented in the 90 degree direction.

The total length and width of the specimens as well as the location of the connections were measured before the tests were performed. The geometrical measurements are found in Table B.13 for rivets and in Table B.14 for screws. The location of the connections are again given in terms of the distances from the centre of the rivet or screw to the top and left edge of the top sheet, as shown with red stippled lines in Figure 3.16. Characteristic information of the positioning of the rivets and screws is found in Table 3.4.

The same experimental setup as for the SLJ tests was applied. The extensometer gauge length was 50 mm and mechanical grips were used to fasten the specimens.

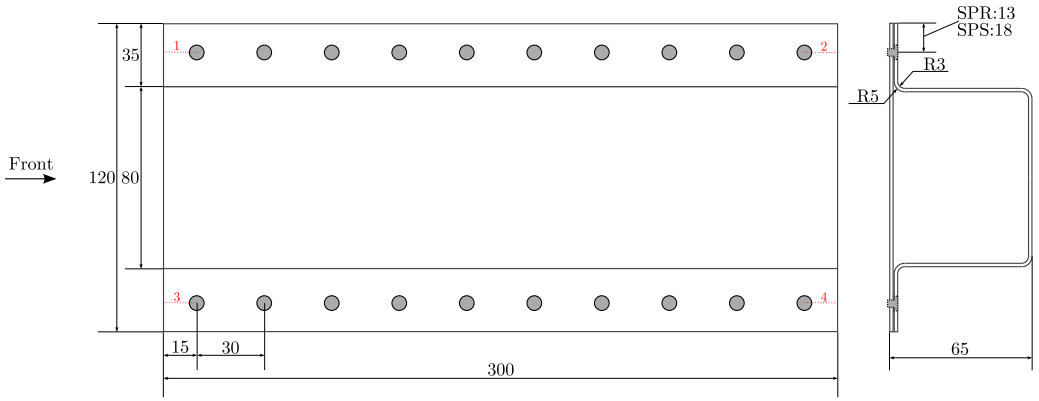

Figure 3.18: Nominal geometry of the CB specimens.

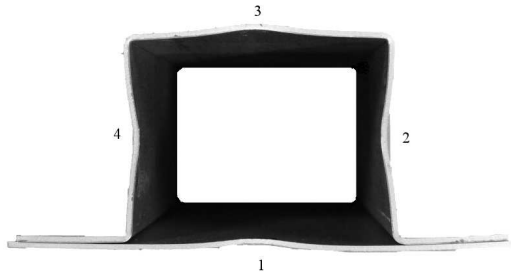

Figure 3.19: Buckling mode triggers on crash box specimens.

Displacements were measured in the same manner as for the SLJ tests. Data from the extensometer was used as long as possible, and subsequently the cross head displacement was used to measure the displacements.

3.4 Component tests

The component test program included quasi-static and dynamic tests of riveted and screwed crash boxes. The nominal geometry of the CB specimens is shown in Figure 3.18. In the description of the specimens, the *front* is where the impactor (static or dynamic) hit and the *rear* is the clamped part of the specimen. The *left* side is left of the front and, correspondingly, the *right* is right of the front. The *top* sheet is the hat profile while the *bottom* sheet is the flat plate.

For all CB specimens, the material in the top sheet was oriented in the 0 degree direction. For the riveted specimens the material in the bottom plate was oriented in the 90 degree direction while it was oriented in the 0 degree direction for the screwed. The crushing distance was approximately 150 mm in both static and dynamic tests.

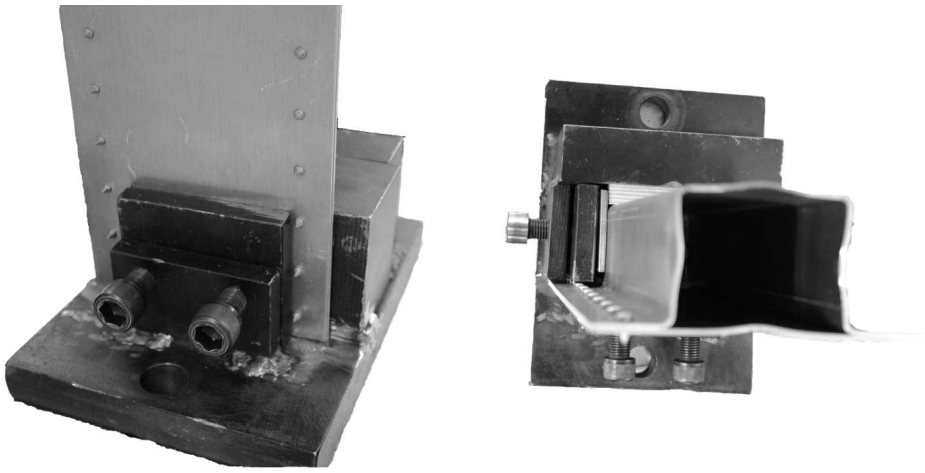

(a) Bottom support. (b) Side support.

Figure 3.20: Clamping of crash boxes.

The specimens were clamped with a custom made device, illustrated in Figure 3.20. The specimens were tightened from the left and bottom side. The specimen and clamping were positioned such that the specimen hit in the centre of the impactor. For one of the screwed and all the riveted crash boxes a steel plate was used between the clamping screws and the bottom side of the specimen, as may be seen in Figure 3.20a. For the remaining screwed specimens a plywood panel was used instead of the steel plate.

The CB specimens were triggered as shown in Figure 3.19 and measurements of the four triggered edges are found in Table B.17. The sides and the bottom sheet were bent inwards while the top was bent outwards. The triggering was performed to ensure that the same progressive buckling mode occurred for all CB tests, as well as to minimize the scatter in the tests. Hanssen et al. [31] found that triggering of the specimens effects the initial peak load significantly.

The name system assigned to the component tests follows the syntax CBNX-Y. CB is a short name for crash box, N is the repetition number of the actual test setup, X indicates whether the test was dynamic (D) or static (S) and Y represents the connection type (R for rivets and S for screws). As an example, CB3D-R means the third repetition of a riveted dynamic crash box test.

The rivets were positioned 13 mm from the edge while the corresponding measure for the screws was 18 mm, see Figure 3.18. This difference is believed to not be affecting the global response of the crash boxes. Generally, the rivets and screws were well-positioned, but some deviation from nominal values was observed near the ends. Of this reason the distances from the end rivets/screws to the edge in axial direction were measured for all specimens. The measurements are found in Table B.15 for rivets and B.16 for screws. A summary of the measurements is given in Table 3.5. It is evident that the screws were positioned close to the nominal values while some accumulated error were present for measure 1 and 4 (according to Figure 3.18) for the rivets.

Table 3.5: Placement of rivets and screws on crash box specimens. Measurements are given in mm and related to Figure 3.18.

Connection	Value	Measure 1	2	3	4
Rivet	Nominal	15.0	15.0	15.0	15.0
	Average	16.8	14.7	15.0	16.9
	Max. deviation from average	2.3	0.9	0.8	1.6
Screw	Average	15.0	14.8	15.0	15.1
	Max. deviation from average	0.4	0.2	0.6	0.1

3.4.1 Dynamic

The dynamic tests were conducted employing a kicking machine with a mass of 395.5 kg impacting the specimens at a velocity of approximately 10 m/s. A more detailed description of the kicking machine is provided by Hanssen et al. [32]. Figure 3.21 illustrates the kicking machine, and Figure 3.22 shows a plan view of the test setup. A picture of the test setup is shown in Figure 3.23. A trolley on rails is accelerated by a pendulum towards the test specimen which is clamped to a reaction wall. The desired impact velocity is obtained by the exertion of a force on the pendulum upon acceleration. A hydraulic/pneumatic actuator system is employed to obtain the desired impact force. The crushing of the specimens is stopped when the trolley hits the secondary energy absorbers. The secondary absorbers were replaced every third test, which caused some differences in total axial deformation.

The velocity of the impactor was measured using a photocell system located directly in front of the specimen. The load cell was attached to the front of the trolley and measured the impacting force as function of time at a sample rate of 100 000 to 200 000 points per second. A Phantom v1610 high-speed camera recorded the impact at a frame rate of 15 000 frames per second. The trolley displacement, as well as the displacement of the reaction wall were measured with a laser system attached to the rails.

Due to propagating elastic stress waves through the strain gauges in the load cell, induced by the impact with the specimen, high frequency noise is commonly observed in the force signal. Of this reason the measured force was filtered using a moving average low-pass filter. The force-time curves were smoothed using a moving average algorithm of 67 points for the test with sampling rate of 100 000 Hz, and 133 points for the tests with sampling rate of 200 000 Hz, corresponding to a filter frequency of 1500 Hz. The algorithm starts and ends the averaging gradually. The first data point is the original one. The second data point is the average of the third, second and first data points. This continues until the maximum number of data points is reached. Then the average is carried out using the maximum number of points until the end of the data set, whereas the number of points included in the averaging is gradually reduced until the last point is reached. The moving average reduces the initial peak force. However, the absorbed energy is correctly estimated.

Three independent measures of trolley displacement were performed in the tests. Firstly,

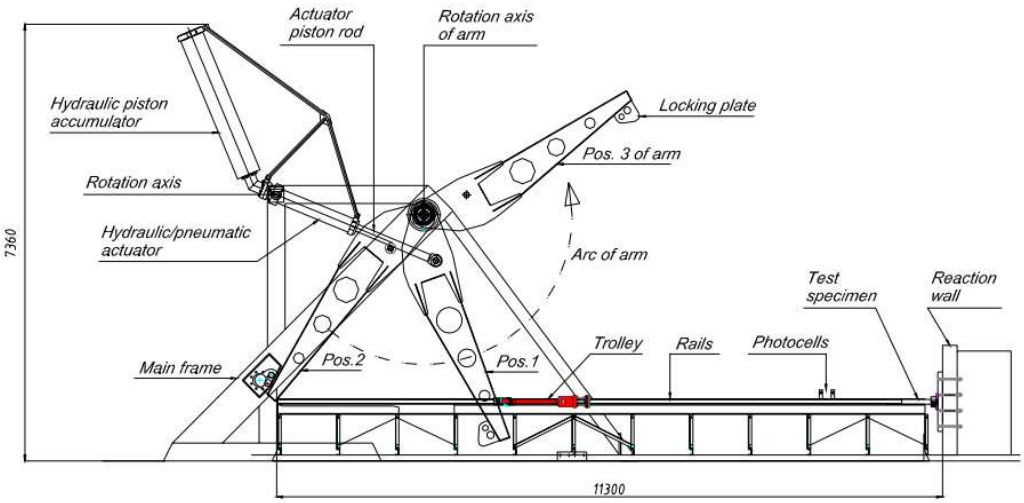

Figure 3.21: The kicking machine [32].

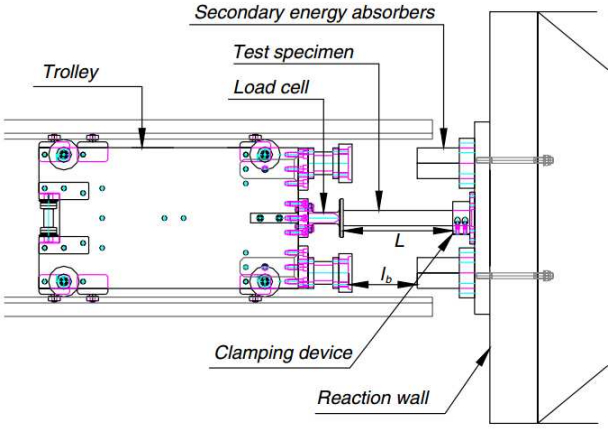

Figure 3.22: Top view of trolley and reaction wall [33].

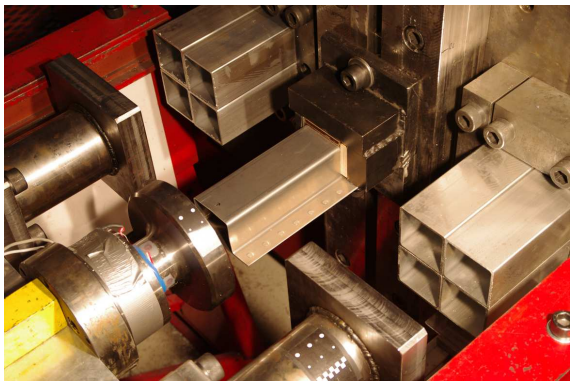

Figure 3.23: Test setup in the dynamic crash box tests.

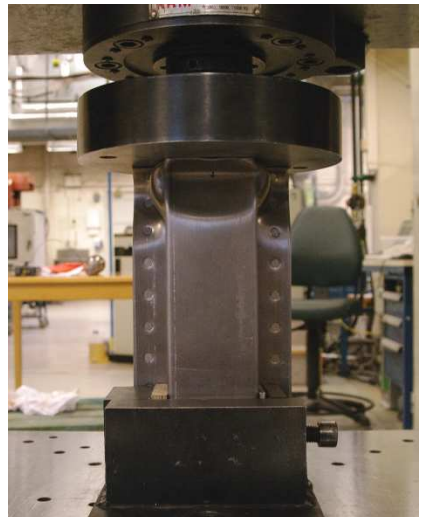

Figure 3.24: Test setup in the quasi-static crash box tests.

the displacement was extracted from the high-speed camera recording. White on the load cell, seen in Figure 3.23, served as references for the measurement. Secondly, the displacement was obtained by integrating the acceleration using the equation

$$u(t) = \int_0^t \int_0^t \frac{F(\tau)}{m} \mathrm{d}\tau \mathrm{d}\tau \tag{3.1}$$

where F is the filtered force, m is the trolley mass, t is the time and τ is a dummy variable for time. The third measurement was obtained with the laser system described above. The accuracy of the measurements was assessed by comparing the three measurements.

Some additional details of the experimental setup for the dynamic component test are found in Table A.1.

3.4.2 Quasi-static

The test setup from quasi-static CB tests is shown in Figure 3.24. An Instron 1332 test machine was employed with a load capacity of 250 kN. The same clamping as in the dynamic tests was utilized, and a steel plate was used as impactor. The velocity of the cross head was 10 mm/min, which was assumed to ensure quasi-static conditions. The total crushing distance was 150 mm. The cross head displacement was recorded during the tests. Quasi-static tests are referred to as *static* tests henceforth.

Chapter 4

Experimental results

4.1 Material tests

The results from the UT tests are presented in terms of engineering stress/strain curves. The results from the PST and ISS tests are presented with the extensometer displacement on the abscissa and force on the ordinate axis. The engineering stress σ_{eng} is defined as

$$\sigma_{eng} = \frac{F}{A_0} \tag{4.1}$$

where F is the force and A_0 is the initial area. The engineering strain ϵ_{eng} is defined as

$$\epsilon_{eng} = \frac{\Delta L}{L_0} \tag{4.2}$$

where $\Delta L = L - L_0$ and L and L_0 are lengths in the deformed and initial configuration, respectively. The engineering strain was either taken directly from the extensometer or computed according to Equation (4.2). Localization occurred inside the extensometer gauge for the PST and ISS tests, but outside or partially outside for most of the UT test. The results after necking depend on whether localization occurred inside or outside of the extensometer gauge.

Generally, little scatter was observed for the tests repetitions. Representative curves were chosen by investigating the curves prior to necking.

4.1.1 Uniaxial tension

The results from the UT tests without HT are presented in Figure 4.1. The selected representative curves are indicated with red colour and plotted together in Figure 4.1h.

Based on Figure 4.1h it is evident that some anisotropy is observed for the flow stress. The scatter in engineering stress for each test direction (Figure 4.1a through 4.1g) is negligible compared to the scatter in engineering stress for the representative curves (Figure 4.1h).

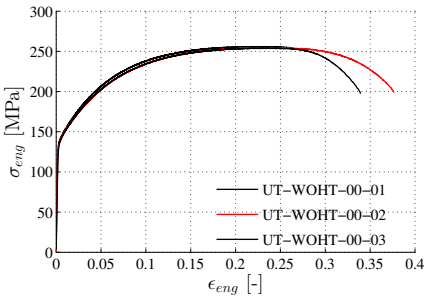

(a) 0 degree direction.

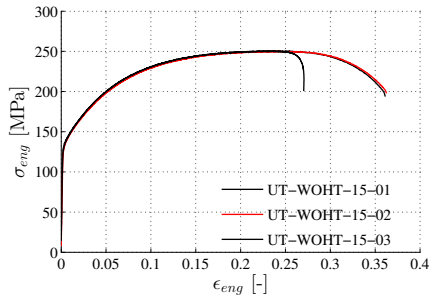

(b) 15 degree direction.

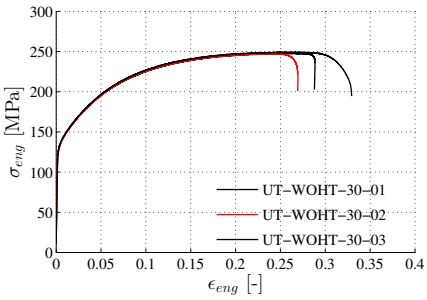

(c) 30 degree direction.

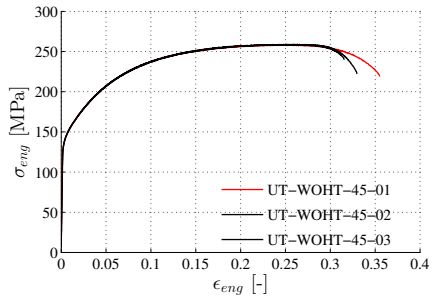

(d) 45 degree direction.

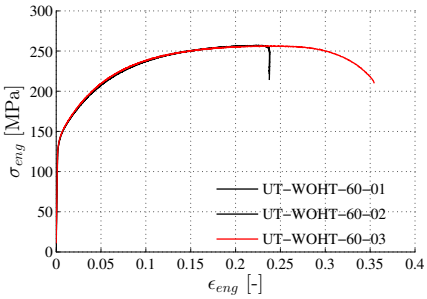

(e) 60 degree direction.

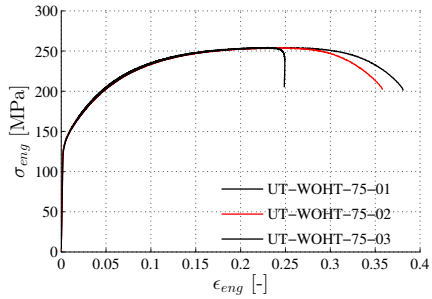

(f) 75 degree direction.

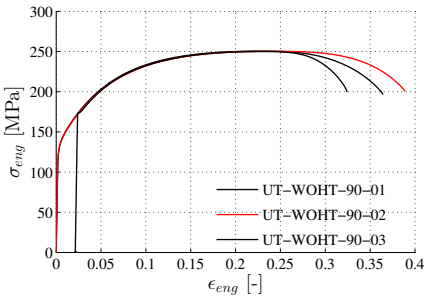

(g) 90 degree direction.

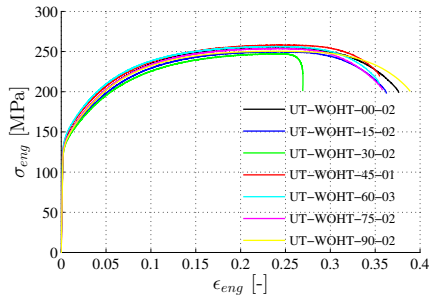

(h) Representative tests.

Figure 4.1: Engineering stress-engineering strain curves for UT tests without HT. The selected representative curves are indicated with red colour and are plotted in (h).

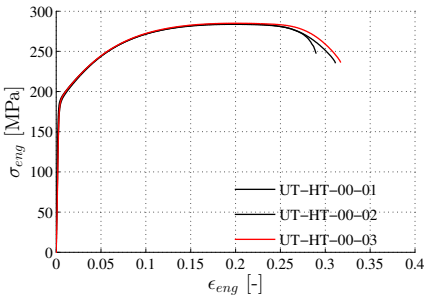

(a) 0 degree direction.

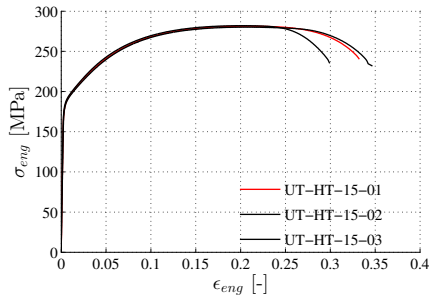

(b) 15 degree direction.

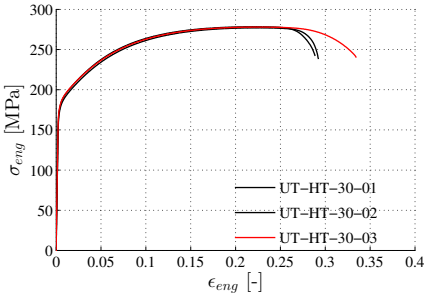

(c) 30 degree direction.

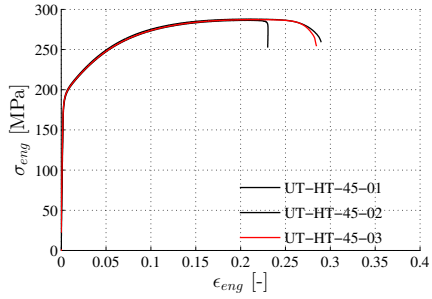

(d) 45 degree direction.

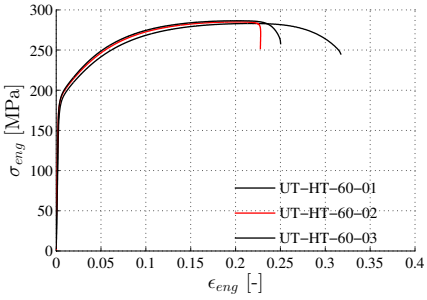

(e) 60 degree direction.

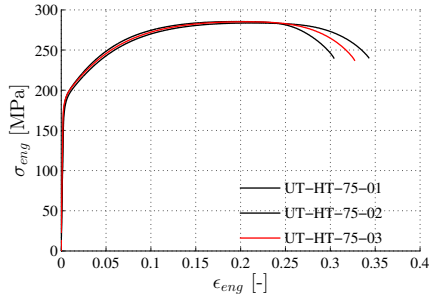

(f) 75 degree direction.

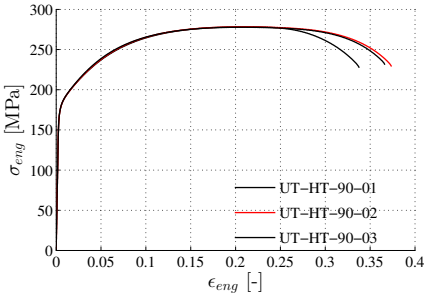

(g) 90 degree direction.

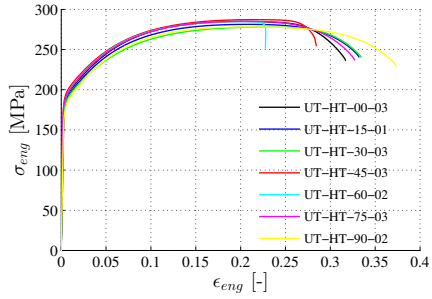

(h) Representative tests.

Figure 4.2: Engineering stress-engineering strain curves for UT tests with HT. The selected representative curves are indicated with red colour and are plotted together in (h).

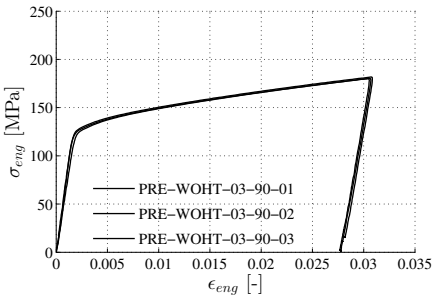

(a) Pre-straining up to 3 %.

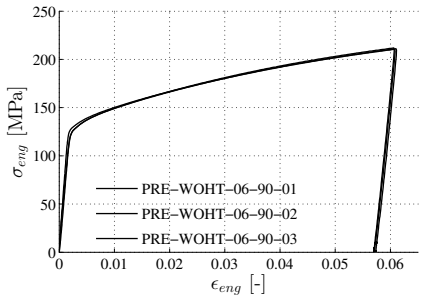

(b) Pre-straining up to 6 %.

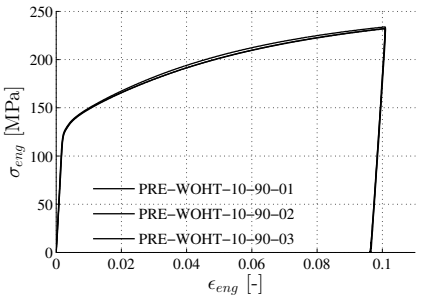

(c) Pre-straining up to 10 %.

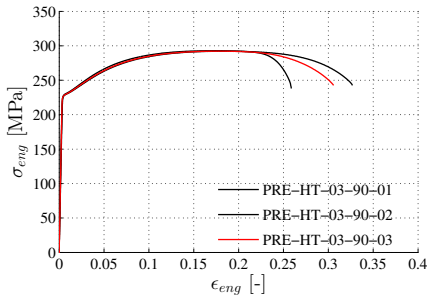

(d) 3 % pre-strain with subsequent HT.

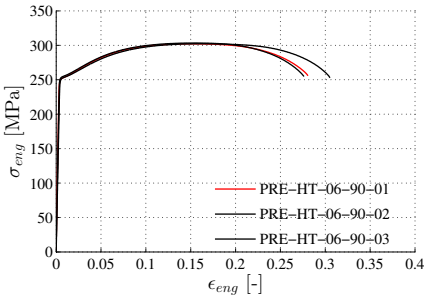

(e) 6 % pre-strain with subsequent HT.

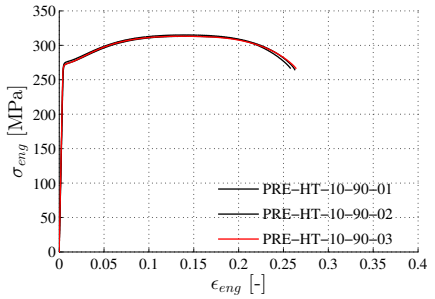

(f) 10 % pre-strain with subsequent HT.

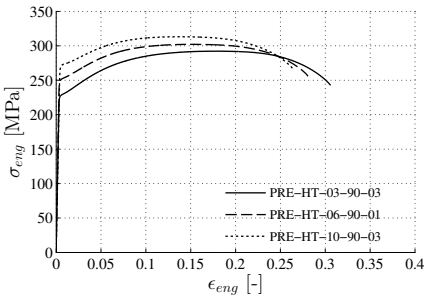

(g) Representative tests.

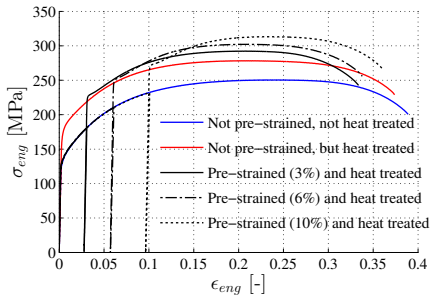

(h) Effect of HT on pre-straining.

Figure 4.3: Engineering stress-engineering strain curves for UT tests with pre-straining and heat treatment. The selected representative curves are indicated with red colour and are plotted together in (g). (h) shows the effect of heat treatment on the pre-straining.

The 45 degree direction exhibits highest flow stress while the 30 degree direction exhibits the lowest.

During the preparations for test UT-WOHT-90-03, the specimen was accidentally loaded before the data logging was started. Plastic deformations occurred, which explains the discontinuous behaviour in Figure 4.1g. Despite this, the result was similar to the two other tests.

Figure 4.2 presents the results from the UT tests with HT and the selected representative curves are indicated with red colour and plotted together in Figure 4.2h.

Slightly more scatter was observed for the heat treated material than for the material without heat treatment. However, the scatter in results from tests in each direction (Figure 4.2a through 4.2g) is negligible compared to the scatter between the representative curves (Figure 4.2h). Again some anisotropy in the flow stress is observed. The 45 degree direction exhibits highest flow stress while the 30 degree direction exhibits the lowest.

By comparing Figure 4.1h and 4.2h it is evident that heat treatment increases the strength and reduces the ductility of the material. The maximum force was increased by approximately 11 %. Results from the UT test in the 90 degree direction with and without heat treatment are compared in the prospective Figure 4.3h.

4.1.2 Pre-strained uniaxial tension

The results of the UT tests with pre-straining followed by heat treatment are shown in Figure 4.3. The pre-straining is shown in Figure 4.3a to 4.3c and the subsequent tests after HT are shown in Figure 4.3d to 4.3f for the different levels of pre-straining. The selected representative tests after heat treatment are indicated with red colour and plotted together in Figure 4.3g. Again, little scatter is observed. Figure 4.3h includes representative curves for different values of pre-straining, the subsequent tests until fracture and tests without pre-straining for both heat treated and not heat treated material. Deliberately, this shows the effect of heat treatment on pre-straining.

As seen in Figure 4.3h it is evident that pre-strained specimens with subsequent heat treatment exhibits higher strength than specimens with heat treatment but no pre-straining. While the pre-straining combined with HT does not affect yielding (i.e. the yielding points lie on the HT curve), the hardening is strongly affected. This is linked to the precipitation of alloying elements interacting with the dislocations issued from the pre-straining. It is also seen in Figure 4.3h, that the ductility seem to be reduced for the pre-strained and subsequently heat treated material compared to material without pre-straining.

4.1.3 Plane strain tension

Results from PST tests are presented in Figure 4.4. Representative curves are indicated with red and plotted together in Figure 4.4e. High repeatability is observed for the PST tests. The strength is increased and the ductility reduced for heat treated material. No anisotropy is observed between the 0 degree and the 90 degree directions.

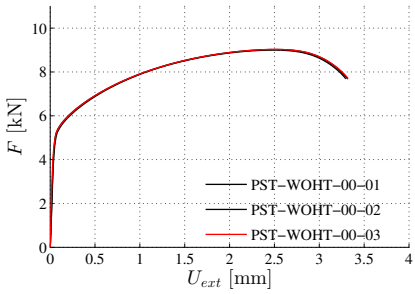

(a) Without HT, 0 degree direction.

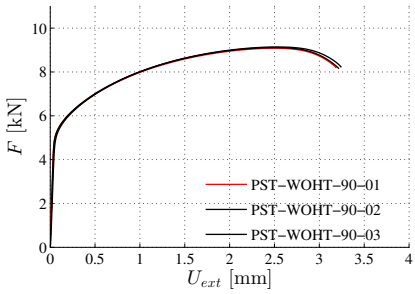

(b) Without HT, 90 degree direction.

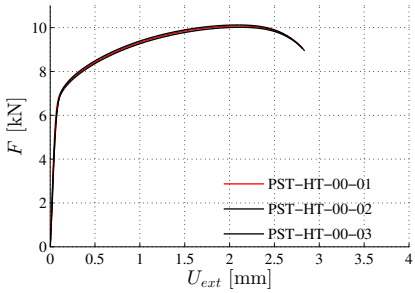

(c) With HT, 0 degree direction.

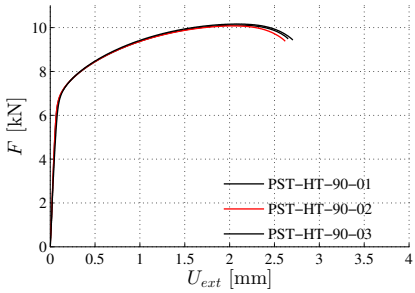

(d) With HT, 90 degree direction.

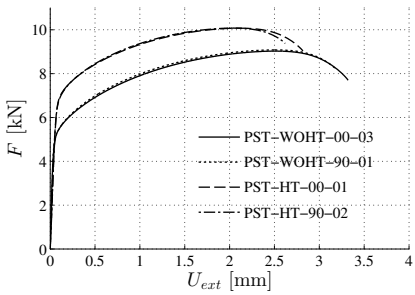

(e) Representative tests together.

Figure 4.4: Force-displacement curves for PST tests. The selected representative curves are indicated with red colour and are plotted together in (e).

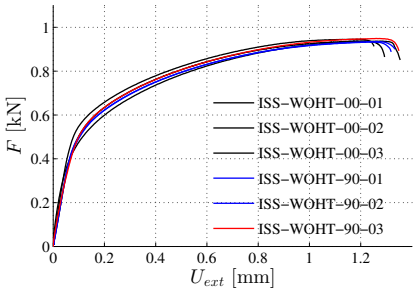

(a) Without HT.

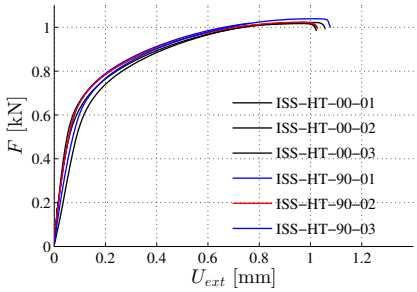

(b) With HT.

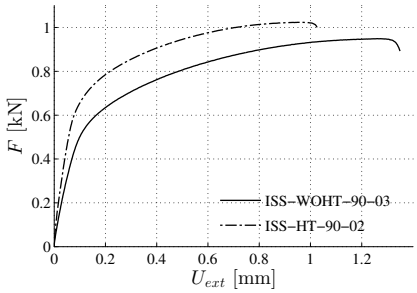

(c) Representative tests without and with HT.

Figure 4.5: Force-displacement curves for ISS tests. The selected representative curves are indicated with red colour and are plotted together in (c).

4.1.4 In-plane single shear

Figure 4.5 shows the results from the ISS tests. Representative curves are indicated with red and plotted together in Figure 4.5c. As expected in Section 3.1.4, the results are similar for the 0 degree and the 90 degree directions.

More scatter is observed for the ISS tests than for UT and PST. Investigation of the broken ISS specimens indicates that the deformation mode involves twisting. Additionally, out-of-plane deformations are clearly observed. The specimens were susceptible to twisting due to the support using a smaller pin diameter than the hole in the specimens. The scatter in Figure 4.5a and Figure 4.5b may thereby be a result of the gripping. Regarding the effect of heat treatment, the same trend is observed for ISS as for UT and PST. Heat treatment increases the strength and reduce the ductility of the material.

4.2 Riveted single connector tests

Between three and five repetitions were performed for all riveted single connector tests. Regardless of the number of repetitions, the results from three tests are presented. As before, the *top* sheet refers to the sheet with the rivet head. The *upper side* of a sheet is the side where the rivet penetrated and the *underside* is the opposite side. The current work will be related to Porcaro et al. [9], where failure modes of self-piercing rivet connections were described.

4.2.1 Cross

Results from the cross tests in the three directions are plotted in Figure 4.6. The measured force level was similar for the repetitions in each direction, but significant differences were observed between the different loading angles. Similarly, the same deformation mode was observed for each repetition, but differed between the loading angles.

For pure normal loading (C-0 test), a near piecewise linear force was measured up to a maximum value of approximately 4.4 kN, as seen in Figure 4.6a. The corresponding displacement was roughly 13 mm. According to the figure, the connection failed shortly after maximum force was reached. After elastic deformations, the top and bottom sheets were deformed around the rivet to the configuration shown in Figure 4.7. A gradual deformation into this state explains the linear plastic part of the load curve. As shown in Figure 4.8, the test setup triggered a deformation mode which inverted the part of the bottom sheet pressed into the die, such that the diameter of the hole around the rivet legs was increased. When a critical opening of the hole was reached, the rivet was released almost instantaneously from the bottom sheet. As seen in Figure 3.8, the diameter of the bottom part of a rivet is smaller than the head. This, in addition to the rivet pull out resistance in the sheets, made the rivet fail from the bottom sheet in all C-0 tests. According to [9], this mode was named *Fs4*.

In Figure 4.6b the force-displacement curves from the C-45 test are displayed. The behaviour is highly non-linear, and some resistance is seen after a maximum force of ap-

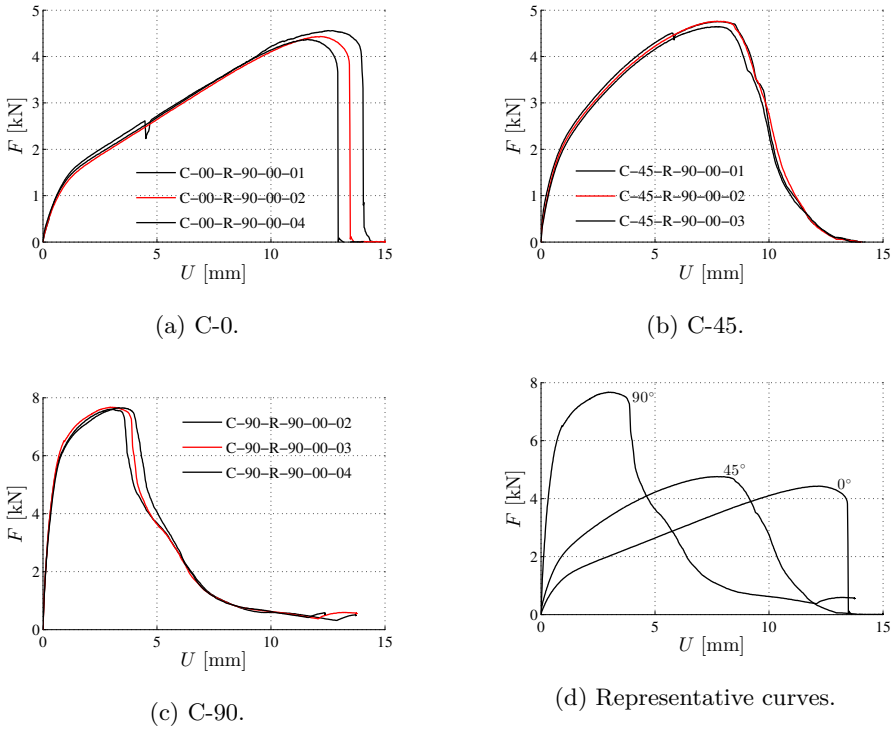

(a) C-0.

(b) C-45.

(c) C-90.

(d) Representative curves.

Figure 4.6: Force-displacement curves from riveted cross tests. Representative curves are indicated with red colour and are plotted together in (d).

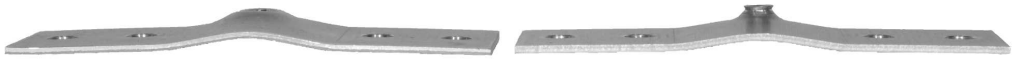

Figure 4.7: Riveted C-0 test specimen after deformation. The upper side of the bottom sheet is seen to the left and underside of the top sheet is seen to the right.

Figure 4.8: Rivet connection from C-0 test after deformation. The underside of the bottom shown.

Figure 4.9: Riveted C-45 test specimen after deformation. The upper side of the bottom sheet is seen to the left and the underside of the top sheet is seen to the right.

(a) Upper side of bottom sheet.

(b) Upper side of bottom sheet.

(c) Underside of top sheet.

Figure 4.10: Rivet connection from C-45 test after deformation.

proximately 4.8 kN is reached. The displacement for maximum force was roughly 8 mm. The shape of the curve is very similar for all tests. The deformed specimen is shown in Figure 4.9. Considering the deformation of the specimen, both sheets deformed firstly in the vicinity of the rivet such that the loading angle on the rivet was reduced to less than 45 degrees, and a larger tensile force component was introduced. Simultaneously to the sheet deformation, the rivet rotated down in the top and out of bottom sheet. At a late deformation state the rivet was held by the one side of the hole in the top sheet and the opposite side of the hole in the bottom sheet. The mark seen in Figure 4.10a and the crack under the bottom sheet seen in Figure 4.10b were produced during this state. The rivet connection failed when the material in the top plate gave off and fractured such that the rivet head slipped through (displayed in Figure 4.10c) and the rivet bottom slid out of the bottom plate. The rivet was entirely detached from both sheets after failure in all tests. This failure mode is close *Fs1* in [9].

The force-displacement curves from pure shear loading (C-90 test) are shown in Figure 4.6c. The maximum force was approximately 7.5 kN with a corresponding displacement of around 3 mm. As for the 45 degree loading angle, some resistance is observed after the peak, but this is believed to essentially be a frictional force caused by jamming of the rivet between the sheets. The deformed specimen is shown in Figure 4.11. The deformation throughout the test may be characterized as an extreme version of the deformation described for the 45 degree loading angle. As seen in Figure 4.12a and 4.12b, a similar, but greater mark and crack were observed compared to the 45 degree loading angle. Similarly as observed for the 45 degree loading direction, the connection failed by the rivet head failing from the top sheet. The fracture mode is seen in Figure 4.12c, and it is observed that some material around the rivet was torn out from the top sheet. The rivet was still attached to the top sheet at the point when the connection failed in all tests. Pocaro et al. [9] called this mode *Fs1*.

In Figure 4.6d, the representative tests from the three loading directions are plotted

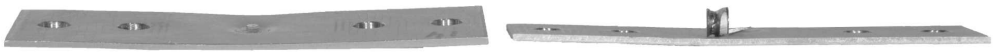

Figure 4.11: Riveted C-90 test specimen after deformation. The upper side of the bottom sheet is seen to the left and the underside of the top sheet is seen to the right.

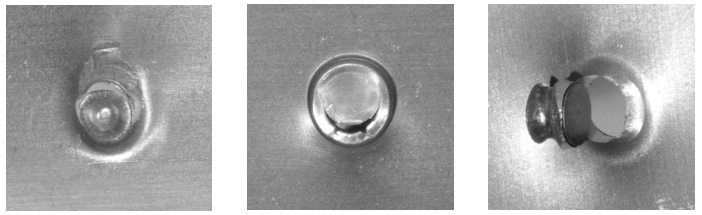

(a) Upper side of bottom sheet.

(b) Underside of bottom sheet.

(c) Underside of top sheet.

Figure 4.12: Rivet connection from C-90 test after deformation.

together. The maximum force was similar for the C-0 and C-45 tests, and significantly higher for the C-90 test. The corresponding displacement was largest for pure normal loading and least for pure shear loading. It should be noted that deformation of the sheets contribute significantly to the global displacement for C-0 and C-45. For C-0 the rivet failed from the bottom sheet while it failed from the top sheet for C-45 and C-90. The rivet was rotated out for the 45 and 90 degree load directions which gave a more ductile response than the pop out experienced for pure normal loading. This is the reason for the slope of the post-fracture portion of the curves. It should be noted that deformation of the sheets is the main reason to global deformations, and this is greatly affected by the loading angle and the clamping. A local deformation measure should be used rather than a global to compare the deformation of the connections directly, but this is not feasible on such specimens.

4.2.2 Single lap-joint

Results from the SLJ tests with rivets are shown in Figure 4.13. Unbroken and stippled lines indicate where the extensometer opening and cross head displacement were used as displacement measures, respectively. High repeatability is observed for the SLJ tests. The maximum force is roughly 7 kN for both material orientations and the corresponding displacement is approximately 2 mm. The riveted connection is slightly more ductile for the material oriented in the 90 degree direction than for the 0 degree direction, due to the material anisotropy.

Deformation of the sheets and the rivet was similar for all SLJ tests, and a deformed

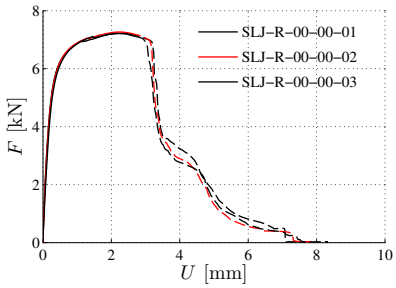

(a) Both sheets 0 degree direction.

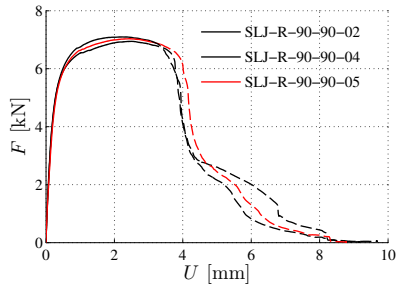

(b) Both sheets 90 degree direction.

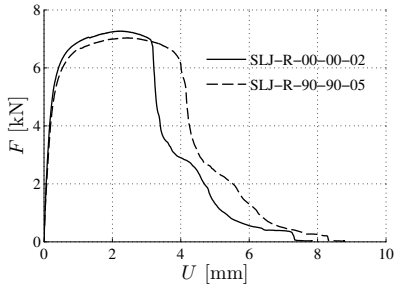

(c) Representative curves.

Figure 4.13: Force-displacement curves from riveted SLJ tests. Unbroken and stippled lines indicate where the extensometer opening and cross head displacement were used as displacement measures, respectively. Representative curves are indicated with red colour and are plotted together in (c).

Figure 4.14: Riveted SLJ test specimen after deformation. Top sheet is to the right.

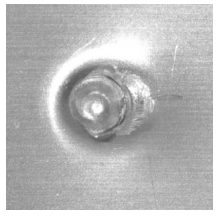

(a) Upper side of bottom sheet.

(b) Underside of bottom sheet.

(c) Underside of top sheet.

Figure 4.15: Rivet connection from SLJ test after deformation.

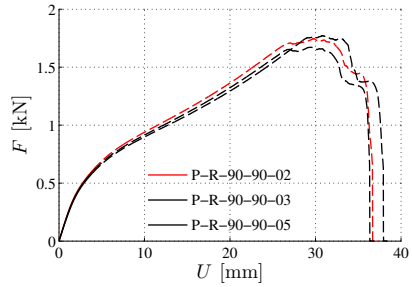

Figure 4.16: Force-displacement curves from riveted P tests. Unbroken and stippled lines indicate where the extensometer opening and cross head displacement were used as displacement measures, respectively. Representative curve is indicated with red colour.

specimen is shown in Figure 4.14. The first visible deformation of the specimen included bending of the two sheets such that the rivet rotated from a pure shear to include a tensile load component, and the rivet was gradually rotated out from the top and bottom sheet. The failure was caused by fracture in the top sheet such that the rivet rotated out of the bottom sheet. The rivet connection after deformation is shown in Figure 4.15. The fractured material remained connected to the rivet, as displayed in Figure 4.15c. The crack observed in Figure 4.15b was on the same side of the rivet connection as where the rivet was rotated down into the bottom sheet. This fracture mode is the same as described for C-45 and C-90.

4.2.3 Peeling

The results from riveted P tests are plotted in Figure 4.16. Some scatter is observed for the maximum force level, which was roughly 1.7 kN, and the corresponding displacement. According to the figure, the evolution of the force level was similar for all tests. The riveted connection failed shortly after maximum force was reached. It should be noted that the deformation was mainly caused by bending of the sheets.

A deformed peeling specimen is shown in Figure 4.17. The deformation pattern observed throughout each test was very similar. Firstly, the initially 90 degree bend was opened at the same time as a new bend appeared near the rivet. For the top sheet the second bend occurred along a line roughly crossing the head of the rivet, while for the bottom sheet the bend was found along a line adjacent the bottom of the rivet. It is notable that the bottom part of the rivet connection, the one pressed into the die, appears as stiffer, causing the position of the bend. The bend in the top sheet crossing the rivet head weakened the connection significantly, and enabled out-rotation of the rivet from the top sheet. In the late part of the test, the rivet head was only attached to the top of the hole in the top sheet in Figure 4.17. As illustrated in Figure 4.18b and 4.18c, rifts perpendicular to the top sheet were formed when the rivet pierced the top sheet. This late stage of deformation of the specimen explains the jagged part of force curves around maximum force (see Figure 4.16). According to [9], this is mode *Fp2*.

Figure 4.17: Riveted P specimen after deformation. Top sheet is to the right.

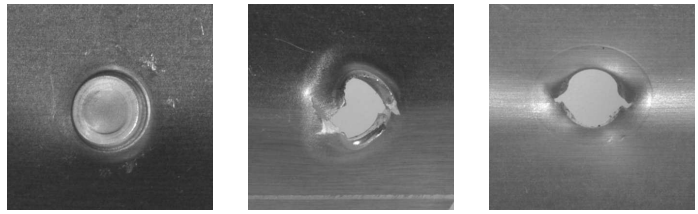

(a) Underside of bottom sheet.

(b) Underside of top sheet.

(c) Upper side of top sheet.

Figure 4.18: Rivet connection in P test after deformation.

4.3 Screwed single connector tests

Likewise the riveted single connector tests, results for three repetitions are presented for the screwed single connector tests.

Recall that the *top* sheet refer to the sheet with the screw head and the *upper side* is the side where the screw penetrated and the *underside* is the opposite side.

4.3.1 Cross

Results from the cross tests in the three directions are plotted in Figure 4.19. For each loading angle, the same deformation mode was observed for each repetition.

The cross test for pure normal force (C-0) showed a near piecewise linear force-displacement relationship, as displayed in Figure 4.19a. The force increased until a sudden failure, typically nearly 3 kN, with a corresponding displacement around 8-9 mm. The deformed specimen is shown in Figure 4.20. The screw was pulled out from the bottom sheet and the threads in the bottom sheet were levelled out by the screw.

As observed from Figure 4.19b, also here a near piecewise linear force-displacement relationship was observed from the C-45 test. In this case the maximum force and failure were just above 3 kN with a correspond displacement of roughly 7 mm. The deformed specimen if shown in Figure 4.21. In this case, the threads in the bottom sheet were levelled out on one side of the hole while mostly preserved on the other side. This is shown in Figure 4.22.

From Figure 4.19c, it is evident that a rather stiff response was observed for pure shear

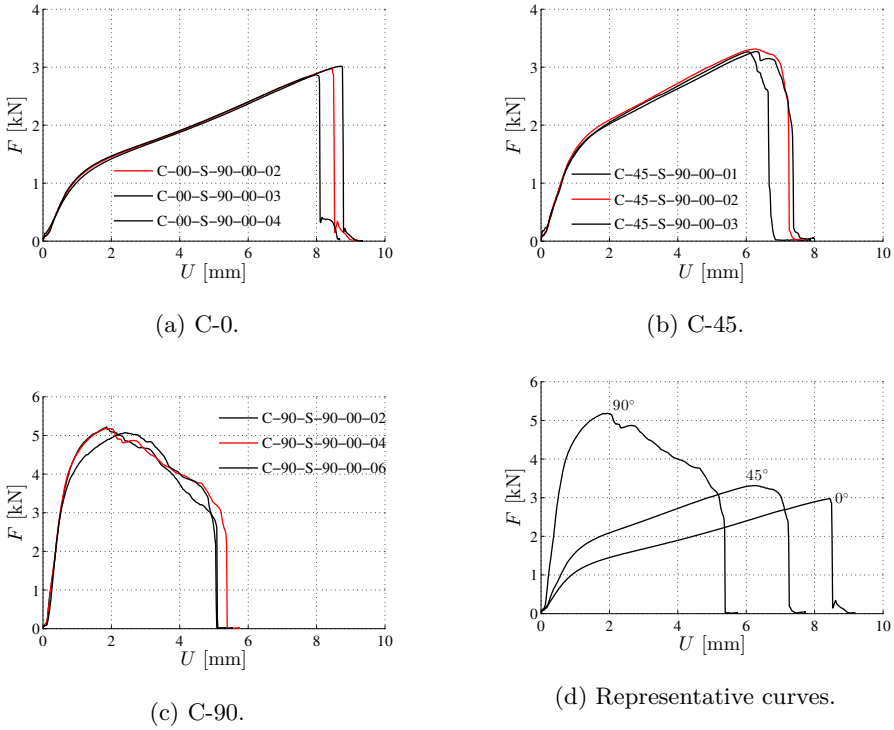

(a) C-0.

(b) C-45.

(c) C-90.

(d) Representative curves.

Figure 4.19: Force-displacement curves from screwed C tests. Representative curves are indicated with red colour and are plotted together in (d).

Figure 4.20: Screwed C-0 test specimen after deformation. The upper side of the bottom sheet is seen to the left and underside of the top sheet is seen to the right.

Figure 4.21: Screwed C-45 test specimen after deformation. The upper side of the bottom sheet is seen to the left and the underside of the top sheet is seen to the right.

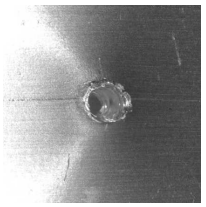

(a) Upper side of bottom sheet.

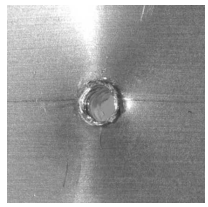

(b) Upper side of bottom sheet.

Figure 4.22: Screw connection from C-45 after deformation.

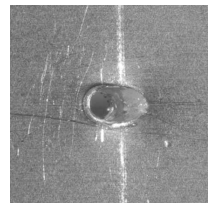

(a) Upper side of bottom sheet.

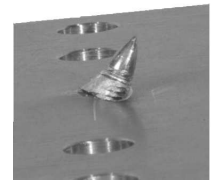

(b) Underside of top sheet.

Figure 4.23: Screw connection from C-90 test after deformation

Figure 4.24: Screwed C-90 test specimen after deformation. The upper side of the bottom sheet is seen to the left and the underside of the top sheet is seen to the right.

loading (C-90). After the maximum of roughly 5 kN, the force was linearly reduced until a sudden fracture occurred for approximately 3 kN. The displacement was around 2 mm for maximum force and 5 mm when the specimen fractured. Little global deformations were observed in the sheets. The screw was rotated approximately 30 degrees by the shear force before a shear fracture occurred in the upper side of the bottom sheet. As shown in Figure 4.23, the threads were levelled out on the loaded side of the hole in the bottom sheet and the fractured material remained connected to the screw. The deformed specimen is shown in Figure 4.24.

In Figure 4.19d, the representative curves from each loading direction are plotted together. Maximum force is highest for C-90 test and similar for the two others. The sheets were most deformed for pure normal loading and least for pure shear. As for rivets the deformation of the sheets is the main reason to global deformations, and this is greatly affected by the loading angle and the clamping.

4.3.2 Single lap-joint

Results from the screwed SLJ tests in both directions are plotted in Figure 4.25. As shown in Figure 4.25c the results are similar for the two directions. The maximum force was nearly 5 kN, and the corresponding displacement was roughly 2 mm. From this point the force level was halved before failure at 5 mm. Failure was observed for displacements around 5 mm.

The specimen during deformation is illustrated in Figure 4.26. Firstly, the sheets were bent such that the screw was no longer horizontal (see Figure 4.26b). This continued until the screw was gradually pulled out (see Figure 4.26c). From this point the connection is believed to have fractured. However, due to friction between the screw and the sheets,

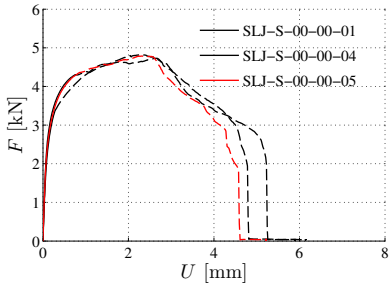

(a) Both sheets 0 degree direction.

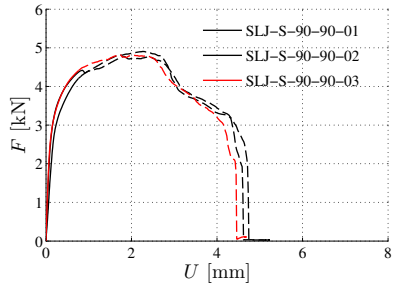

(b) Both sheets 90 degree direction.

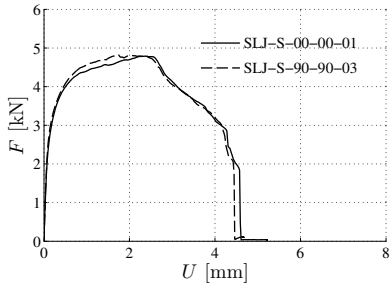

(c) Representative curves.

Figure 4.25: Force-displacement curves from screwed SLJ tests.

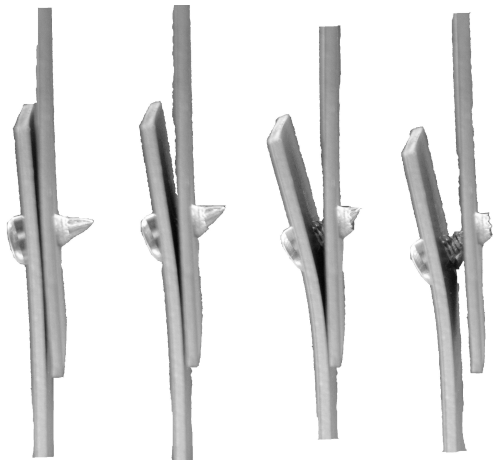

(a) (b) (c) (d)

Figure 4.26: Deformation during screwed SLJ test.

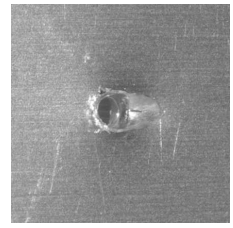

(a) Upper side of bottom sheet.

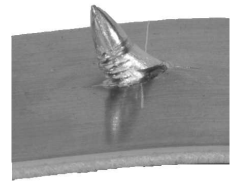

(b) Underside of top sheet.

Figure 4.27: Screw connection in SLJ tests after deformation.

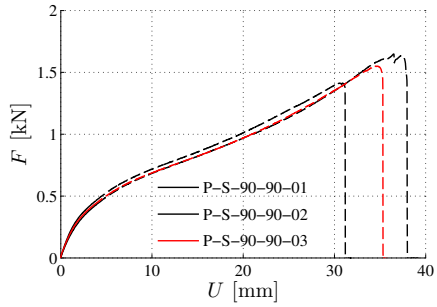

Figure 4.28: Force-displacement curves from screwed P tests. Unbroken and stippled lines indicate where the extensometer opening and cross head displacement were used as displacement measures, respectively. Representative curve is indicated with red colour.

some strength in the connection was still observed. This explains the near linear reduction of force after the peak force. For non-monotonic loading, this strength would probably vanish. Figure 4.26d shows the deformation just before complete pull-out. As observed in Figure 4.27, fractured material remained connected to the screw, indicating that failure occurred by threading.

4.3.3 Peeling

Results from the screwed peeling tests are plotted in Figure 4.28. In a similar manner as for the rivet connection, a near piecewise linear force-displacement relationship was observed. The connection failed just after a maximum force of approximately 1.5 kN was reached. The corresponding maximum displacement was roughly 35 mm. Some scatter was observed both for the maximum force and the maximum displacement. Most of the global displacement was caused by bending of the sheets.

Figure 4.29 shows a deformed specimen, and Figure 4.30 shows different stages of deformation. The deformation of the specimen was very similar for each test. Firstly, the bending of the sheets were symmetric such that the screw remained vertical. Next, the sheets were bent into the configuration in Figure 4.30a. It should be noted that the bend in the top sheet was adjacent to the screw head while it was crossing the centre line of the screw in the bottom sheet. Apparently, the screw head stiffens the top sheet. This behaviour is exactly the opposite of the rivet one. The deformation pattern continued, as shown in Figure 4.30b. The specimen shortly after failure is shown in Figure 4.30c. When inspecting the specimen it was clear that the hole in the bottom sheet was oval. Additionally, small rifts were observed in the bottom sheet from the hole and in the direction along the bend in the sheet.

Figure 4.29: Screwed P test specimen after deformation. Top sheet is to the right.

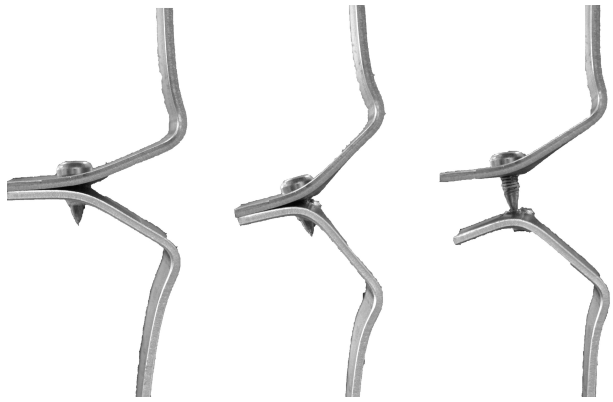

(a) (b) (c)

Figure 4.30: Deformation stages during screwed P test.

4.4 Comparison of connector tests

In this section the results from all riveted and screwed single connector tests are compared and discussed. In Figure 4.31, a synthesis of the results are presented. No plastic deformations were observed in the rivets or screws. Generally, the rivet connection was significantly stronger than the screw connection. It should be emphasized that the nominal diameter was 5 mm for the rivets and 4 mm for the screws. Consequently, increased strength of the rivet connection is expected and a direct comparison of maximum force levels should be done with care. A smaller diameter of the connections implies higher curvature of the holes in the sheets and correspondingly higher stress concentration.

4.4.1 Connector tests

As observed in Figure 4.31d the cross test for pure shear loading and the SLJ are very similar. In the figure, the SLJ tests with material orientation corresponding to the loading direction in the C-90 test are plotted. By inspection of the specimens, it is evident that the same fracture mode of the connection was observed in the two tests, both for rivets and screws. Higher maximum force and increased ductility is observed for the C-90 test compared to SLJ. This is probably explained by the two-sided clamping of the cross specimens, which gave a high resistance to out-of-the-plane deformations. For SLJ tests, such deformations were not constrained, and allowed for a bend in the top sheet, as

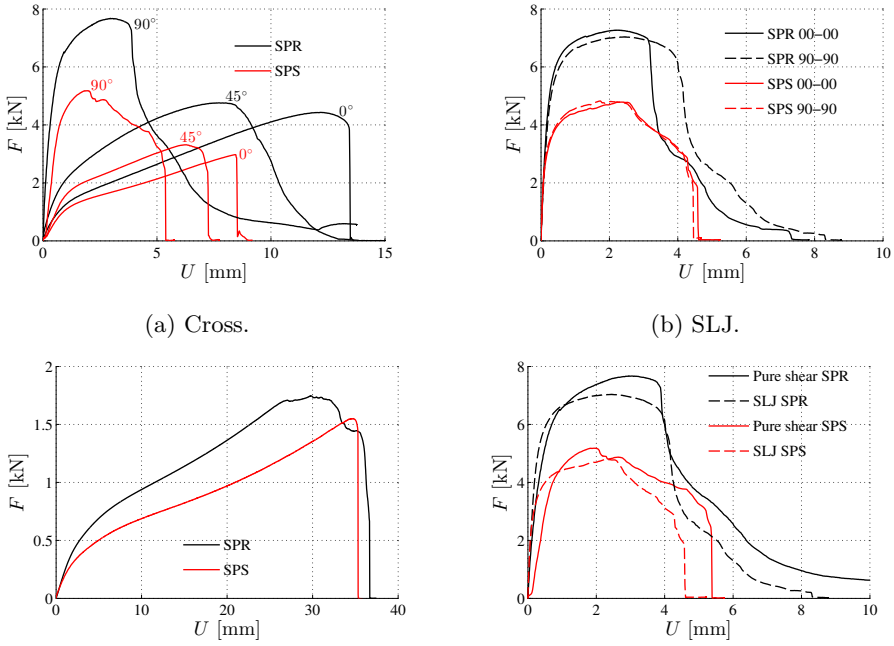

(a) Cross.

(b) SLJ.

(c) Peeling.

(d) C-90 and SLJ.

Figure 4.31: Comparison of results from single-connector tests for rivets and screws.

Table 4.1: Average maximum force and average of corresponding displacements for single-connector tests.

	SPR		SPS		(SPR - SPS)/ SPS	
Test	$\bar{F}_{\max}$ [kN]	$\bar{U}_{\bar{F}_{\max}}$ [mm]	$\bar{F}_{\max}$ [kN]	$\bar{U}_{\bar{F}_{\max}}$ [mm]	$\bar{F}_{\max}$	$\bar{U}_{\bar{F}_{\max}}$
C-0	4.45	12.11	2.95	8.38	51 %	45 %
C-45	4.72	7.70	3.29	6.20	44 %	24 %
C-90	7.65	3.09	5.16	2.04	48 %	51 %
SLJ-00-00	7.24	2.25	4.80	2.44	51 %	-8 %
SLJ-90-90	7.03	2.42	4.84	1.95	45 %	24 %
P	1.73	30.03	1.54	33.95	13 %	-12 %

shown in Figure 4.14 and Figure 4.26d. Consequently, a minor tensile load component was introduced for the SLJ tests. For the C-90, however, a stabilizing, compressive force prevented the sheets from separating, such that the pure shear load was better sustained than for the SLJ test.

For the riveted SLJ tests, a reduction in maximum force level and increased ductility was observed for the material oriented in the 90 degree direction compared to the 0 degree direction (see Figure 4.31b). In both cases fracture was seen in the top sheet material surrounding the rivet and a subsequent rotation of the rivet out of the bottom sheet. By inspecting the deformed specimens closely, a small difference in the angle of the bends of the specimens (see Figure 4.26d) was observed. The bend in the top sheet was slightly larger for the specimens with material oriented in the 90 degree direction. Increasing the angle increases the tensile load component in the connection. As seen from the results from the cross tests (see Figure 4.31a), introduction of tensile forces reduces the maximum force level and increases the ductility of the connection. From Figure 4.1h it is observed that the hardening of the material is larger in the 0 degree direction than the 90 degree direction. A possible explanation to the discussed matter then reads; higher hardening leads to smaller bending of the specimen, which in turn introduce smaller tensile load components and thereby higher maximum force and less ductility. No effect of material orientations was, however, observed for screws. A possible explanation for this is the diameter of the screws. As the screw has smaller diameter than the rivet, the amount of material loaded by the rivet is larger compared to for the screw. Thus, the effect of anisotropy of the sheets is less pronounced for the screws.

4.4.2 Rivets and screws

The results from the cross tests are compared in Figure 4.31a, and it is noted that the shapes of the curves are similar for the two connections. According to Table 4.1, the average maximum force was 51 %, 44 % and 48 % higher for the rivet than for the screw connection in the 0, 45 and 90 degree loading direction. The average of the corresponding displacements was increased by 45 %, 24 % and 48 %, respectively. It should be emphasized that possible capacity after maximum force is concealed in the numbers. For each loading direction, the shapes of the force-displacement curves were similar.

For the C test with 0 degree loading angle, a snapping fracture was observed for both connections. For the rivet connection, the fracture was a result of plastic deformations around the legs of the rivet such that the rivet was released from the bottom sheet. For the screw, the fracture was a result of the threads in the bottom sheet levelling out. The fracture modes are comparable. As observed from the figure, the connection was stiffer for the rivets than the screw. This additional stiffness is probably explained by plastic deformations in the sheet material around the rivet, due to the riveting process. For the screw, however, the sheets does not seem to be significantly stiffened by adding the screw. By inspecting the deformed specimens (Figure 4.7 and 4.20), it is obvious that more plastic deformations are observed for the riveted specimen than for the screwed for the same displacement.

The average maximum force was approximately 50 % higher for rivets than screws in 0, 45 and 90 degree loading angle cross tests. The same increase was observed for the

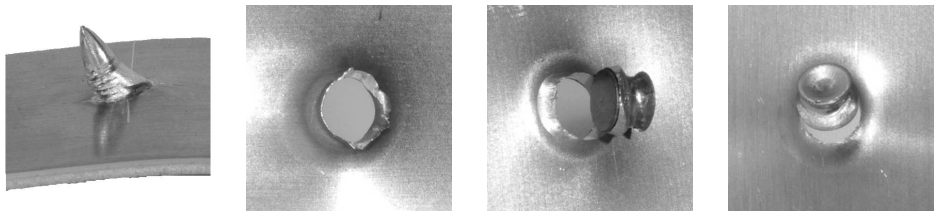

(a) SLJ, screw. (b) C-45, rivet. (c) C-90, rivet. (d) SLJ, rivet.

Figure 4.32: Repetition of fracture modes from C-45, C-90 and SLJ tests. The underside of the top sheet is shown.

corresponding displacements, except for the 45 degree loading angle, which increased by the halve (24 %). Stated differently, the screwed connection was more ductile in the 45 degree loading than the riveted compared to the 0 and 90 degree loading direction. For the rivet, the same fracture mode was observed in the C-45 and C-90 test. This mode causes the reduced ductility compared to the screws, and is explained in next paragraph.

The C-90 and SLJ are discussed together, and the results are compared in Figure 4.31d. The shape of the curves are very similar for rivets and screws up to maximum force, both in the C-90 and in the SLJ tests. Inspection of the deformation of the connections up to this point revealed great similarities. This included a gradual rotation of the connection down from the top sheet and out of the bottom sheet. After maximum force was reached, however, the behaviour was more ductile for the screw than the rivet connection. The fracture modes of the connections are repeated for convenience in Figure 4.32. For the screw, the rotation continued and the force was linearly reduced until pull-out by a shear fracture in the bottom sheet (Figure 4.32a). The rivet, however, fractured from the top sheet. The rivet head with surrounding material was torn out such that the rivet rotated out of the bottom sheet (clearly displayed in Figure 4.32c and 4.32d). The same mode, but less prominent, was observed for the C-45 test (Figure 4.32b). This tear-out of the rivet from the top sheet explain the abrupt force-drop and negligible capacity shortly after maximum force was reached. A larger rivet head would increase the resistance to this deformation mode due to larger contact surface.

According to Table 4.1, the maximum force in the peeling tests was 13 % higher for the rivets than for screws and inverted results are seen for the corresponding displacements. This clearly deviates from the previously observed trend, and implies that the resistance against fracture was higher for the screwed specimens relative to the riveted for the peeling test. Considering the fracture, the most obvious difference is that the rivets failed from the top sheet while the screws failed from the bottom. Somehow, the bottom plate of the rivet connection behaved similar to the screw head, and stiffened the respective sheet significantly. The sharp edge on the head of the rivet cut through the top sheet, and probably this problem is increased by increasing the head diameter. The fracture of the screw, however, was similar as observed for other tests and included rotation until pure pull-out.

To conclude, the strength of the rivet connection was approximately 50 % higher than for the screw. In pure normal load both connections fractured similarly and from the bottom

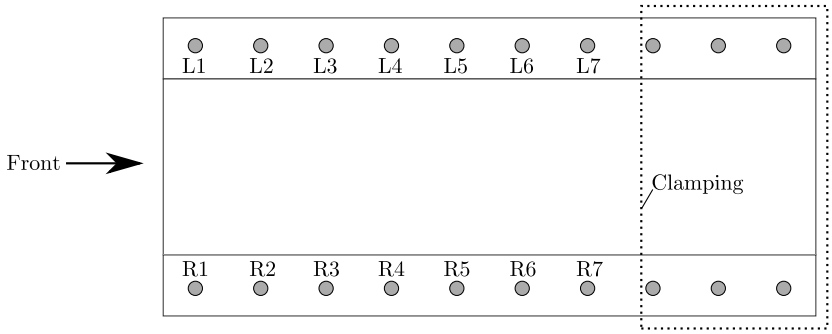

Figure 4.33: Name system for the connections. L1 refers to the first rivet on the left side.

sheet. For all other tests the rivet fractured from the top sheet, often including rotation out of the bottom sheet. For screws, the same fracture was observed in all tests, which included a gradual rotation until pull-out from the bottom sheet.

4.5 Riveted component test

In this section results from the dynamic and static riveted component tests are presented. Results from dynamic tests are emphasized and results from static tests serves as references. The component tests are described according to Figure 4.33. As explained in Section 3.4, the specimen is described from the impactor's perspective of view, such that *left side* is left to the *front*. L1 means rivet 1 on the left side etc.

The same progressive buckling mode was observed for all crash boxes, both for dynamic and static tests, and is shown in Figure 4.34 for CB7D-R. As the same mode was triggered in each test, the triggers presented in Figure 3.19 worked as intended.

4.5.1 Dynamic

In total seven dynamic riveted component tests were performed and the results from five of them are presented. The remaining two test were discarded due to slightly different deformation modes caused by geometrical imperfections, triggering a large amount of fracture in the sheets. The same global buckling mode was observed for the five chosen crash box tests and the deformed specimens are shown in Figure 4.35 from different points of view. From Figure 4.35b it is noted that the folds are smaller and have higher curvature near the front. Deformation of the crash boxes during dynamic testing was recorded by a high-speed camera, and is shown for one specimen in Figure 4.36. Measurements from the test setup for each test is found in Table A.1.

As explained in Section 3.4.1 three different measures of displacement were performed in the tests; high-speed camera measurement of the trolley displacement, integration of the force data and laser measurement of the trolley displacement. Comparisons of the three measures are shown for test CB7D-R in Figure 4.37. Figure 4.37a shows the measured

(a) Right and top.

(b) Top.

(c) Left.

(d) Bottom.

(e) Front.

Figure 4.34: Details of the buckling mode observed in crash box tests.

(a) Front.

(b) Left.

(c) Right.

(d) Top.

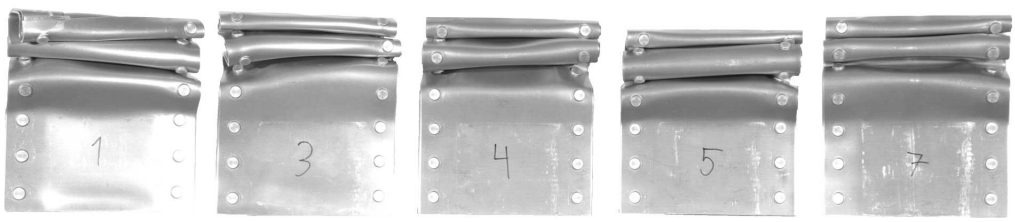

(e) Bottom.

Figure 4.35: Deformation modes from riveted, dynamic CB tests.

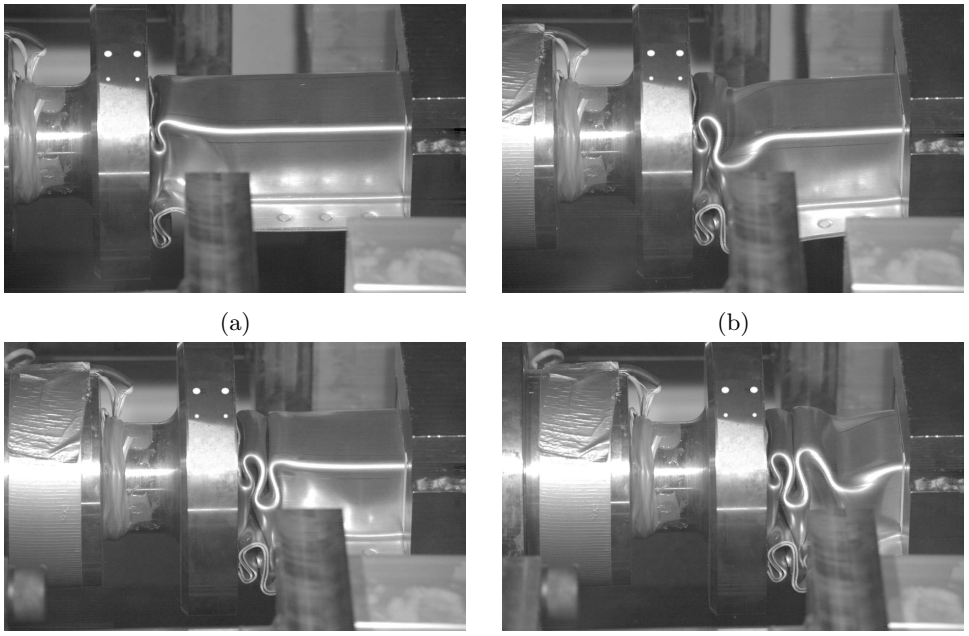

(a) (b)

(c) (d)

Figure 4.36: Deformation of crash box during dynamic test as recorded by the high-speed camera.

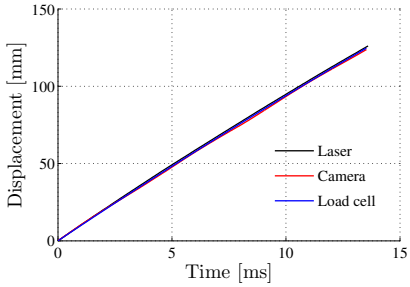

(a) The three displacement measures plotted together.

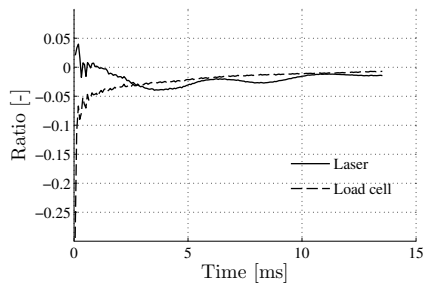

(b) Displacement ratios, where 0 implies no difference to the displacement measured by the camera.

Figure 4.37: Comparison of displacement measures in dynamic riveted CB tests. The results displayed are for CB7D-R.

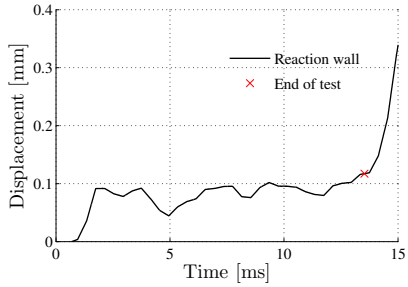

Figure 4.38: Reaction wall displacement for test CB7D-R.

displacements as function of time. Evidently, the measurements are very similar for all three methods. Displacement ratios r_{laser} and $r_{\text{load cell}}$, computed as

$$r_{\text{laser}} = \frac{U_{\text{laser}} - U_{\text{camera}}}{U_{\text{camera}}} \tag{4.3}$$

and

$$r_{\text{load cell}} = \frac{U_{\text{load cell}} - U_{\text{camera}}}{U_{\text{camera}}} \tag{4.4}$$

are plotted in Figure 4.37b. U_{laser}, $U_{\text{load cell}}$ and U_{camera} are displacement measured by the laser, load cell and camera, respectively. Additionally, the measured displacement of the reaction wall is shown in Figure 4.38. As seen, the reaction wall displacement was less than 0.1 mm for almost the entire test and is hence considered negligible. From this it is concluded that all measures of displacement are valid. The load cell measurements are used henceforth.

The mean force F_m was calculated as the absorbed energy E divided by the total defor-

mation u of the specimen,

$$F_m(u) = \frac{E(u)}{u} \tag{4.5}$$

The absorbed energy is the area under the force-displacement curve, calculated by

$$E(u) = \int_0^u F(\hat{u})\,\mathrm{d}\hat{u} \tag{4.6}$$

where F is the force, u is the crushing distance and $\hat{u}$ is pseudo crushing distance.

4.5.1.1 Results

The force-displacement history for the five tests are presented in Figure 4.39. The measured, filtered and mean force for all tests are plotted against displacement in Figure 4.39a, 4.39b and 4.39c, respectively. As seen, high repeatability is evident with respect to the initial peak force and the post-buckling behaviour, both for filtered and mean forces. The filtered forces are very similar up to approximately 60 mm displacement, including initial peaks between 80 and 92 kN. The force level deviates slightly from test to test after 60 mm. The scatter in mean force levels as function of displacement is negligible and indicates high repeatability with respect to the energy absorption. The average mean force for 100 mm displacement was 40.37 kN. The mean force is slightly lower for CB1D-R which probably is related to a major rift in the top sheet, which is further described in Section 4.5.1.3. In Figure 4.39d, the measured, filtered and mean forces are plotted together for CB7D-R. It is observed that most of the initial peaks are omitted for the filtered force. It is also noted that the oscillations in the measured force decrease, as the stress waves are damped out.

4.5.1.2 Deformation and failure of rivets

Deformation and failure modes of the rivets from the five crash box specimens were investigated closely and categorized according to Table 4.2. One or more deformation modes were observed for most of the rivets, and the failure mode was observed for three rivets. The three deformation modes and the failure mode are shown in Figure 4.40. No relative displacement between the sheets was observed.

Three rivets on each side of the specimen were inside the clamping of the crash box and thereby ignored in the categorization. The remaining 14 rivets on each deformed specimen were categorized, which give a total number of 70 relevant rivets. The connections were named according to Figure 4.33. The deformation and failure mode(s) for each specific rivet is found in Table C.1 in the Appendix. The deformation of rivet L7 and R7 were somehow influenced by the clamping of the specimen.

Deformation mode 1 (D1) showed a significant crack in the bottom sheet along the diameter of the bottom of the rivet, as depicted in Figure 4.40a. Even though the crack was clearly visible, it appeared to be shallow and only affecting the part of the bottom sheet within the diameter of the rivet. The bottom sheet around the rivet was still intact. D1 was found for the majority of the rivets and thereby believed to be initiated on an

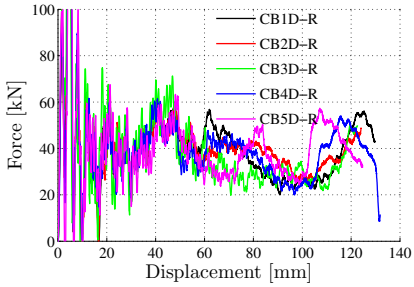

(a) Measured force for all tests.

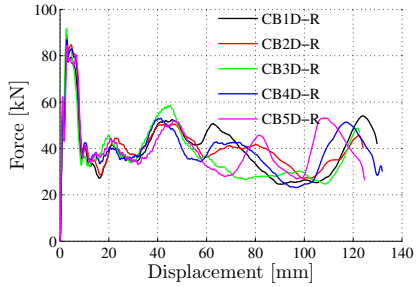

(b) Filtered force for all tests.

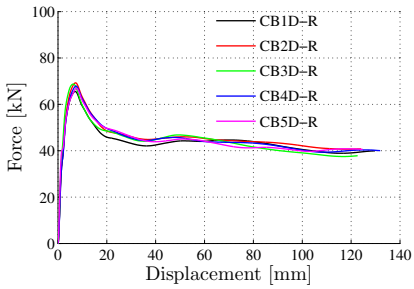

(c) Mean force for all tests.

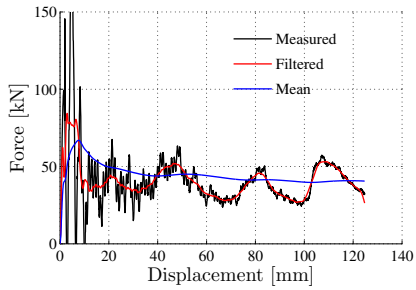

(d) Measured, filtered and mean force for CB7D-R.

Figure 4.39: Measured, filtered and mean force plotted against displacement for all riveted CB tests in (a), (b) and (c) and plotted together for CB7D-R in (d).

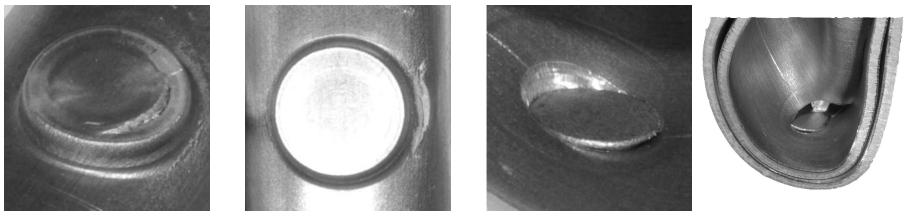

(a) D1. (b) D2. (c) D3. (d) F1.

Figure 4.40: Deformation and failure modes of rivets.

Table 4.2: Deformation and failure modes of rivets for riveted crash box specimens.

Name	Description
No mode	No visible deformation or failure mode
D1	Crack in bottom sheet underneath rivet
D2	Crack in bottom sheet near rivet
D3	Incipient tear-out of rivet from top sheet
F1	Crack in top sheet initiated by rivet

early deformation stage. Furthermore, the deformation mode is believed to be a result of the length of the rivets, and that the mode would be less frequently observed for shorter rivets. Of course, shorter rivets would also lower the strength of the connections.

For deformation mode 2 (D2), the rivet itself holds, but a crack opened in the bottom sheet adjacent to the rivet connection. This mode was most frequently observed where the bottom sheet was outside of sharp folds, as shown in Figure 4.40b. The mode was never observed for a corresponding inwards fold. This accords with observations from the peeling test, where no crack was found for a inward fold (see Figure 4.18a).

Deformation mode 3 (D3) included incipient tear out of the rivet from the top sheet. The mode is shown in Figure 4.40c. The rivet in the figure is a typical D3 rivet. The material of the top plate was clearly affected, but it is uncertain how the strength of the rivet connection was influenced by the deformation mode. This mode is similar to the deformation observed early in the riveted peeling tests.

For failure mode (F1), a crack was observed in the top sheet initiated near the rivet. The most prominent example is displayed in Figure 4.40d. The failure mode is believed to be a well developed case of D3. As long as the rivet head was not entirely visible, covered by material from a crack in the top sheet, the rivet was characterized as F1. This failure mode is very similar to the failure mode observed in the riveted peeling tests.

In Table 4.3 the deformation modes of the rivets of the crash boxes are summarized. The modes N, D1, D2, D3 and F1 were observed for 14 % 73 %, 20 %, 33 % and 7 % of the rivets, respectively. D3 is clearly linked to D1, as the D3 mode was seldom observed without the D1 mode. D2 was either observed alone, combined with D1 or combined with D3. Only one rivet exhibited all three deformation modes. By far, rivet row 4 was most heavily damaged and all failures of rivets were found in this row. By closer inspection, these rivets were subjected to a peeling deformation due to the deformation of the top sheet. D2 an D3 were most frequently observed in the front of the specimen. The specimens were generally less damaged in the rear halve, and rivets on row 7 were the least damaged of all.

Table 4.3: Percent of rivets within each rivet row experiencing deformation and failure mode(s), when all dynamic tests are taken into account. One rivet may have more than one mode and row number refer to Figure 4.33.

Mode	All rivets	Row						
		1	2	3	4	5	6	7
No mode	14	0	30	0	0	0	20	50
D1	73	40	70	90	80	100	80	50
D2	20	90	10	10	30	0	0	0
D3	33	10	10	70	90	10	40	0
D1+D2	7	30	10	0	10	0	0	0
D1+D3	29	0	10	60	80	10	40	0
D2+D3	6	10	0	10	20	0	0	0
F1	7	0	0	0	50	0	0	0

4.5.1.3 Failure in the sheets

Failure in the sheets were observed for all crash boxes and appeared as small cracks in highly deformed areas of the top sheet. All cracks appeared at or in the vicinity of the bends of the sheets, which is the region most affected by the forming process. No failures were observed for the bottom sheet.

In Figure 4.41 examples of failures in the sheets for CB1D-R are shown. As seen, a propagating rift from the front of the top sheet to the second fold is present. This is by far the most severe failure observed for all crash boxes. Consequently, the two first folds on the left side were bent down as crushing proceeded, as depicted in Figure 4.41a and 4.41b. This particular occurrence was not observed for any other crash boxes. Another unique observation for this crash box was rifts along the bend of the plate, as illustrated in Figure 4.41c. A similar rift is seen in Figure 4.41a. In addition, several cracks as shown in Figure 4.41d and 4.41e were observed.

Considering failures in the sheets, very similar observations were done for CB3D-R, CB4D-R and CB7D-R. This included a crack behind the first fold on both sides of the specimen. As illustrated in Figure 4.42 the crack was largest for CB3D-R and smallest for CB7D-R. For CB4D-R and CB7D-R a similar crack was observed behind the second fold, but only on the left side of the specimen. For CB3D-R a second crack was found inside the second fold on the left side. It is noted that cracks are more frequently observed on the left side of the specimen.

For CB5D-R, failure in the sheets was observed inside the second fold on both sides as illustrated in Figure 4.43.

In general the sheets manifested high ductility during deformation and few cracks were observed. None of the cracks are believed to be crucial for the global strength of the crash boxes, except for the rift in CB1D-R. The cracks in the sheets may, however, be considered as locally weakened zones.

(a) Left side and the front.

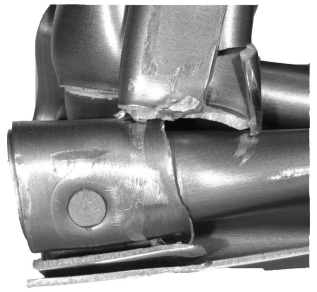

(b) Front.

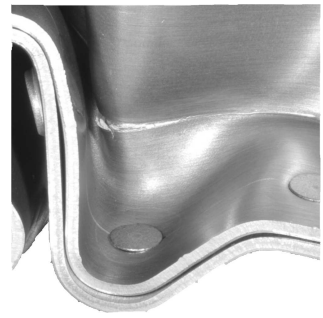

(c) Right side near clamping.

(d) Right side near the front.

(e) Left side near the front.

Figure 4.41: Failure in the sheets of CB1D-R.

(a) Left side and top of CB3D-R near the front.

(b) Right side of CB3D-R near the front.

(c) Left side of CB4D-R near the front.

(d) Right side of CB4D-R near the front.

(e) Left side of CB7D-R near the front.

Figure 4.42: Failure in the sheets of CB3D-R, CB4D-R and CB7D-R.

(a) Left side near the front.

(b) Right side near the front.

Figure 4.43: Failure in the sheets of CB5D-R.

4.5.2 Static reference

The deformed specimens are displayed in Figure 4.44, and display the same folding pattern. As seen, all folds for a specimen have approximately the same size.

The results from the static, riveted component tests are displayed in Figure 4.45 in terms of force and mean force histories. High repeatability is observed for the force level both in the initial peak force, ranging between 75 and 83 kN, and during the propagating buckling. The second peak is lower for CB1S-R than the two others, which is probably explained by a rift in the sheets, which is described later in this section. The mean force level is similar for all test, which indicate high repeatability with respect to energy absorption. The average mean force for 100 mm displacement was 35.14 kN.

Deformation and failure of rivets from static tests are described and categorized in a similar way as in Section 4.5.1.2. The deformation mode(s) for each specific rivet is found in Table C.2 and a summary of the observations is given in Table 4.4. None of the rivets failed completely. No deformation mode was observed for 14 % of the categorized rivets, while D1 was found for 86 % and D3 for 48 % of the rivets. As seen from the table, D1 was present for all occurrences of D3. More interestingly, no cases of D2 was observed.

The failures in the sheets found from the riveted crash boxes from static tests are displayed in Figure 4.46. Generally, cracks were observed at the same positions for all repetitions, but some differences were seen. As illustrated in Figure 4.46a, a rather large crack was observed for the first fold on the right side of CB1S-R. This is, however, believed to be caused by geometrical imperfections as the shape of the first fold on the top of the specimen (displayed in Figure 4.44c) deviated from CB2S-R and CB3S-R. Additional cracks were observed in the bends on each side of the specimen, seen in the lower left corner of Figure 4.46b. Expect for this, all cracks were found in zones in the folds where tension occurred, as illustrated in Figure 4.46c and 4.46d.

Table 4.4: Percent of rivets experiencing deformation and failure mode(s) from static tests.

Mode	All rivets
No mode	14
D1	86
D2	0
D3	48
D1+D2	0
D1+D3	48
D2+D3	0
F1	0

(a) Front.

(b) Left.

(c) Right.

(d) Top.

(e) Bottom.

Figure 4.44: Deformation modes from riveted, quasi-static tests.

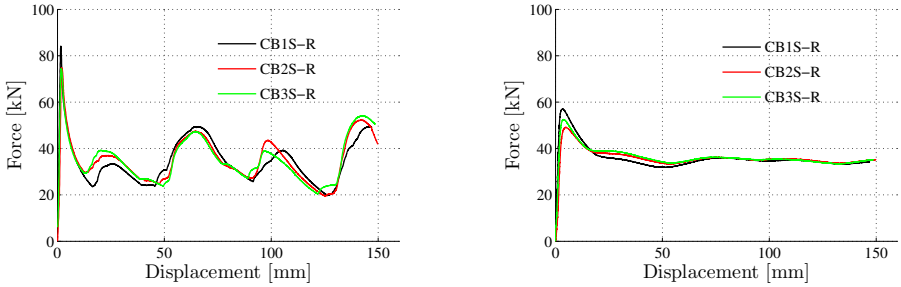

(a) Measured force.

(b) Mean force.

Figure 4.45: Measured and mean force plotted against displacement for the quasi-static riveted CB tests.

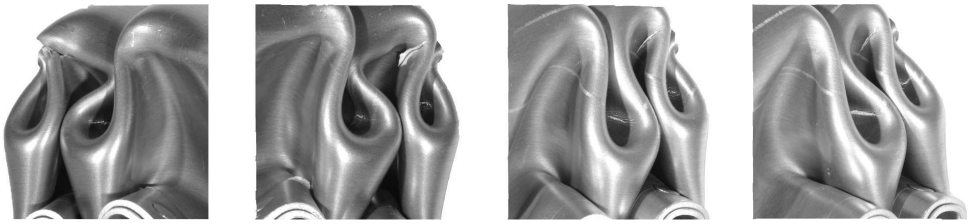

(a) Right side of CB1S-R near the front.

(b) Left side of CB1S-R near the front.

(c) Left side of CB2S-R near the front.

(d) Left side of CB3S-R near the front.

Figure 4.46: Failure in the sheets from riveted, quasi-static CB tests.

4.6 Screwed component test

The results from dynamic and static tests of screwed crash boxes are presented in this section. As for the riveted crash boxes, the emphasis is put on the dynamic tests and the static tests serve as references.

4.6.1 Dynamic

The deformed specimens are shown in Figure 4.47. Three dynamic component tests were performed for screwed crash boxes. The same deformation modes were seen for all specimens and none of the tests were discarded. As observed in Figure 4.47c, the size of each fold was generally increasing towards the clamped end. It is also noted that the clamping on the bottom side of the specimen was not stiff enough, as out-of-the-plane deformations are observed within the clamped area. Measurements from the test setup for each test is found in Table A.1.

As for the riveted component tests (see Section 4.5.1) three different displacement measures were conducted during the tests. By comparison it was concluded that all measures were valid, and the load cell measure is used henceforth. The mean force measurements were obtained from Equation (4.5) and (4.6).

4.6.1.1 Results

Figure 4.48 shows the force-displacement history of the three tests. The measured, filtered and mean force for all tests are plotted as function of displacement in Figure 4.48a, 4.48b and 4.48c, respectively. Excellent repeatability is observed. The initial peak forces are ranging from 92 to 97 kN for the filtered forces, and the post-buckling behaviours are similar up to approximately 105 mm displacement, both for the unfiltered and filtered signal. The scatter for the mean force is also insignificant, again indicating a high repeatability with respect to the energy absorption. The average mean force for 100 mm displacement was 38.77 kN. The measured, filtered and mean force is plotted together for test CB3D-S in Figure 4.48d.

4.6.1.2 Deformation and failure of screws

The description of deformation of crash boxes is related to Figure 4.33. Deformation and failure of the screws from the dynamic crash box tests were categorized according to Table 4.5 and as illustrated in Figure 4.49. The strength in the connection is considered small or negligible if one of the failure modes are observed. The screws are categorized in the same way as the rivets, including seven screws on each side of each specimen (see Figure 4.33). This leads to a total of 42 categorized screws for the dynamic CB specimens. The deformation and failure mode(s) for each specific screw is found in Table C.3 in the Appendix.

(a) Front.

(b) Left.

(c) Right.

(d) Top.

(e) Bottom.

Figure 4.47: Deformation modes from screwed, dynamic CB tests.

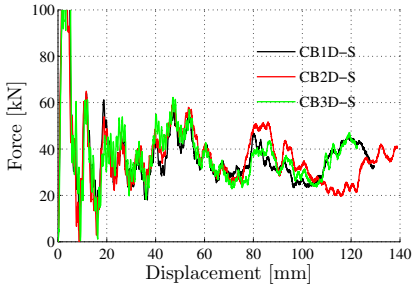

(a) Measured force for all tests.

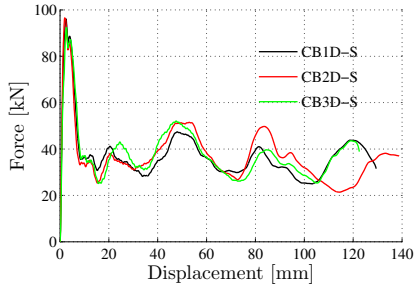

(b) Filtered force for all tests.

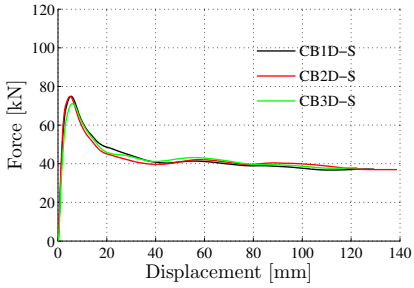

(c) Mean force for all tests.

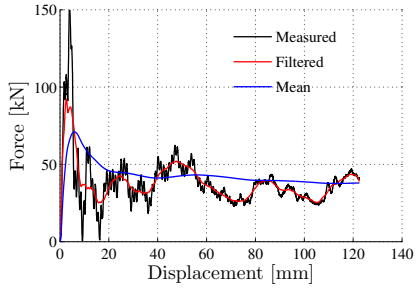

(d) Measured, filtered and mean force for CB3D-S.

Figure 4.48: Measured, filtered and mean force plotted against displacement for all screwed CB tests in (a), (b) and (c) and plotted together for CB3D-S in (d).

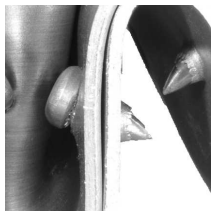

(a) D1.

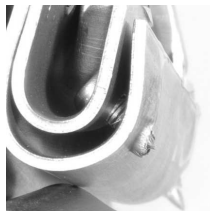

(b) F1.

(c) F2.

(d) F3.

Figure 4.49: Deformation and failure modes of screws.

(a) (b) (c)

Figure 4.50: Screw fracture captured by high-speed camera.

Table 4.5: Deformation and failure modes of rivets for screwed crash box specimens.

Name	Description
N	No visible deformation of failure mode
D1	Rotation of screw
F1	Pull-out from bottom sheet
F2	Push-out from bottom sheet
F3	Fracture in screw near the head
No head	Screw head missing from assembly

Deformation mode 1 (D1) is seen in Figure 4.49a and included rotation of the screw. As observed, the rotation of the screw was caused by relative displacement between the top and bottom sheet. This mode was typically observed for screws on the side of the folds.

Failure mode 1 (F1) is illustrated in Figure 4.49b and included pull-out of the screw from the bottom sheet. In most cases this failure mode was observed for highly rotated screws and may thus be considered as well developed cases of D1. However this was not always the case, as for the screw in Figure 4.49b.

For failure mode 2 (F2), the screw was pushed out from the bottom sheet by contact with an adjacent sheet or screw. This mode always involved a significant amount of rotation of the screw. An example of the mode is shown in Figure 4.49c.

A picture of failure mode 3 (F3) after deformation is shown in Figure 4.49d. F3 included fracture in the screw itself near the screw head, but not entirely adjacent. This mode was observed for two screws, and is believed to either be a result of over-torquing during the screwing process or induced by dynamic effects. Pictures of deformation mode 3 taken by the high-speed camera is shown in Figure 4.50. The top an bottom plates were never perfectly aligned in the front, such that the connections were subjected to shear loading during impact. The failure mode in the screw is possibly explained by high shear strain rates.

As seen in Table 4.6, the modes N, D1, F1, F2 and F3 were observed for 33 %, 55 %, 7 %, 7 % and 5 % of the screws, respectively. The two cases of F3 were both observed near the front of the specimens. No deformation or failure modes were observed for screws on row 4. These screws were located at the end of the second outward fold, where no relative movement of the sheets occurred. D1 was found for screws on the sides of a fold (row 2,

Table 4.6: Percent of screws within each screw row experiencing deformation and failure mode(s). One screw may have more than one mode. Row numbers refer to Figure 4.33.

Mode	% of all screws	% of screws in row						
		1	2	3	4	5	6	7
No mode	33	50	0	0	100	0	17	67
D1	55	17	83	83	0	83	83	33
F1	7	17	0	0	0	17	17	0
F2	7	0	0	17	0	33	0	0
F3	5	17	17	0	0	0	0	0
No head	2	0	0	17	0	0	0	0

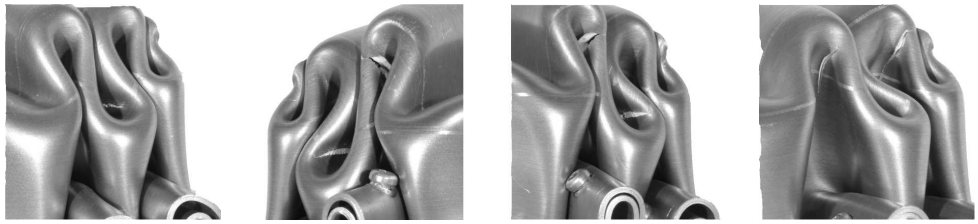

(a) Left side of CB1D-S near the front.

(b) Right side of CB2D-S near the front.

(c) Left side of CB2D-S near the front.

(d) Left side of CB3D-S near the front.

Figure 4.51: Failure in the sheets from screwed, dynamic CB tests.

3, 5 and 6). The screws on row 7 were generally little damaged. There is clearly a link between D1 and F1 and D1 an F2. The two failure modes were most frequently observed for highly rotated screws.

4.6.1.3 Failure in the sheets

Similar failures in the sheets were observed for all screwed crash boxes from dynamic tests, as illustrated in Figure 4.51. In all cases, the cracks were observed in the lobes at the corners of the specimens. These areas are tensile dominated zones. One to three cracks were observed on each side of the specimens. The cracks are not believed to affect the global response.

4.6.2 Static reference

The deformed specimens from static, screwed crash box tests are shown in Figure 4.52. As observed from Figure 4.52b, the folding pattern is the same between the specimens. Additionally it is observed that the sheets within the clamped area is deformed out of the plane. This is clearly visible in Figure 4.52e. The problem was resolved for test CB2S-S, where a plywood panel was exchanged with a steel plate.

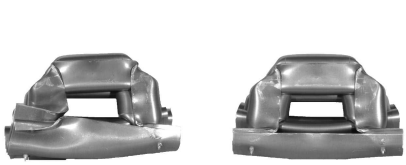

(a) Front.

(b) Left.

(c) Right.

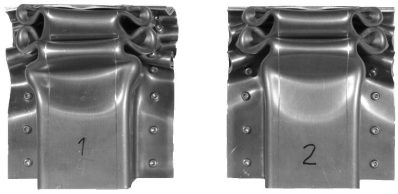

(d) Top.

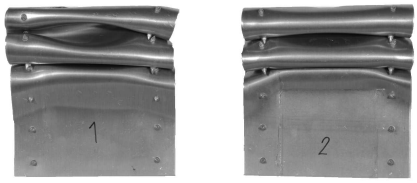

(e) Bottom.

Figure 4.52: Deformation modes from screwed, quasi-static CB tests.

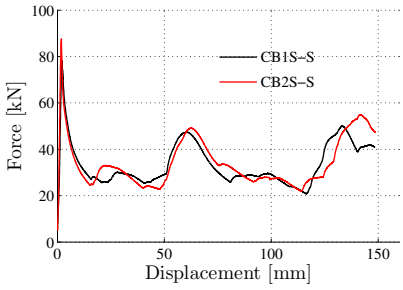

(a) Measured force.

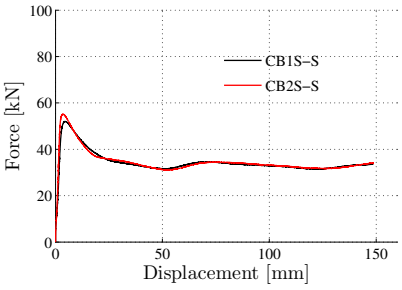

(b) Mean force.

Figure 4.53: Measured and mean force plotted against displacement for the quasi-static screwed CB tests.

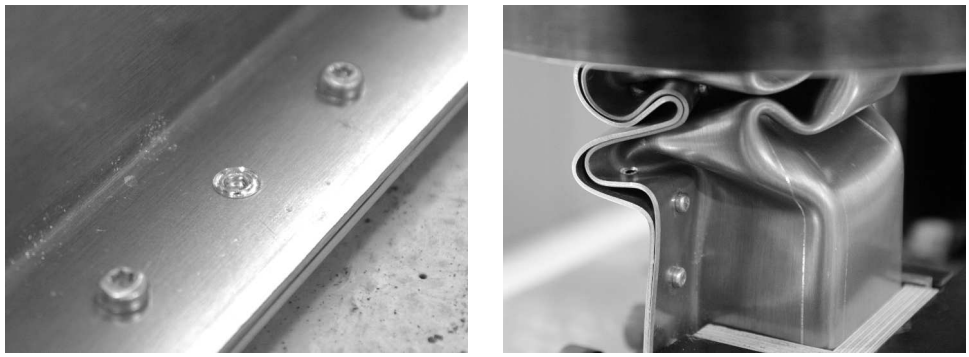

(a) Before deformation. (b) During deformation.

Figure 4.54: Screw head missing from assembly, CB1S-S.

Table 4.7: Percent of screws experiencing deformation and failure mode(s) from static tests.

Mode	All screws
No mode	43
D1	50
F1	4
F2	4
F3	0
No head	4

In Figure 4.53, the results from the static, screwed crash box tests are displayed. Again, high repeatability is observed for both the force and the mean force. The initial peak was 78 kN and 88 kN for the two tests. The average mean force for 100 mm displacement was 33.03 kN.

Deformation and failure of the screws from the quasi-static tests were categorized in the same way as the dynamic, and an explanation of the categories is found in Table 4.5. The deformation mode(s) for each specific screw is found in Table C.4 in the Appendix. A summary of the number of modes observed for the quasi-static tests is found in Table 4.7. Either no mode (43 %) or D1 (50 %) was found for the great majority of the screws. Additionally one screw was found from each of the categories pull-out, push-out and no head. The F3 mode (fracture in the screw itself) was not observed for the quasi-static tests.

The screw head missing in one crash box is displayed in Figure 4.54a. As shown in Figure 4.54b, this connection obviously influence the response of the crash box. Apparently, the sheets separate and the local deformations become slightly different in the vicinity of the screw. However, as observed in Figure 4.52c, the global response does not seem to be changed if this connection is missing. A general observation is illustrated in Figure 4.54b;

(a) Left side of CB1S-S near the front.

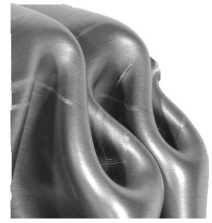

(b) Left side of CB2S-S near the front.

Figure 4.55: Failure in the sheets from screwed, quasi-static CB tests.

the sheets does not seem to be stiffened by the screw connection, as observed for the rivets. This may be due to the smaller diameter of the connection, as well as a smaller zone hardened by the inserting process for screws than for rivets.

For the static, screwed crash box tests, only minor cracks in the sheets were observed. As for other crash boxes, the cracks were found in tensile dominated zones inside the folds of the corners. This is shown in Figure 4.55. Additionally, whitened zones were observed inside the folds of some corners. It is believed that the these zones indicate incipient cracks.

4.7 Comparison of component tests

In this section, results and observations from the component tests are presented and discussed. Firstly, the dynamic component tests are compared to the static reference tests. Thereafter, the riveted tests are compared to the screwed, before the section is finalized by a comparison of the results from the static tests with an analytical formula for the mean force.

4.7.1 Dynamic and static

Comparisons of the results from dynamic and static tests of riveted and screwed crash box tests are shown in Figure 4.56 and 4.57, respectively. From the figures, it is evident that the local force peaks during progressive buckling in the dynamic tests are shifted towards lower displacements compared to the static tests. It is also seen that the force level generally is higher for the dynamic tests. Higher repeatability is seen in the force for static tests compared to dynamic. From Figure 4.56c it is noted that a force peak around 100 mm displacement was absent for the static screwed test compared to the dynamic.

By considering the mean force, it is observed that the difference between dynamic and static gradually decreases. For the riveted crash boxes, the average of the mean force for 100 mm displacement was 15 % higher for the dynamic than the static tests. The corresponding difference for the screwed crash boxes was 17 %. In general, an increased

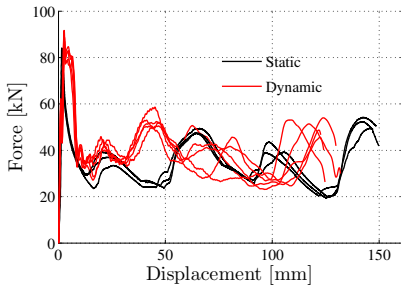

(a) Force.

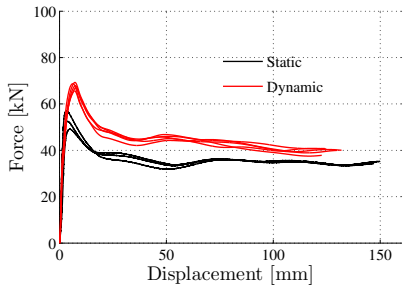

(b) Mean force.

Figure 4.56: Force and mean force from dynamic and quasi-static riveted CB tests.

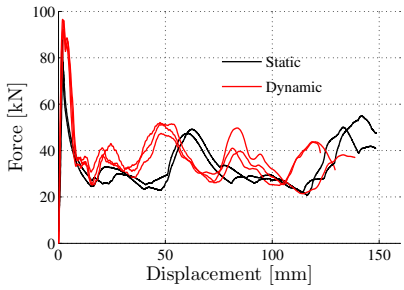

(c) Force.

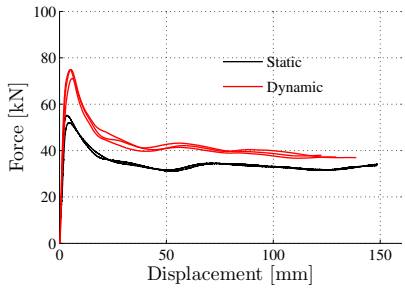

(d) Mean force.

Figure 4.57: Force and mean force from dynamic and quasi-static screwed CB tests.

force level in dynamic compared to static tests is either explained by strain rate effects, inertia effects or a combination of these. As Moore et al. [24] found that the strain rate sensitivity of AA6016-T4 is low, strain rate effects are assumed to be of minor importance. Inertia effects arises due to acceleration of mass in the axial direction of the specimen, as well as lateral acceleration of the walls of the top-hat section. It was also observed that inertia effects enforced different shapes of the specimens. This is discussed in the following.

In Figure 4.58 and 4.59, the buckling modes from dynamic tests are compared to static for riveted and screwed crash boxes, respectively. The red dots are the connections. It should be emphasized that the shown specimens were chosen to highlight a general trend observed for buckling modes, rather than being representative for all tests. Similar differences between dynamic and static tests are observed for both riveted and screwed crash boxes. Firstly, it is seen that the folds are most narrow near the front of the specimen, but with increasing fold size with increasing distance from the front. From the static tests, however, the fold size is nearly constant. This is also seen when inspecting the location of the connections with respect to the folds (see Figure 4.58 and 4.59). For instance, for the statically deformed specimens, the third connection is located at the end of the second

(a) Dynamic.

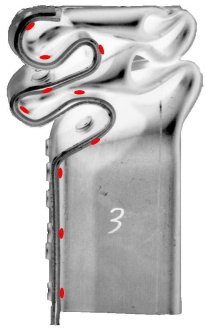

(b) Static.

Figure 4.58: Comparison of buckling modes from riveted CB tests.

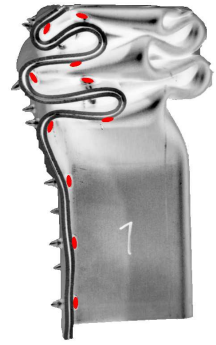

(a) Dynamic.

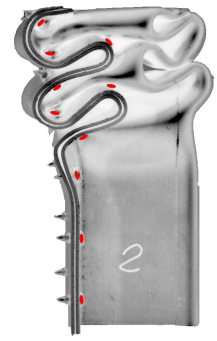

(b) Static.

Figure 4.59: Comparison of buckling modes from screwed CB tests.

fold. However, for the dynamically deformed specimens, the third connection is located between the second and third fold. Apparently, the dynamic crash boxes were forced into a shape which include larger deformations in the sheets near the front than the static. It is believed that the deformation during static tests followed the path of least resistance, which might explain why more energy was absorbed in the dynamic tests. Additionally, dynamic effects explain the shifting of the force curve towards lower displacements for the dynamic tests compared to the static.

Another observation well illustrated by Figure 4.59a is the undulated shape of the flanges within the clamped area. This was observed in some of the dynamic, but none of the static tests. By inspecting the recording from the high-speed camera, it is evident that this shape was enforced in the initial part of the impact. The phenomenon is believed to be local buckling of the flanges caused by propagation of stress waves.

In Table 4.8, the deformation and failure modes of the rivets and screws are compared between dynamic and static tests. Observations indicate that the damage of rivets is linked to the deformation shapes, presented in Figure 4.58. In the static tests little variation in damage modes was seen throughout the height of the specimens. In the dynamic tests, however, the connection damage was most severe near the front. For instance, the D2 mode (crack in bottom sheet near rivet) was in the dynamic tests observed for 20 % of the rivets, and only in the first four rows. This mode was, however, not seen in the static tests. Mode D1 and D3 occurred more often in the static than the dynamic tests, but was more evenly distributed along the height of the specimen in the static. These observations may indicate that the energy absorption was more evenly distributed along the height of the specimens in the static tests.

The screws were generally less damaged in static than dynamic tests. The F3 mode (fracture in screw near the head) was not observed in the static tests, which supports the assumption that this mode was induced by dynamic effects. It is believed that the two screws experiencing mode F3 were dynamically loaded in shear in the tests. In the screw assembly process, scatter in the torque may lead to over-tightening, which may reduce the capacity of the screw to sustain external loads. It is believed that the two F3 screws were

Table 4.8: Percent of rivets and screws experiencing deformation and failure modes in dynamic and static tests.

Rivets			Screws		
Mode	Dynamic	Static	Mode	Dynamic	Static
No mode	14	14	No mode	33	43
D1	73	86	D1	55	50
D2	20	0	F1	7	4
D3	33	48	F2	7	4
F1	7	0	F3	5	0
			No head	2	4

subjected to over-tightening, and that they therefore fractured during the tests. It should, however, be emphasized that possible imperfections in the screws may also contribute to such fractures. The D3 mode(rotation of screw) was observed for approximately the same number of screws in dynamic and static tests, which indicates that relative displacement between the sheets is not only a dynamic phenomenon.

The sheets experienced similar failure in the dynamic and static tests. Cracks were most frequently observed in tensile dominated zones at the rear side of the first folds from the front. Generally, slightly larger cracks were observed in the dynamic tests compared to the static. Additionally, the most severe sheet cracks were observed in dynamic tests. Slightly more damage was observed on the left than the right side of the specimens, which may indicate that the specimens were not perfectly centred.

4.7.2 Rivets and screws

A comparison of the results from riveted and screwed crash box tests is shown in Figure 4.60. The trend of force from dynamic tests (see Figure 4.60a) is very similar up to approximately 60 mm. The initial peak was slightly higher for screwed crash boxes, but shortly after the riveted exhibited the highest force throughout the test. Additionally, the force curves for rivets were slightly shifted towards lower displacements than for screws, which indicates a stiffer response.

According to Figure 4.60b, the force from static tests was similar for the screwed and riveted crash boxes. The force level was slightly higher for the riveted and one of the peaks (around 100 mm displacement) was absent for both screwed specimens.

In Figure 4.60c, the mean force from all tests are plotted together. Generally, the force level of the riveted crash boxes was higher than the screwed. As summarized in Table 4.9, the average mean force for 100 mm displacement was 4 % and 6 % higher for the riveted than the screwed crash boxes in dynamic and static tests, respectively. Slightly less scatter was observed in the mean force for the screwed than the riveted crash boxes.

In Figure 4.61 the buckling modes from dynamic tests are compared. Two riveted and two screwed specimens are included in the figure, in order to illustrate the scatter in deformation pattern. The global buckling modes were similar for riveted and screwed

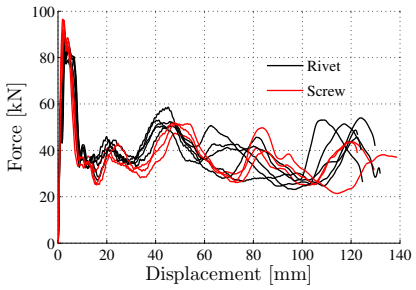

(a) Force, dynamic tests.

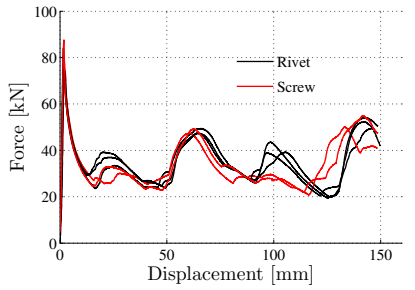

(b) Force, static tests.

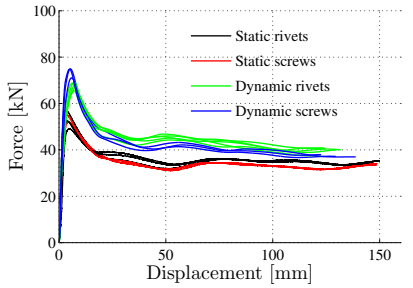

(c) Mean force, static and dynamic tests.

Figure 4.60: Measured and mean force for dynamic and static CB tests for rivets and screws.

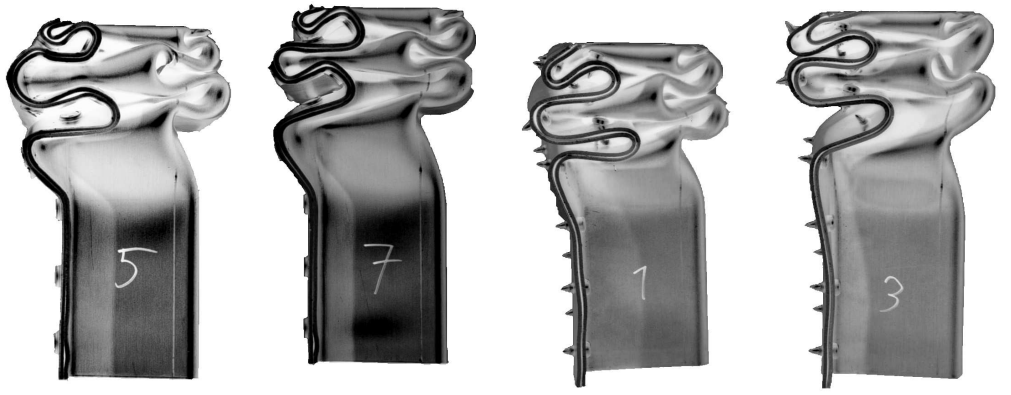

(a) Riveted. (b) Riveted. (c) Screwed. (d) Screwed.

Figure 4.61: Comparison of buckling modes from riveted and screwed dynamic CB tests.

Table 4.9: Comparison of average mean force for 100 mm displacement for crash box tests. The difference between the compared and the reference test is given in percent of the reference test.

	To compare			
Reference	Rivet, dynamic	Rivet, static	Screw, dynamic	Screw, static
Rivet, dynamic	-			
Rivet, static	15 %	-		
Screw, dynamic	4 %	-9 %	-	
Screw, static	22 %	6 %	17 %	-

crash boxes, but a more edged shape was observed in the folds for the riveted crash boxes. This is due to the stiffening of the sheets in the vicinity of the rivets. For the riveted crash boxes, each fold is represented by two smaller bends, while the corresponding deformation is formed by one large bend for the screwed. Possibly, larger plastic strains and thereby increased hardening are introduced for the smaller bends. If this is the case, this contributes to the increased force level seen for the riveted tests compared to the screwed.

In some cases the sheets were not perfectly aligned in the front and rear end of the crash box, such that a significant shear force occurred in adjacent connections upon impact. The rivet connections seemed to resist the shear force, while for the screwed specimens this led to some rotation of the adjacent screws and slight sheet separation. As previously discussed, significantly more sheet separation occurred in the screwed than the riveted crash boxes. Based on these observations, it is believed that the higher shear resistance of the rivets accounts for some of the increased energy absorption seen for riveted crash boxes.

In the dynamic tests, 14 % of the rivets and 33 % of the screws showed no deformation, while 7 % of the rivets and 19 % of the screws failed. This indicates that the deformation modes of the rivets were less severe than for screws. This may also be revealed by considering the observed relations between deformation and failure modes. For rivets, the failure mode F1 was linked to the less observed deformation mode D3. The most frequently observed failure modes for screws, F1 and F2, were clearly related to the often observed deformation mode D1.

As described in Section 4.4.2, the peeling resistance for rivets was relatively low compared to screws. From Figure 4.58a and 4.59a, it is observed that the connection on row four had the same position, inside a fold, for riveted and screwed crash boxes. This was the case for all specimens. The connections on this row were subjected to a peeling deformation. Interestingly, no deformation or failure modes were found for screws on this row, while all rivets failed there.

4.7.3 Comparison with analytical formula for static tests

An analytical expression for the static mean crushing force F_m^s for a spot welded top-hat section subjected to symmetric progressive buckling was developed and proposed by White et al. [34]. They assumed that the top-hat specimen was spot welded in a manner such that the structural integrity of the specimen was maintained during progressive buckling and the specimen was considered as a continuous structure. A perfectly plastic material was assumed, and the lobes were idealized as perfect plastic hinges. White et al. [34] predicted the static mean crushing force as

$$F_m^s = 8.22\hat{\sigma}_0 t^2 (L/t)^{1/3} \tag{4.7}$$

Here, $\hat{\sigma}_0$ is the yield stress of the perfectly plastic material, t is the thickness of the sheets and L is the perimeter of the top-hat section. The perimeter is given by $L = 2a+2b+4f$, where a and b are the width and height of the specimen, respectively, and f is the width of the flanges.

Since the sheet material in the tests was not perfectly plastic, the choice of $\hat{\sigma}_0$ was not obvious. As first choices, the initial yield stress σ_0 and the ultimate tensile stress σ_u observed in the UT tests in the 0 degree direction were tried. Additionally, the mean of these σ_m and an equivalent flow stress s_0 as proposed by Tarigopula et al. [33] were tried. The equivalent flow stress is given by

$$s_0 = \frac{\int_0^{e_u} s\,(e)\,\mathrm{d}e}{e_u} \tag{4.8}$$

where s and e are the engineering stress and strain, respectively. e_u is taken at the point of maximum engineering stress.

The results from the static tests are compared to the analytical solution of Equation (4.7) in Figure 4.62. As seen, the predicted mean force is highly dependent on the yield stress measure, and using σ_0 and σ_u gives too high and too low results, respectively. Using s_0 gives slightly better results, while σ_m renders best results.

The theoretical development is based on a top-hat specimen connected with spot welds. The influence of SPR or SPS connections is hence not accounted for. The assumption

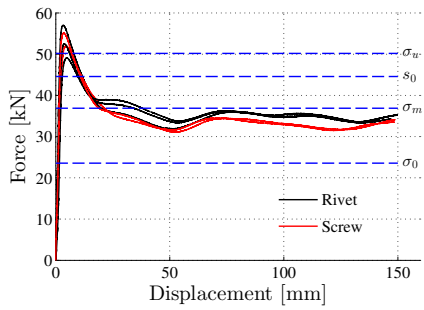

Figure 4.62: Comparison of mean force with analytical formula for static crushing.

that the specimen was a continuous structure is probably wrong for the SPR and SPS connections, as relative movement of the sheets was evident both for SPR and SPS. This was especially pronounced for the SPS specimens, which also experienced a few connection failures.

4.8 Concluding remarks

Material tests

- Uniaxial tension tests in seven directions, plane strain tests in two directions and shear tests were performed for material with and without heat treatment. In addition, pre-strained uniaxial tension tests with subsequent heat treatment were carried out for three levels of pre-straining.
- Generally, little scatter was observed in the material tests.
- The uniaxial tension tests indicated a minor anisotropy in flow stresses. No anisotropy was found for plane strain tensile yield stress.
- Heat treatment increased the maximum force and reduced the ductility. For uniaxial tension, the increase of maximum force by heat treatment was approximately 11 %.
- The effect of heat treatment was increased by pre-straining the specimens prior to heat treatment.

Single-connector tests

- Cross tests in three directions, single lap-joint tests with material oriented in two directions and peeling tests were performed for rivets and screws.
- By visual inspection, no plastic deformations were observed in the rivet or screw during testing.
- The pure shear cross test and the SLJ test were very similar, but a small tensile load component was introduced in the SLJ test in addition to the shear loading. In the pure shear cross tests, the sheets were prevented from separation due to the clamping.
- In the riveted SLJ tests, the material in the 90 degree direction showed decreased maximum force and significantly increased ductility compared to the 0 degree direction. This is possibly explained by higher hardening for the material in the 0 degree direction, introducing less tensile components in the connection.
- For the cross test, the maximum force and corresponding displacement was approximately 50 % higher for the riveted specimens than for the screwed. It should be emphasized that the diameter was 5 mm and 4 mm, respectively, and a higher strength was expected for the rivets compared to the screws.
- The rivet connection was stiffer than the screw connection. This is probably due to additional stiffness in the sheet caused by plastic deformations by the forming process, as well as the smaller diameter of the screw than the rivet. This influenced the deformation of the sheet around the connection.

- The fracture mode of the rivet connection for shear loading (the C-45, C-90 and SLJ tests) was more abrupt than for the screw connection. The rivet fractured suddenly from the top sheet while the screw failed gradually by pull out from the bottom sheet.
- In shear, relative movement between the sheets rotated the screw until the screw was pulled out by a shear fracture in the top sheet. Relative movement between the sheets was not seen for the rivets.
- Relatively speaking, the screw connection showed significantly higher resistance to peeling the rivet connection.
- Larger rivet head would increase resistance against failure mode observed in C-45 test, C-90 test and SLJ test, while probably decrease the peeling resistance.

Component tests

- Dynamic crash box tests were performed for rivets and screws, and corresponding quasi-static tests have been carried out as a reference.
- The same propagating buckling mode was observed for all tests.
- Generally, high repeatability was observed in both dynamic and static tests.
- For all crash boxes, minor tears were observed in the sheets in tensile zones on the rear side of the folds near the front.
- For the riveted crash boxes, three deformation modes and one failure mode was observed. The failure mode was related to peeling. From the dynamic tests, no failure or deformation mode was found for 14 % of the rivets while 7 % of the rivets failed. Except for peeling deformation, the rivet connections appeared to be stronger than the sheets.
- For the screwed crash boxes, one deformation mode and three failure modes were found. The deformation mode included rotation of the screw, and was observed for the half of the screws. Two of the failure modes, pull-out and push-out of the screw, were linked to this deformation mode. The third failure mode was believed to be a shear fracture in the screw, induced by a dynamic shear force. From the dynamic tests, no deformation or failure mode was observed for 33 % of the screws while 19 % failed.
- For the riveted crash boxes, the average of the mean force for 100 mm displacement was 15 % higher for the dynamic than the static test. The corresponding difference for the screwed crash boxes was 17 %. Strain rate effect was assumed to be of minor importance, and the increase of mean force is thereby explained by inertia forces.
- The crash boxes from were generally more damaged in dynamic tests compared to static, in particular near the front of the specimens. Additionally, the deformation of dynamically tested crash boxes included an increasing fold size with distance from the front, while the fold size was constant for the crash boxes from static tests. Explanation of higher damage in dynamic tests is two fold, higher total absorption of energy due to inertia forces and higher local deformations near the front.

- Deformation and failure of connections was more severe near the front in the dynamic tests (especially for rivets), while a more evenly distribution of deformation and failure was observed in the static tests. This is clearly linked to the previous bullet point.
- Generally, the measured force was higher for the riveted than screwed specimens. For 100 mm displacement the average of mean force was 4 % and 6 % higher for riveted than screwed specimens in dynamic and static tests, respectively.
- The same global buckling mode was found for riveted and screwed crash boxes, but the shape of the bends of the flanges was more edged for the riveted than the screwed specimens. This is believed to absorb more energy due to increased plastic deformations and subsequent hardening of the material.
- Relative movement between the sheets was observed for the screwed crash box specimens but not for the riveted. This is assumed to decrease the energy absorption of the screwed specimens compared to the riveted, due to reduced stiffness.
- Failure of the rivets is related to a less frequently observed deformation mode while failure of the screws is related to the most common deformation mode. Somehow, this make the behaviour of the screws more predictable.
- Slightly less sheet fracture was observed for the screwed specimens than the riveted, which possibly is related to a lower total energy absorption.
- The static mean forces from the experiments were compared to an analytical formula developed for hat sections of extruded material. Good agreement was seen when the mean of the initial yield and the ultimate tensile stress from the experiments was used as yield stress in the formula.

Chapter 5

Material model parameters

In this chapter, the constitutive relations governing the material response of the aluminium sheets are calibrated. Uniaxial tension tests are used to identify the material constants in the Barlat yield surface and Voce hardening rule. Subsequently, finite element models of the UT, PST and ISS tests are established. Results from the simulations are compared to experimental data to validate the calibrated model. The constitutive equations are calibrated for the material without heat treatment, the experimental data for heat treated material is left for later work.

5.1 Calibration

In this section, the Barlat yield function (see Section 2.4.2) and Voce hardening rule (see Section 2.4.4) are calibrated. The yield surface and the hardening rule are calibrated separately and together they form the constitutive model used for the chosen aluminium. This constitutive model was calibrated for the material without heat treatment.

The program MatPrePost developed by SIMLab at NTNU and SINTEF was used to perform the calibration. Representative force-displacement curves from UT tests in different directions were imported to the program together with measurements of the width and thickness of the respective specimens before and after the test. Information from the PST and ISS tests was not used for the calibration of the constitutive model. However, this information was used to validate the results.

MatPrePost calculates the flow stress ratios (r-ratios) from Equation (2.34) based on the force-displacement curves and from the UT tests and measurements of the initial geometries. In accordance with Equation (2.36), the strain ratios, R-ratios, are calculated based on the initial and final geometry of the specimens. As explained in Section 2.4.5, the r-values constrain the magnitude and the R-values constrain the gradient of the yield function. In the Barlat yield function, a possible strain dependency of the directional r- and R-values is neglected. r_α^{avg}, calculated using Equation (2.34), is used as r-value in the calibrations. The model predictions of the r- and R-values are continuous functions

Table 5.1: Different calibrations of the yield function.

Name	m	R_{EqB}
Calibration 1	6	0.86
Calibration 2	6	1.00
Calibration 3	8	0.86
Calibration 4	8	1.00

of the angle α and are denoted r_α and R_α, respectively. The equi-biaxial strain ratio R_{EqB} constrain the gradient of the yield function at the EqB point in the calibration. The equi-biaxial stress ratio r_{EqB} was not constrained in the calibration. MatPrePost optimizes the material parameters using a least square error algorithm.

Since the yield function is symmetric with respect to tension and compression, R_{EqB} may be found from through-thickness compression tests, assuming that the plastic deformation is independent of hydrostatic pressure. But no such test was included in the experimental program. Consequently a value of the parameter was chosen. A conservative choice would be $R_{EqB} = 1.00$, which is the value in von Mises' criterion. Based on recommendations the yield surface was calibrated for both the values 0.86 and 1.00. Vegter et al. [35] found $R_{EqB} = 0.889$ for an AA6016 alloy, which supports the choice of 0.86.

The value of the parameter m in the yield function, Equation (2.28), greatly affects the shape of the yield surface. This value must be specified prior to the optimization procedure. As stated in Section 2.4.2, $m = 8$ yields a good approximation for FCC metals, but additionally the value $m = 6$ was tested.

Accordingly, the yield function was calibrated with four different combinations of m and R_{EqB} (see Table 5.1). The same values of the hardening parameters were used for Calibration 1 through 4.

In addition to identifying model parameters, MatPrePost visualizes the results. In Figure 5.1 the experimental R-values are plotted as dots against the angle α. As before, α is the angle between the loading direction and the rolling direction of the sheets. Each experimental value represents an average value, as the values were exclusively based on information before and after the test. The variation of R-values over the plane of the sheet indicate some anisotropy in strain hardening. The continuous lines in the figure are the R_α-values predicted by the yield function for the different calibrations. As seen, the two yield surfaces calibrated with $m = 8$ predict identical R_α-values, while the values predicted with $m = 6$ are similar. All four calibrations are able to reproduce the experimental R-values.

In Figure 5.2 the r-values are plotted as function of plastic strain, and r_α^{avg} is displayed for each direction. The anisotropy of the flow stress is clearly visible. From the figure it is evident that the r-values evolve during plastic work, which is not in accordance with the assumption of isotropic hardening. In Figure 5.3, the predicted r_α-values for the calibrated yield surfaces are plotted against the angle α. The red dots are the r_α^{avg}-values from Figure 5.2. The two yield surfaces with exponent $m = 8$ give very similar results, and the yield surfaces with $m = 6$ deviate from each other. The surfaces with $m = 8$

predict r_α-values closer to experimental data than the surfaces with $m = 6$.

Figure 5.4 and 5.5 show the identified yield surfaces with intersections at constant shear stress σ_{xy} and in the σ_{xy} vs. $\frac{\sigma_x+\sigma_y}{\sqrt{2}}$ plane with intersections with planes with normal vectors along the line $\sigma_x + \sigma_y = 0$, respectively. Green dots in the figures represent r-values and the arrows indicate the R-values for the actual test direction. As expected, all four yield surfaces are very similar close to the points with experimental data. The yield surfaces with exponent $m = 6$ are more rounded than for $m = 8$. The greatest differences between the surfaces are found near the equi-biaxial point. Changing the R_{EqB}-values essentially tilt the surface normal in this point which enforces a different shape of the yield surface.

In Figure 5.6 and 5.7 the plane strain tension yield stress ratios, r_α^{pst}, and shear yield stress ratios, r_α^s, are plotted as functions of angle α. The curves represent unconstrained parts of the yield surfaces, as data from the PST and ISS was not included in the calibration. Again, m appears as a more important parameter than R_{EqB}. From the figures it is evident that the R_{EqB}-value has greater impact on the plane stress tension yield stress in y-direction than in x-direction. For the shear yield stress in zero degree direction, the calibrations with $m = 8$ give identical results while calibrations with $m = 6$ predict lower shear yield stress.

The hardening part was calibrated in MatPrePost using a ralg solver where the initial yield value and a cut off value was specified. The calibration was based on the representative experimental curve for UT test in the 0 degree direction. The same hardening parameters were applied to the four calibrations of the yield function.

Depending on the orientation of the material, Young's modulus was observed in the interval between approximately 65000 and 75000 MPa. A mean value of the Young's modulus was chosen equal to $E = 70000$ MPa and Poisson's ratio was set to $\nu = 0.35$ in all four calibrations. By this, the isotropic elasticity was defined.

The four calibrations have yield function parameters according to Table 5.2 and the seven Voce parameters are given in Table 5.3. The coefficients in the tables are according to Equation (2.29) and (2.32) in the Theory chapter.

5.2 Validation

Numerical analyses of the UT, PST and ISS tests were performed to validate the calibrated constitutive model. Based on the results from the numerical simulations one of the four calibrations from Table 5.2 is chosen to represent the material behaviour. The finite element code LS-DYNA was used to perform the analyses.

Explicit time integration was applied using constant stress solid elements. The SIMLab Metal Model was used to include the Barlat yield function in the numerical analyses. The SIMLab Metal Model is a part of a model library where customized user-defined material models are linked to finite element codes.

As the Barlat yield function is rate independent, time scaling was applied to reduce the computational time. The energy balance was monitored to ensure negligible inertia effects

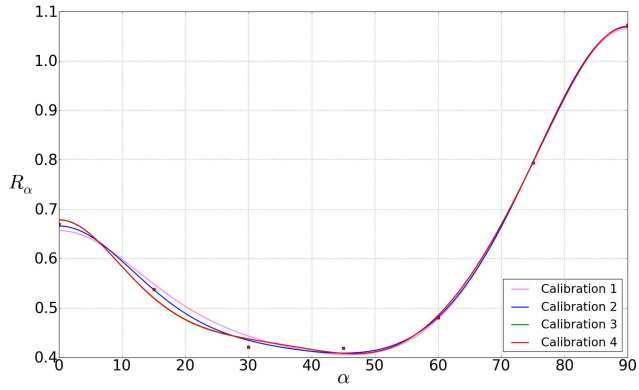

Figure 5.1: R-values as function of material orientation.

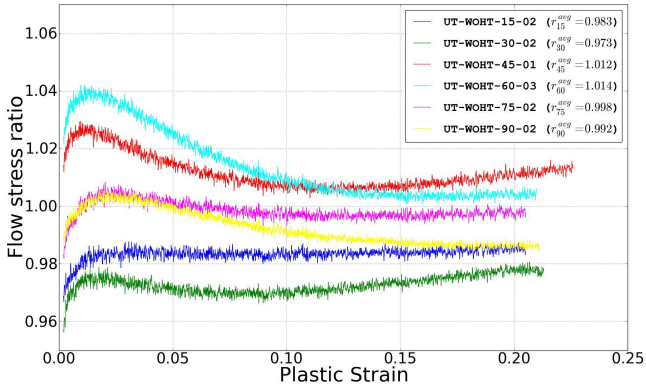

Figure 5.2: Uniaxial tension flow stress ratios as function of plastic strain.

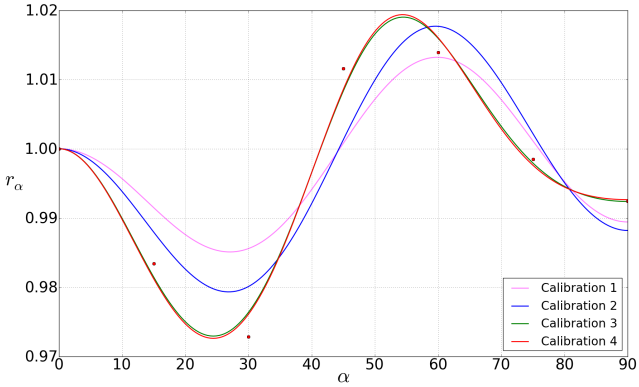

Figure 5.3: Uniaxial tension flow stress ratios as function of material orientation.

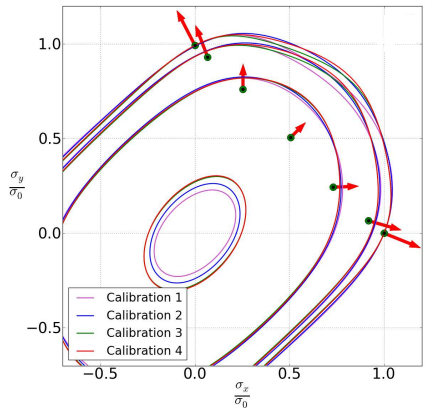

Figure 5.4: Yield surfaces for intersections at constant shear stress σ_{xy}.

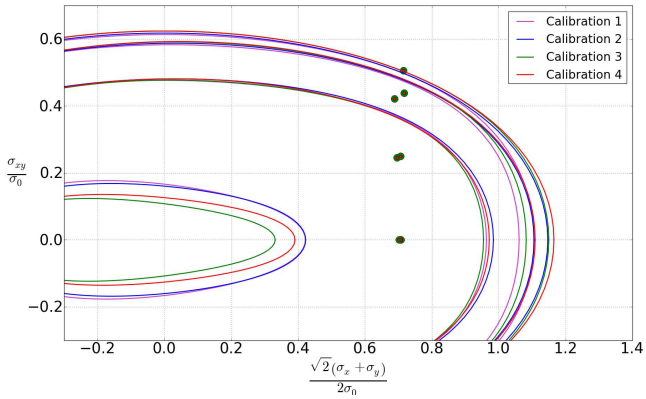

Figure 5.5: Yield surfaces for intersections of planes with normal vectors along the line $\sigma_x + \sigma_y = 0$.

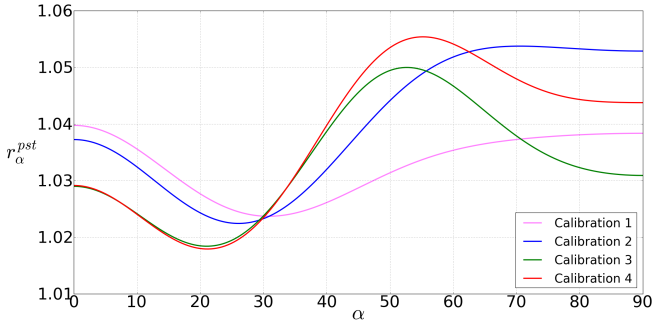

Figure 5.6: Plane strain tensile flow stress ratios as function of material orientation.

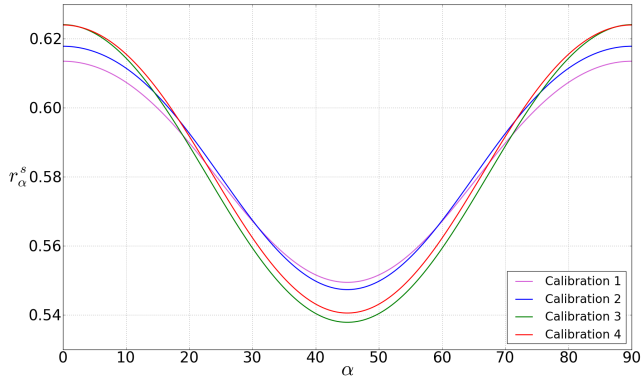

Figure 5.7: Shear flow stress ratios as function of material orientation.

Table 5.2: Parameters of calibrations of the yield function.

Calibration	1	2	3	4
m	6	6	8	8
c'_{12}	0.5378	0.5598	0.7956	0.7286
c'_{13}	-0.1755	-0.2378	-0.0314	0.0009
c'_{21}	0.2431	0.3232	0.1911	0.2277
c'_{23}	1.4632	1.4875	1.5011	1.4653
c'_{31}	-0.0559	0.0159	0.1253	0.2183
c'_{32}	0.8291	0.9536	1.0644	1.1202
c'_{44}	0.6860	0.7574	0.7035	0.6899
c'_{55}	1.0000	1.0000	1.0000	1.0000
c'_{66}	1.0000	1.0000	1.0000	1.0000
c''_{12}	1.4827	1.4085	1.0023	0.9938
c''_{13}	1.8574	1.8684	1.5979	1.6659
c''_{21}	1.2222	1.1883	1.1492	1.1866
c''_{23}	0.3547	0.2043	0.1206	0.1028
c''_{31}	0.8549	0.6145	0.3614	0.2803
c''_{32}	1.1069	0.9837	0.9037	0.8709
c''_{44}	1.1257	1.0465	1.0402	1.0537
c''_{55}	1.0000	1.0000	1.0000	1.0000
c''_{66}	1.0000	1.0000	1.0000	1.0000

Table 5.3: Parameters of the calibrated hardening rule.

Name	Value	Unit
σ_0	1.1966×10^2	MPa
Q_{R1}	1.6059×10^1	MPa
C_{R1}	1.6582×10^4	-
Q_{R2}	1.3456×10^2	MPa
C_{R2}	1.9346×10^3	-
Q_{R3}	3.4086×10^2	MPa
C_{R3}	2.6510×10^2	-

in the simulations. A stiffness based control of hourglass energy was applied in all the simulations of the material tests.

As the calibrations of the material model were purely based on results from the UT tests, excellent correspondence between the experiments and the numerical simulations was expected for these tests. However, the results from the numerical simulations of the PST and ISS tests indicate the quality of two parts of the yield surface not constrained during the calibration of the constitutive model. Accordingly, numerical simulations of the PST and ISS tests serve as validations of the calibration.

5.2.1 Simulation of UT test

The nominal geometry of the UT specimens is shown in Figure 3.1. As explained in Section 3.1.1, the specimens were simply supported with pins through the holes. The diameter of the pins was the same as the diameter of the holes. In the simulations of the UT tests the pins were modelled as rigid bodies (*MAT_020) and a one-sided contact formulation (*CONTACT_AUTOMATIC_NODES_TO_SURFACE_SMOOTH) was applied between the pins (master surfaces) and the holes (slave surfaces). The geometry was discretized using 8910 elements. In the primary deformation area the element size was 0.5 mm $\times$ 0.5 mm $\times$ 0.4 mm in the longitudinal, transverse and thickness direction, respectively. This corresponds to five elements through the thickness. The user-defined material was oriented in the longitudinal direction of the specimen. The model is shown in Figure 5.8. One pin was fixed and a prescribed velocity was applied to the other pin.

The resultant force in the longitudinal direction of the specimen was obtained by summing the element forces over a cross-sectional plane in the primary deformation area with normal vector perpendicular to the specimen. To obtain the displacement, the distance between two nodes in the primary deformation area was measured. The two nodes corresponded to the placement of the knives of the extensometer. The engineering stress and strain were subsequently computed according to Equation (4.1) and (4.2).

The mesh appeared to be too coarse to capture necking correctly, but this was ignored as post-necking behaviour is not a concern in this work. To improve the results after necking, a finer mesh should be applied, as well as an iterative procedure for Voce hardening parameters.

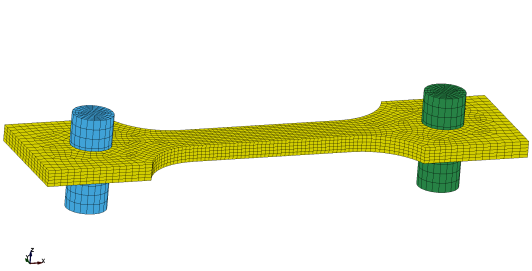

Figure 5.8: Finite element model of the UT tests.

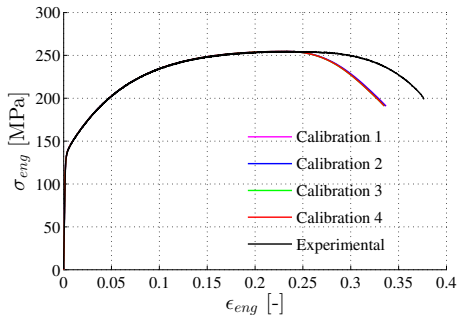

Figure 5.9: Engineering stress-engineering strain curves from the simulations and the representative experimental test.

Figure 5.9 shows the engineering stress-engineering strain curves from the simulations using Calibration 1 through 4. The results of all simulations of the UT test match perfectly with experimental data up to necking. This was expected since the material model was calibrated from the results of the UT tests.

5.2.2 Simulation of PST test

The PST test was modelled with nominal geometry (see Figure 3.3) and the model is shown in Figure 5.10. In the simulations of the PST tests the geometry was discretized using 8384 elements. The approximate element size in the primary deformation area was 0.6 mm $\times$ 0.5 mm $\times$ 0.5 mm in the longitudinal, transverse and thickness direction, respectively. In the thickness direction 4 elements were used. The user-defined material was assigned to the model and simulations were performed for both the material orientated in the longitudinal (0 degree direction) and the transverse direction of the specimen (90 degree direction).

The clamping was modelled by fixing the nodes at the left end and applying a velocity constrained to the longitudinal direction of the to the nodes at the right end.

The clamped parts of the specimen were assumed to stay undeformed during the test. This being the case, the specimen was intentionally modelled 17.5 mm shorter in each end to represent the pneumatic clamping.

The force in the longitudinal direction of the specimen was computed by summing the element forces over a cross-sectional plane perpendicular to the primary deformation area. To obtain comparable displacements with the experiments, the longitudinal distance between two nodes was measured throughout the simulation. The two nodes were picked such that the initial distance matched the gauge length of the extensometer (25 mm).

The force-displacement curves from the simulations are shown in Figure 5.11. As seen, the results match well. From approximately 0.75 mm displacement, the simulation over-predicts the force until the maximum force is reached. Calibration 3 provides the lowest

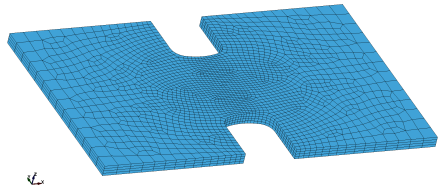

Figure 5.10: Finite element model of the PST tests.

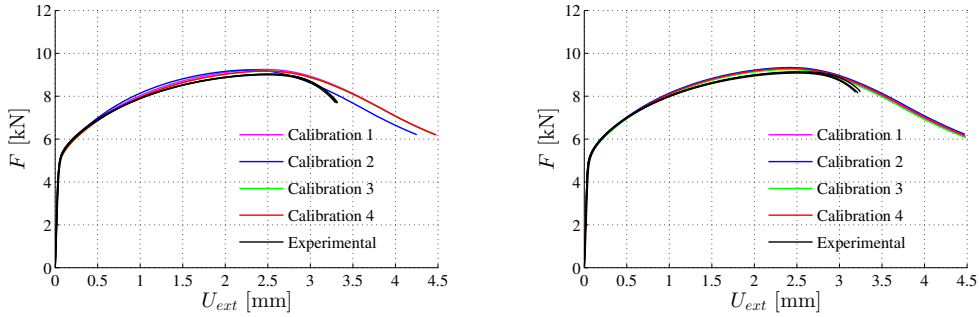

(a) 0 degree direction.

(b) 90 degree direction.

Figure 5.11: Force-displacement curves from the simulations compared with the experimental results for the 0 degree and the 90 degree directions.

force level in both the 0 degree and the 90 degree simulations. For this simulation, the maximum force over-estimated by approximately 1.6 % and 1.8 %, respectively in the 0 degree and the 90 degree directions.

Calibration 1 produced the highest force level in the 0 degree direction, while Calibration 3 produced the lowest. For the 90 degree direction Calibration 2 produced the highest, while Calibration 3 produced the lowest force level. By considering the plane stress tensile yield stress from Figure 5.6, it is evident that the results corresponded with the expectations.

All yield surfaces are able to satisfactorily reproduce the experimental results from the PST tests. Nevertheless, Calibration 3 provides the best results.

5.2.3 Simulation of ISS test

The nominal geometry of the ISS specimen is shown in Figure 3.5. The numerical model of the ISS specimen is shown in Figure 5.12 and 5.13. When the ISS specimen is stretched, the geometrical shape enforces the deformations to primarily occur in the central part. Hence, the red and green parts were modelled as rigid bodies (*MAT_020). To enable use of a finer mesh in the central part, the blue and yellow parts were tied together by use of a node-to-surface contact formulation (*CONTACT_TIED_NODES_TO_SURFACE). The user-defined material was assigned to the blue and yellow parts. Simulations were

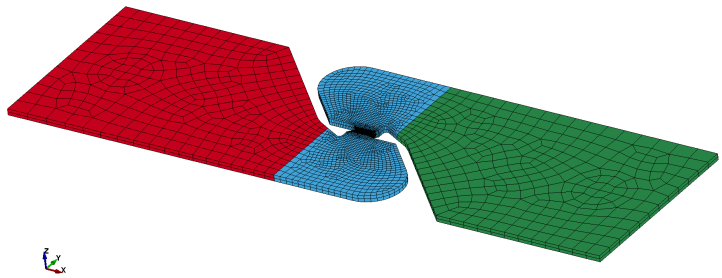

Figure 5.12: Finite element model of the ISS tests.

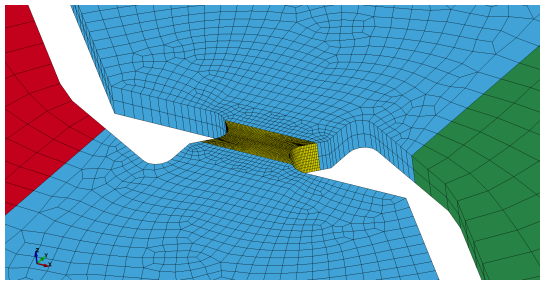

Figure 5.13: Central part of finite element model of the ISS tests.

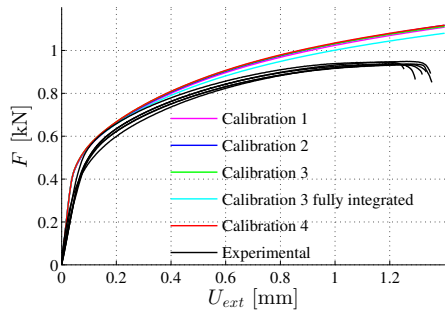

Figure 5.14: Force-displacement curves from the simulations in 0 degree direction compared with the experimental results.

performed with the material oriented in the 0 degree direction and in the 90 degree direction.

A symmetry condition was applied such that half the thickness was modelled. The complete model was discretized using 30980 elements where 26400 form the yellow part. The approximate element size for the smallest elements was 0.03 mm $\times$ 0.02 mm $\times$ 0.1 mm in the longitudinal, transverse and thickness direction, respectively.

In the experiments, the specimens were attached to the test machine with pins through holes at each end. Each end was clamped in the numerical model. The load was applied as prescribed motion in the longitudinal direction of the specimen at each end. The resultant force in the longitudinal direction was computed by summing the element forces over a cross sectional plane.

Ideally, the displacements should be extracted from the same positions in the simulation as the placement of the knives of the extensometer during the experiments. Due to the rigid body definitions, the displacements extracted from the simulation corresponded to the displacements of the rigid bodies. By comparing the experimental test setup in Figure 3.6 and the numerical model in Figure 5.12, it is evident that an error is introduced as the displacements were extracted from different positions. Displacements were extracted 20 mm from the midpoint in the experiments (40 mm gauge length on the extensometer) and 5 mm from the midpoint in the numerical simulations (end of blue part). This source of error was discovered when investigating the results.

A comparison between the force-displacement curves from the experiments and the simulations is shown in Figure 5.14. All four calibrations give similar results. This is expected, as the yield surfaces are similar for a pure shear stress state (see Figure 5.5). Generally, the results of the simulations of the ISS tests are considered satisfactory.

The response is too stiff in the elastic part and the force is increasingly over-estimated throughout the test. The force is over-predicted by approximately 15 % at the point where the experimental tests fractured. The stiff response in the elastic part may be due to the error introduced when extracting the displacements. The model should have been simulated with deformable material within the placement of the knives of the extensometer. The effect of this on the extracted displacements is assumed to be small, but is not further investigated. Modelling the specimen as clamped instead of with pins through holes might also have stiffened the response. Another possible explanation for the stiff response is the mesh size, as the mesh in the blue part in Figure 5.13 is rather coarse. The jump in mesh size at the tied contact might also have added some stiffness to the model. The over-estimated force level after yield may be due to the isotropic hardening rule, which was calibrated in tension. Additionally, the shear test could be used to identify the hardening parameters by an inverse method.

The magnitude of the hourglass energy in the analyses was approximately 5 % of the internal energy. To investigate this effect an analysis with fully integrated elements was performed. As seen in Figure 5.14 the results are significantly better for the fully integrated elements. However, the original results are still considered reliable.

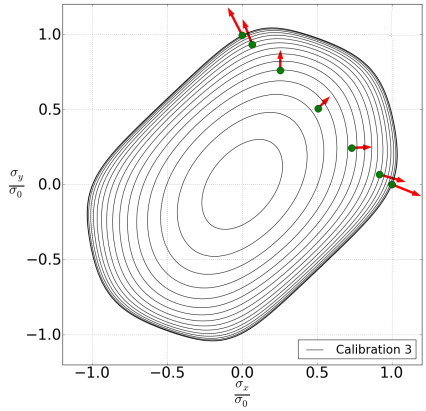

Figure 5.15: Yield surface for intersections at constant shear stress σ_{xy}.

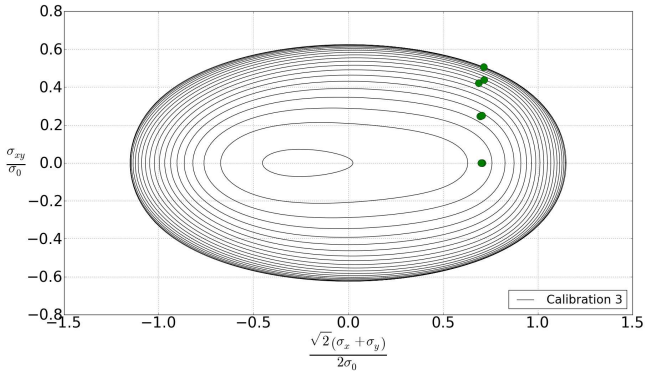

Figure 5.16: Yield surface for intersections of planes with normal vectors along the line $\sigma_x + \sigma_y = 0$.

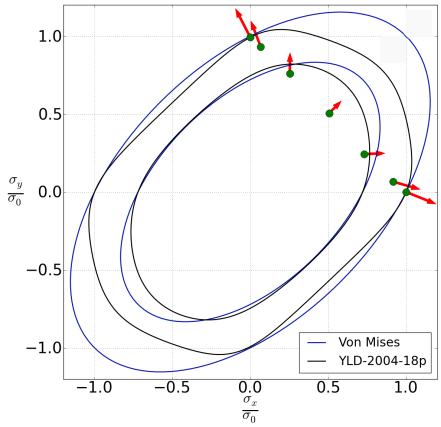

Figure 5.17: Chosen yield surface compared to von Mises'.

5.2.4 Conclusions from validation

Based on the results from the simulations of the UT, PST and ISS tests, all calibrations seem to give acceptable results. This might be explained by the high flexibility of the Barlat yield function. In the simulation of the UT test, all calibrations gave identical results. For the PST simulations Calibration 3 and 4 ($m = 8$) gave better results than 1 and 2 ($m = 6$). By taking the PST simulation with the material oriented in the 90 degree direction into consideration, Calibration 3 gave the best results. For the ISS results, the results from the simulations were similar. As a conclusion Calibration 3 ($m = 8$ and $R_{EqB} = 0.86$) gave best correlation with experiments and was chosen to represent the material behaviour.

The yield surface of Calibration 3 is presented in Figure 5.15 and 5.16, again with the experimental results indicated with green dots and red arrows. Calibration 3 is plotted together with von Mises' isotropic yield function in Figure 5.17. Largest differences in flow stress are observed near the equi-biaxial point. For von Mises' yield function $r_{EqB} = 1$, while for Calibration 3 r_{EqB} is less than 1. The minor material anisotropy is reflected in the slight rotation of the symmetry axis of Calibration 3 compared to von Mises'.

5.3 Concluding remarks

- The Barlat yield function was calibrated from UT tests in seven directions for four combinations of the exponent m and the R_{EqB}-value using the material without heat treatment. Experimental data for the material with heat treatment is left for later work.
- The Voce hardening rule was calibrated from initial yield to necking from the representative UT test with material oriented in the rolling direction.
- A minor anisotropy was found in flow stress.
- Anisotropy in strain hardening was observed.
- The four calibrated yield surfaces were validated by performing finite element simulations of UT, PST and ISS tests. Generally, the results corresponded well with experimental data. The surface with $m = 8$ and the $R_{EqB} = 0.86$ predicted best results and was chosen to represent the material.

Chapter 6

Forming process simulations

As part of the production of the P and CB specimens, 90 degree bends were introduced in the sheets. The bending process induces residual plastic strains which may affect the local as well as the global response of P and CB specimens. To investigate this, finite element models of the forming process were established and simulations were performed. Subsequently, the final equivalent plastic strain field and the hardening values in the bend from a forming process simulation were mapped to corresponding bends in established finite element models of the P and CB specimens. Finally, the effect of forming history in the P and CB simulations was investigated (Chapter 7 and 8).

Bending of the plates was performed by using a punch to pressing the plate into a die. LS-DYNA was used to simulate the process. Two different models were generated, one using 2D plane strain elements (element formulation 13) and one 3D plane stress simulation using Belytschko-Tsay shell elements (element formulation 2). Details of the element formulations are found in the LS-DYNA Theory Manual [36]. The update of the P and CB simulations is based on the 3D plane stress analysis. The 2D analysis was intended to give detailed information of the through-thickness and along-width plastic strain field, and serve as a validation of the 3D analysis.

It was not possible to include the Barlat yield function for the 2D plane strain elements. Therefore, the 2D analysis was modelled with von Mises' yield criterion combined with the same hardening parameters as before. An alternative strategy to include the Barlat yield function, would be to model the problem in 3D and constrain displacements in one direction. Even if the anisotropy of the material could have an impact on the bending simulation, this is not regarded in this study.

Explicit time integration was applied, and the SIMLab Metal Model library was utilized to include both material models. Since the material models are rate independent, time scaling was applied to reduce the computational time. The energy balance was monitored to ensure negligible inertia effects in the simulations.

The inner and outer radius of the bend in the specimens were 3 and 5 mm, respectively. To obtain the same shape in the simulations, the radius of the punch and die were set to 3 and 5 mm. In both models the die was constrained, while a prescribed motion was

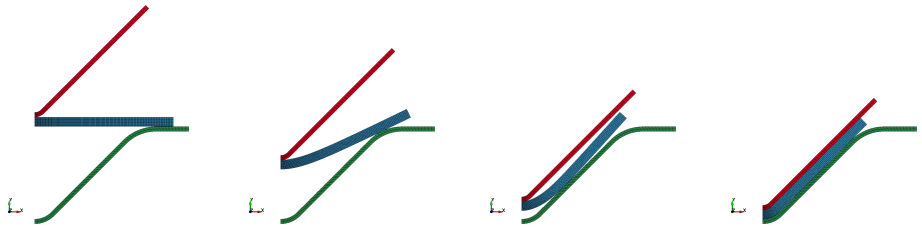

(a) Before. (b) Halfway. (c) Nearly there. (d) After.

Figure 6.1: 2D plane strain model at different stages of the forming process.

assigned to the punch. The length of the plates in the 3D model was 300 mm, which equals the length of the crash box specimens. The width was chosen as 60 mm for both the 2D and the 3D model, which corresponds to the bent parts of the peeling and crash box specimens.

Forming process simulations usually involve friction between the sheet and the punch/die. As the friction coefficient was unknown, a parametric study was done to assess its effect. For both the 2D and 3D simulation, the following values were tested: 0.2, 0.3, 0.4 and 0.5. Details from the simulations are presented for friction coefficient 0.2.

6.1 2D plane strain simulation

To simulate the forming process under the plane strain condition, a 2D plane strain shell model was established. The kinematics of the simulation are detailed in Figure 6.1. The numerical model consisted of three parts. The punch (red part) and the die (green part) were modelled as rigid bodies, while von Mises' yield function with hardening was applied to the plate (blue part). A 2D node to surface contact formulation was applied between the plate and the tools. In both cases, the plate was defined as slave. Initially, all parts were separated in space by a small gap, to avoid any initial contact of the contact algorithm. A symmetry condition was applied to halve the number of elements.

The geometry was discretized with a total number of 2102 elements, where 1800 elements formed the plate. The approximate element size close to the symmetry line was 0.13 mm $\times$ 0.13 mm and 0.13 mm $\times$ 0.37 mm near the plate end. This mesh is denoted the standard mesh. One additional model was built with a refined mesh for the plate part, keeping the mesh for the punch and die unchanged. In this case the plate was modelled with 3150 elements which corresponds to an approximate mesh size of 0.10 mm $\times$ 0.10 mm close to the symmetry line and 0.10 mm $\times$ 0.30 mm near the plate end.

In Figure 6.2a and 6.2b the equivalent plastic strain ϵ^p_{eq} for different values of the friction coefficient is plotted for the top and bottom element rows, respectively. The abscissa axis refer to the initial position of the elements in the plate plane. Generally, the forming process appears to be little influenced by the friction coefficient. Peak values of plastic strains are observed in the contact zone between the punch/plate and the plate/die.

The equivalent plastic strain at the top and bottom of the plate are plotted in Figure

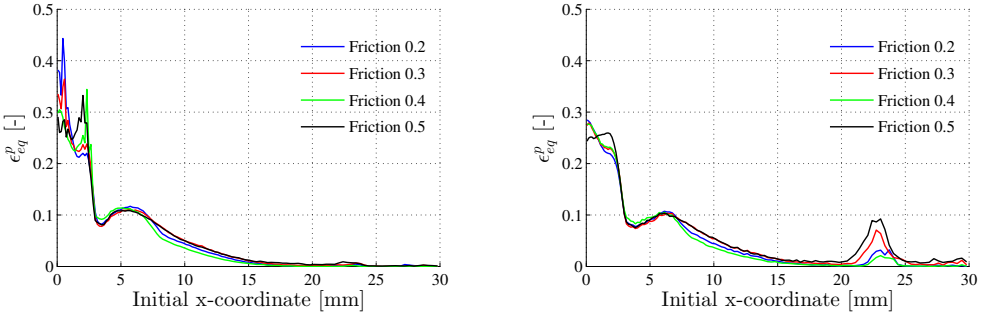

(a) Top element row.

(b) Bottom element row.

Figure 6.2: Equivalent plastic strain for different friction coefficients in the 2D plane strain model with the standard mesh.

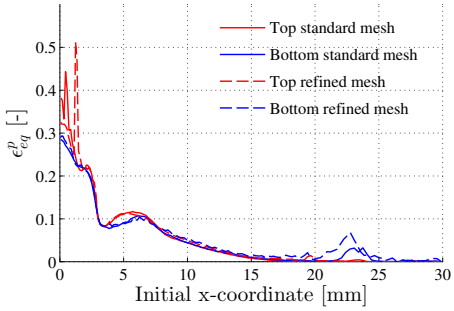

Figure 6.3: Equivalent plastic strain for different meshes in the 2D plane strain model. Friction coefficient is 0.2.

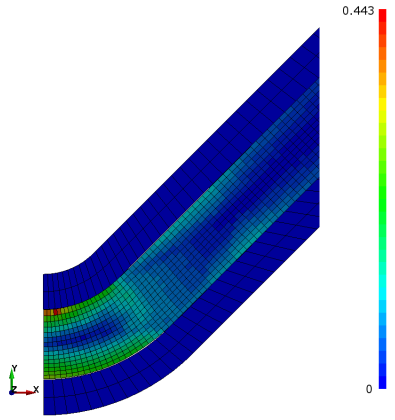

(a) Equivalent plastic strain field.

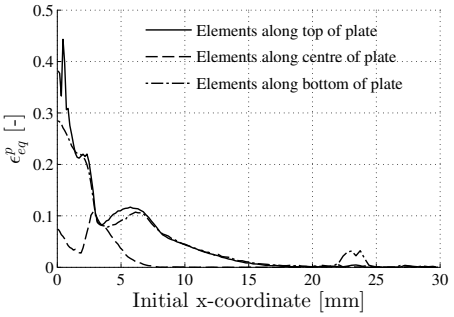

(b) ϵ^p_{eq} along the width.

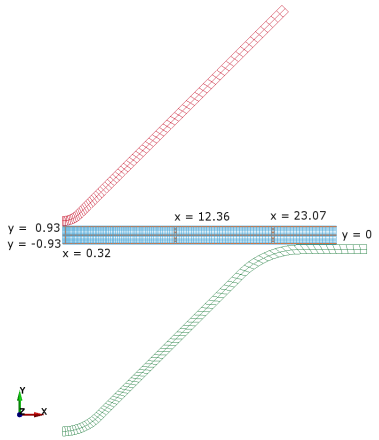

(c) Selected element rows and columns. The coordinates refer to element centre.

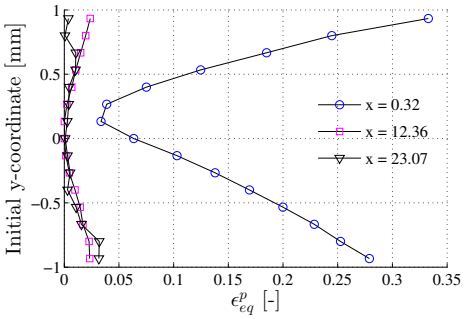

(d) ϵ^p_{eq} through the thickness.

Figure 6.4: Equivalent plastic strain for friction coefficient 0.2 in the 2D plane strain model with the standard mesh.

6.3 for the standard and refined mesh. The general trend is similar for the two meshes, but the magnitude and position of the maximum values seem to be mesh dependent. By investigating the results closely it became clear that penetration occurred between the punch/plate and the die/plate in areas with high curvature. This produced non-physical peak values of equivalent plastic strain in single elements. Hence, the peak values observed in the contact zones with high curvature are believed to be a numerical effect produced by the contact algorithm. The problem may be reduced by refining the mesh on the punch and die to better represent a smooth curvature of the rigid bodies.

In Figure 6.4a the equivalent plastic strain field after forming is shown, and in Figure 6.4b the equivalent plastic strains for elements on the top, the centre and the bottom of the plate are represented. To investigate the through-thickness equivalent plastic strain, the results are illustrated for three sections. As shown in to Figure 6.4c, the first section is between the curved part of the punch and die, the second is between two flat parts and the third section is between the flat part of the punch and the curved part of the die. The through-thickness equivalent plastic strain fields at these positions are shown in Figure 6.4d.

As seen in Figure 6.4b some plastic strains are evident along the centre of the plate, up to 17 mm from the symmetry line. From 10 mm to 30 mm the equivalent plastic strain equal zero for the mid element row. A peak is observed in the region approximately 3-8 mm from the symmetry line, and may be explained by taking a closer look on the deformation history. The first part of the metal forming is a three-point bending process where the contact point between the plate and die gradually moves towards the symmetry line, as displayed in Figure 6.1b. This continues until the punch hits the end of the plate, which is about to happen in Figure 6.1c. From this point to the end the simulation becomes similar to a five-point bending process which introduces alternated moments and corresponding plastic strains. This explains the peak mentioned above. As shown in Figure 6.3, this peak appeared to be little influenced by the mesh size of the plate. The height and position of the peak, however, is highly affected by the width of the plate. The width of the plate determines the lever arm in the five-point bending process. Changing the lever arm will change the alternated moments and correspondingly the distribution of plastic strains. This particular phenomenon is not further investigated in this work.

According to Figure 6.4d it is observed that the equivalent plastic strain is higher in the upper half of the plate than the lower, such that the neutral axis is situated above the centre line. This is explained by the lower radii of curvature of the punch than the die, which enforce larger deformations under the punch than over the die.

6.2 3D plane stress simulation

A 3D shell model of the forming process was established and is shown in Figure 6.5. The punch (blue part) and the die (green part) were defined as rigid bodies (*MAT_020). The Barlat yield function with the hardening rule was assigned to the plate (red part), and oriented in the longitudinal direction of the plate. A one-sided contact formulation (*CONTACT_AUTOMATIC_NODES_TO_SURFACE) was applied between the punch and die (masters) and the plate (slave). The symmetry of the process was utilized, and two sym-

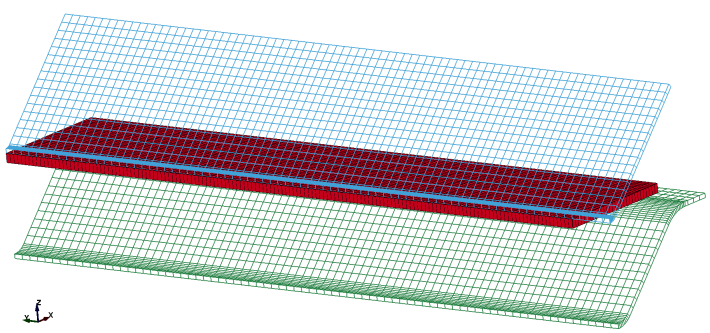

Figure 6.5: 3D shell model of forming process. The thickness is included for visualization.

metry planes were defined through the middle of the plate in both the transverse and longitudinal direction. In Figure 6.5 only the modelled quarter is shown. The complete model consisted of 9300 elements whereof 4500 constituted the plate. The element size of the plate was 1.0 mm $\times$ 1.0 mm. In order to check for mesh dependency a simulation with element size of 0.5 mm $\times$ 0.5 mm in the plate was performed, but no significant difference was observed. For the deformable elements the through-thickness element integration was performed using Gauss integration with five integration points. The equivalent plastic strains were obtained for the same locations as the integration points.

In Figure 6.6 the equivalent plastic strain along the element row in the middle of the plate (left on Figure 6.5) is plotted against initial position of the elements in the transverse direction. As for the 2D plane strain model, the value of the friction coefficient is insignificant on the level of plastic strains.

Figure 6.7 shows the equivalent plastic strain field in the uppermost integration point at the end of the simulation. Except for a slightly evident end effect the equivalent strain field is independent of location in the longitudinal direction of the plate. This supports the assumption of plane strain. In Figure 6.8 further details are displayed, as the equivalent plastic strain is plotted along three element rows in the transverse direction of the plate. Left and right end refers to Figure 6.5 and corresponds to the mid and the end of the plate, respectively. The remaining row is in the middle of the model. As expected, the equivalent plastic strains at the left end and the middle of the model are almost identical. Some end effects are, however, observed at the element row at the right. The level of equivalent plastic strain is lower for this element row.

Figure 6.9 shows the equivalent plastic strain plotted along the element row on the left of the model (corresponds to the middle of the plate) for different integration points. The coordinate z refers to the position of the integration point in the thickness direction of the plate. As the forming process mainly consist of near pure bending, the equivalent plastic strain was expected to be zero in the middle of the plate and gradually increasing towards the surfaces. As seen, this is the case.

The same deformation history of the plate was observed for the 3D model as for the 2D model. The details of this are described in Section 6.1.

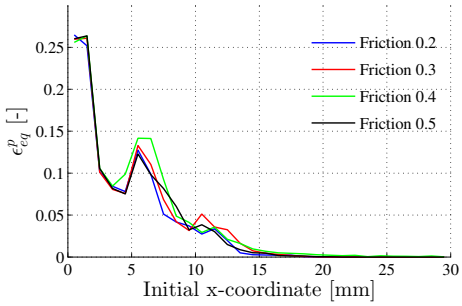

Figure 6.6: Equivalent plastic strain for different friction coefficients.

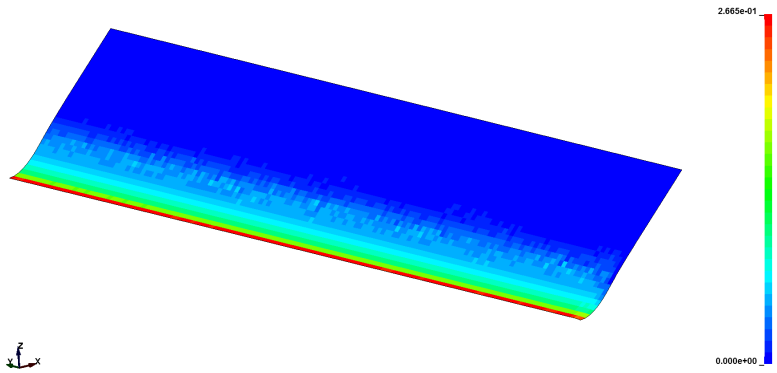

Figure 6.7: The equivalent plastic strain field for friction coefficient 0.2.

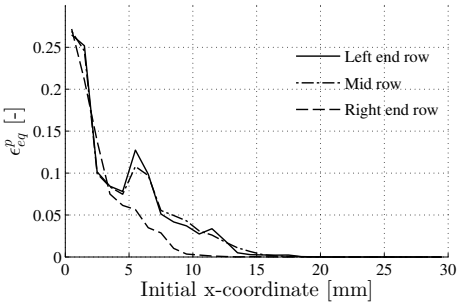

Figure 6.8: Equivalent plastic strain along three element rows. Friction coefficient is 0.2.

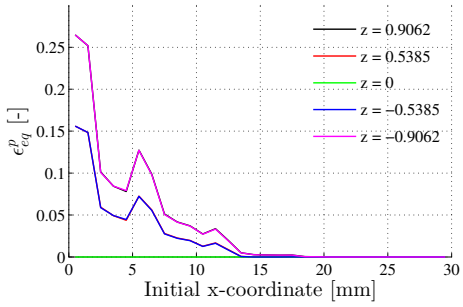

Figure 6.9: Equivalent plastic strain at the different integration points for friction coefficient 0.2.

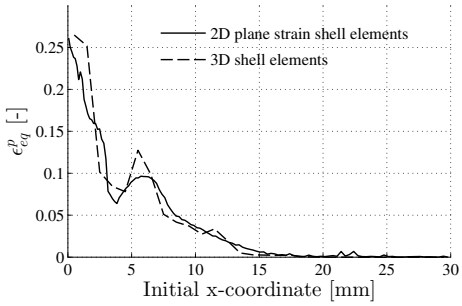

Figure 6.10: Equivalent plastic strain for the plane strain and shell element simulations for friction coefficient 0.2.

6.3 Comparison of results

For both the 2D plane strain model and the 3D shell model, the value of the friction coefficient did not influence the equivalent plastic strain field significantly. Friction coefficient 0.2 was chosen as representative. The equivalent plastic strain from the 2D plane strain and 3D plane stress simulation are compared in Figure 6.10. From the 2D analysis, plastic strains were extracted from elements in the upper half of the plate with corresponding position to the uppermost integration point of the 3D analysis. The plastic strains along the element row in the middle of the plate are extracted from the 3D model.

According to the figure, the predicted equivalent plastic strain fields are similar for the 2D and 3D simulations. The 2D model was simulated using von Mises' and the 3D model was simulated with the Barlat yield function, but the choice of yield function seems to be of minor importance. As observed, the resolution of the results is better for the 2D simulation due to the smaller elements compared to the 3D simulation. The 2D simulation serves as a validation of the 3D simulation, from which the equivalent plastic strain field and the hardening values are extracted and mapped to the models of P and CB specimens.

6.4 Concluding remarks

- A 2D plane strain shell and a 3D shell model of the forming process of the sheets were established, and simulations were performed to investigate the equivalent plastic strain field in the bends.
- The two models predicted similar equivalent plastic strain fields.
- Following the plate centre line, plastic strains were present up to 17 mm from the symmetry line of the bend. The maximum value of equivalent plastic strain was 27 %, an it decreased non-linearly with increasing distance from the symmetry line of the bend.
- The effect of the friction coefficient on the equivalent plastic strain field appeared

to be negligible.

- Subsequently, the equivalent plastic strain field and corresponding hardening values were extracted from the 3D shell simulation to established finite element models of the P and CB specimens. Two forming histories were mapped to the P and CB models, one with the same through-thickness value of ϵ^p_{eq} and one with varying through-thickness value.

Chapter 7

Point-connector model parameters

In this chapter the calibrations of the point-connector model for SPR and SPS are presented. A finite element model of the cross test was established, and the point-connector model was fitted to experimental results from the cross test by a reverse engineering approach. Subsequently, the calibrations were validated by finite element simulations of the SLJ and peeling tests.

The simulations were performed using LS-DYNA, as well as the SIMLab Metal Model to include the anisotropic constitutive model. Explicit time integration was performed and time scaling was applied to reduce the computational time. Monitoring of the energy balance was done to ensure that quasi-static conditions were fulfilled. For most of the simulations, a stiffness based hourglass control was employed. However, for some of them a viscous based hourglass control gave best results.

7.1 Calibration

The theory of the point connector model was presented in Section 2.2.1. To recapitulate, the parameters are f_n^{max}, f_t^{max}, δ_n^{fail}, δ_t^{fail}, ξ_n, ξ_t, α_1, α_2, α_3 and the diameter of the rivet or screw d. The values of the parameters were determined by a reverse engineering approach using the software LS-OPT. This software carried out simulations of the C tests with varying combinations of parameter values, and optimized the parameters to fit the experimental force-displacement curves. Initial estimates of the parameters were found by inspecting the force-displacement curves.

The C specimens were modelled with nominal geometry (Figure 3.11), as shown in Figure 7.1. In the experimental tests, the specimens were clamped using solid metal blocks with bolts through the holes of the plates. As the bolts were tightened firmly, it was assumed that the clamping was well represented by modelling the clamped parts of the plates as rigid bodies (*MAT_020) with spatial constraints. The unclamped parts of the

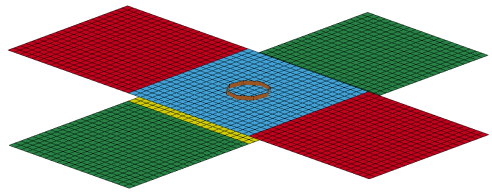

Figure 7.1: Model of C test.

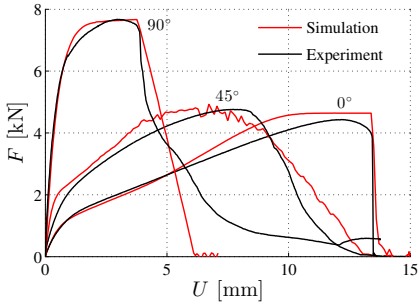

Figure 7.2: Results from the calibration of the point connector model for SPR.

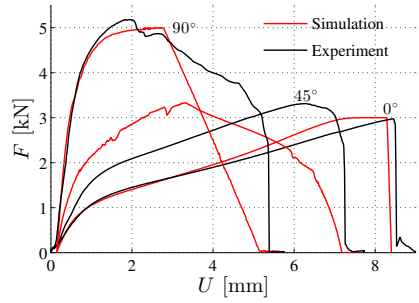

Figure 7.3: Results from the calibration of the point connector model for SPS.

plates were modelled with the anisotropic material model. Like in the experiments, the material of the top plate was oriented in the 90 degree direction and the material of the bottom plate was oriented in the 0 degree direction. The geometry was discretized using 2400 3D shell elements, whereas 800 were deformable and 1600 rigid, with an element size of 2 mm $\times$ 2 mm and five integration points through the thickness. A two-sided contact formulation (*CONTACT_AUTOMATIC_SURFACE_TO_SURFACE_ID) was applied between the plates, in order to account for possible contact forces, likely to occur for the shear loading tests. The friction coefficient was set to 0.2. The point-connector model is implemented in LS-DYNA, with the keyword *CONSTRAINED_SPR2. The node defining the position of the connection was placed between the plates in the centre of the cross.

The rigid parts of the bottom plate was fixed in space, while a prescribed velocity, depending on the loading direction, was assigned to the rigid parts of the top plate. The velocity was assigned as a smooth function, to avoid numerical noise. The force and displacement were extracted from the moving rigid part.

The results from the calibrations for SPR and SPS are plotted in Figure 7.2 and 7.3, respectively, and the parameters obtained in the calibration procedure are given in Table 7.1. Note that the numerical diameters of the rivet and screw are 12 mm and 6 mm, respectively. The numerical curves in Figure 7.3 are shifted 0.15 mm to better match the experimental curves, as some sliding of the clamping device occurred in the start of the screwed C tests, causing some error in the displacement measurement.

As seen, the force-displacement curves for SPR are well reproduced, both with respect to the maximum force level, ductility, softening and fracture. For pure normal loading (C-0

Table 7.1: Parameters of the point connector model calibrated to SPR and SPS.

Symbol	Unit	SPR	SPS	Description
f_n^{max}	[N]	4640	3000	Maximum pure normal force
f_t^{max}	[N]	7650	5000	Maximum pure shear force
δ_n^{fail}	[mm]	6.25	2.00	Deformation at failure for pure normal deformation
δ_t^{fail}	[mm]	6.00	4.80	Deformation at failure for pure shear deformation
ξ_n	[-]	0.90	0.90	Where softening starts for pure normal deformation
ξ_t	[-]	0.60	0.50	Where softening starts for pure shear deformation
α_1	[-]	0.10	0.05	Initial value of the damage parameter α
α_2	[-]	0.30	0.65	Value of α when softening starts
α_3	[-]	3.00	1.40	Final value of α
d	[mm]	12.0	6.0	Numerical diameter

test), it is seen that the force is slightly over-predicted before softening starts. It was possible to bring this force level down, at the cost of not matching the start of the curve. The last part of the softening in pure shear loading was mainly due to frictional forces caused by jamming of the rivet between the sheets. Thus, it is believed that the linear decrease predicted by the model is a result in agreement with the physics of the problem. The results of the mixed mode test (C-45) are also well reproduced. The maximum force level as well as the softening behaviour are correctly predicted.

For the SPS connection, the results from the simulation with pure normal loading correspond well with experiments, both considering the maximum force level and ductility. It was impossible to obtain a perfect fit for the C-45 an C-90 test simultaneously. More effort was put into obtaining a good fit for the pure shear loading case, as the connections in the component tests are mainly loaded in shear. In the pure shear loading, the curve was well predicted up to maximum force, but the linear softening until fracture observed in the experiments was not captured by the model. In the mixed loading mode the maximum force level was well predicted, but the corresponding displacement was significantly under-predicted. Additionally, the simulation predicted a rather gradual fracture while a more abrupt fracture was observed in the C-45 test. Different combinations of parameters were tried without improved results. By using a numerical diameter of 4 mm instead of 6 mm, a better fit was obtained in pure normal load at the expense of shifting the results in pure shear towards larger displacements. A possible explanation is related to the diameter of the screw. The diameter of the screw head is larger than the diameter at the tip, while for the rivet the diameter is approximately equal at the head and legs. This is seen in Figure 3.8 and 3.9a. The influence of the wider head of the screw is not accounted for in the model.

The following discussion is purely based on experimental results. It is included in this section as the results may highlight aspects of the results in Figure 7.2 and 7.3. Figure 7.4 shows the normalized force and normalized displacement fracture loci from the C tests for SPR and SPS. In Figure 7.4a the mean values of the maximum forces from the C tests are plotted, normalized to the mean pure shear force (C-90) on the abscissa axis and the mean normal force (C-0) on the ordinate axis. For the mixed mode point (45°) the force is decomposed before normalization. The normalized standard deviations are also included.

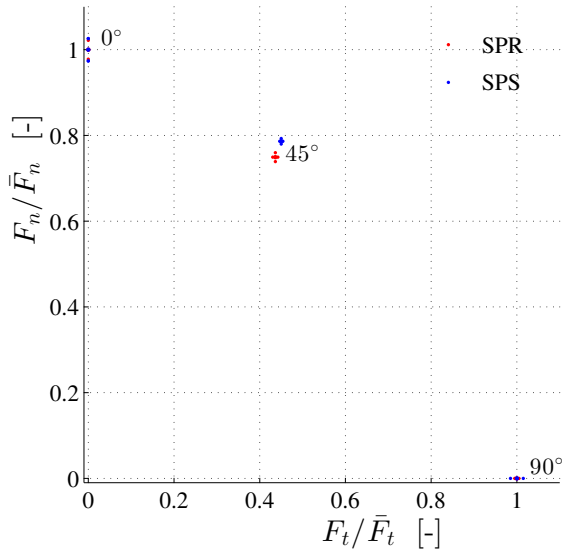

(a) Force.

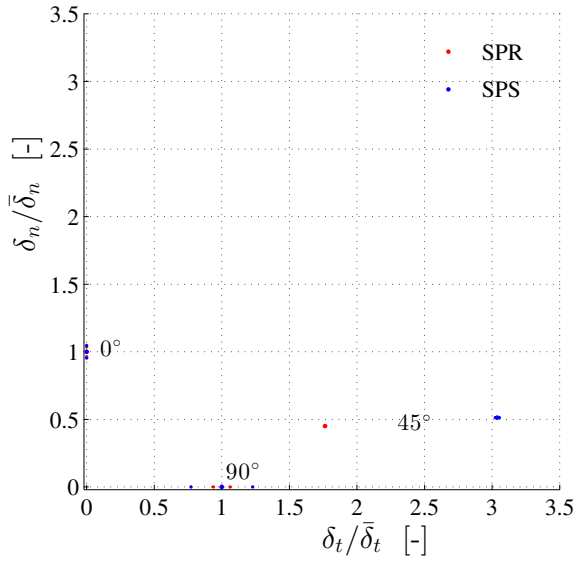

(b) Displacement.

Figure 7.4: Normalized fracture loci from C tests, including mean value ± one standard deviation.

Correspondingly, the points in Figure 7.4b are the mean values of the displacements at maximum force, normalized in the same way as the force.

Ideally, the fracture loci should be based on characteristic points for fracture. However, characteristic fracture points were hard to determine from the C tests (recall Figure 4.31a). Of this reason, the fracture loci are based on the maximum forces and the corresponding displacements instead. Possible strength during softening is thus not accounted for.

Interestingly, the shapes of the force loci are similar for the rivets and screws. This indicates that the point-connector model should be able to reproduce the maximum force level for the three loading directions in the C tests equally well for SPR and SPS. As seen in Figure 7.2 and 7.3, this is also the case. When considering the displacement loci (Figure 7.4b), it is evident that the shapes are dissimilar. In the C tests with rivets, the displacement at maximum force for the mixed loading mode was approximately two times the displacement at maximum force in pure shear. For the screws, this ratio was approximately three. The predicted and experimental response of SPR in the cross tests are similar (see Figure 7.2). From the results for SPS (see Figure 7.3), it is evident that the shapes of the curves are similar to the results observed for SPR. This indicates firstly that the fracture loci are well-predicted for SPR, and secondly that the model forces the fracture loci of SPS to be similar the fracture loci of SPR. The point-connector model is tailored for self-piercing rivet connections, and does not seem to be sufficiently flexible to describe the fracture behaviour of SPS connections.

7.2 Validation

The calibrations of the point-connector model for rivets and screws are validated by finite element simulations of the SLJ and P tests.

7.2.1 Simulation of single lap-joint test

The SLJ specimens were modelled using a nominal geometry (Figure 3.14), and the FE model is shown in Figure 7.5. In total 1920 3D shell elements with five through-thickness integration points represented the geometry, whereas 320 elements constituted rigid parts and 1600 constituted deformable parts. The size of the deformable elements was 2 mm $\times$ 2 mm. In the experimental SLJ tests, 40 mm of each end of the specimens were clamped using mechanical grips. The clamped parts were modelled as rigid bodies (*MAT_020). One end was fixed in space and the other was assigned a velocity in the longitudinal direction using a smooth curve to reduce numerical oscillations. The anisotropic material model was assigned to the deformable elements. The simulations were performed with the material reference direction in the transversal direction of the specimen. In order to account for possible contact forces, a two-sided contact formulation (*CONTACT_AUTOMATIC_SURFACE_TO_SURFACE_ID) was applied between the plates with a friction coefficient of 0.2. The force and displacement were obtained from the moving rigid part. The connection was included using the *CONSTRAINED_SPR2 keyword, with the node defining the position of the connection placed between the plates in the centre of the overlap area.

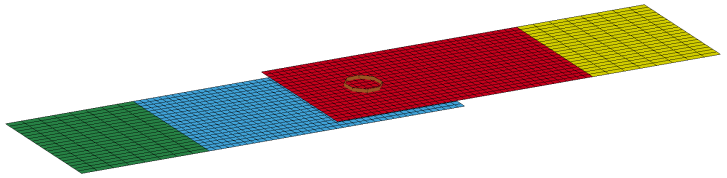

Figure 7.5: Model of SLJ test.

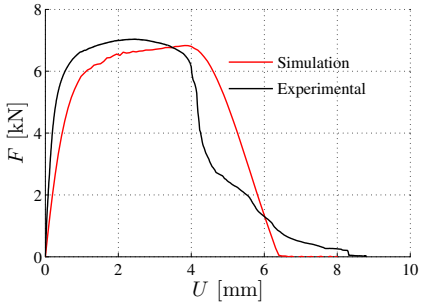

Figure 7.6: Results from the simulation of the riveted SLJ test.

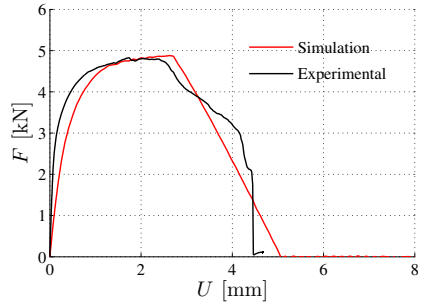

Figure 7.7: Results from the simulation of the screwed SLJ test.

The simulations of the SLJ tests for SPR and SPS are compared to experimental data in Figure 7.6 and 7.7, respectively. As seen, the results match well, both for rivets and screws. The maximum forces as well as the ductilities are well predicted. The simulation for SPR under-predicts the stiffness in the initial part, and the maximum force and softening part are reached for higher displacements than in the tests.

The SLJ test is a shear dominated problem, but with a small normal load component. Thus, with reference to Figure 2.7, the SLJ loading case is located slightly above the shear loading axis. The ability of the model to reproduce the SLJ results indicates that the calibration is satisfactory for this region of loading.

7.2.2 Simulation of peeling test

The P specimen was modelled with nominal geometry (Figure 3.16) and is shown in Figure 7.8. The model consisted of 1920 3D shell elements, of which 320 were rigid and 1600 deformable. The size of the deformable elements was 2 mm × 2 mm, and through-thickness integration was performed with five integration points. As for the SLJ simulations, the clamping was represented by modelling 40 mm at each end of the specimen as rigid bodies (*MAT_020). One end was fixed, and the other was assigned a velocity in the longitudinal direction using a smooth curve. Like in the experimental P tests, the material in the deformable parts was oriented in the transversal direction. As contact between the sheets occurred in the tests, a two-sided contact formulation (*CONTACT_AUTOMATIC_SURFACE_TO_SURFACE_ID) was applied with a friction

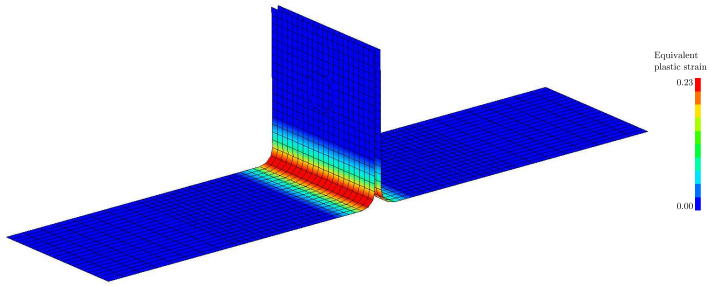

Figure 7.8: Model of P test. The mapped equivalent plastic strain field is displayed.

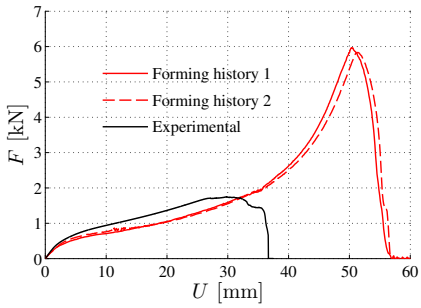

Figure 7.9: Simulation of riveted P test.

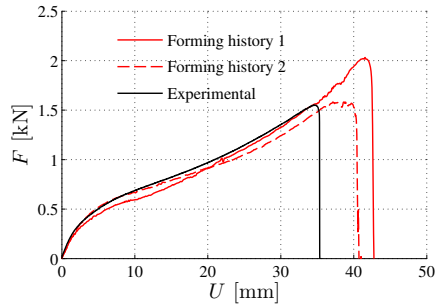

Figure 7.10: Simulation of screwed P test.

coefficient of 0.2. Again, force and displacement were obtained from the moving rigid body.

The connection was included using the *CONSTRAINED_SPR2 keyword. The response from the peeling simulations was highly dependent on the placement of the connection. In the model the connection was placed at a distance 15.86 mm and 14.37 mm from the top edge for SPR and SPS, respectively. This corresponded to the position of the connections from the experiments, found in Table 3.4.

To account for work hardening caused by bending of the rolled sheets, plastic strains were extracted from the forming process simulation and mapped into the model of the peeling test. Two different forming history configurations were extracted from the equivalent plastic strain field displayed in Figure 6.9 and mapped to the thorough-thickness integration points of the peeling test model. In forming history 1 the average of the values through the thickness was mapped to all integration points and for forming history 2 through-thickness variation taken into account. In Figure 7.8 the mapped field is shown for the outermost integration point with forming history 2.

In Figure 7.9, the results from the simulations of the P tests is compared to experimental data, both for SPR and SPS. Remarkable differences are observed in the results for SPR and SPS.

For the SPR simulation, the strength of the connection is massively over-estimated. The maximum force is approximately three times higher and the corresponding displacement

(a) Test.

(b) Simulation.

Figure 7.11: Comparison of deformed P specimen after test and after simulation with SPR connection.

was increased with approximately 70 % compared to experimental data. In the first part of the simulation the force is under-predicted by approximately 25 %. As maximum force is reached in the experiments, the force in the simulation increase continuously until fracture. A deformed specimen from the P test is compared to the simulated deformed specimen in Figure 7.11. The effect of the over-prediction of the strength is clearly seen, as the sheets are considerably more stretched out in the simulation.

The P test with SPS connection is satisfactorily reproduced in the simulation. As seen in Figure 7.10, the shape of the curves match closely. However, the displacement at fracture is over-estimated by approximately 15-20 %. The effect of forming history is evident. When through-thickness variation of the initial plastic strains is taken into account (forming history 2), the maximum force prediction is exceptional, though occurring slightly later than in the tests. It is noteworthy that some scatter was observed for the ductility of the P tests with SPS (see Figure 4.28), and that the predicted fracture, in fact, is in the range of the scatter.

Again with reference to Figure 2.7, the P test is located slightly to the right of the normal loading axis. The P test is a tensile dominated problem with a small shear component. Of this reason, the tangent of the fracture locus in tension should point towards the correct fracture value in peeling to get accurate numerical predictions. For SPS, this reduced peeling resistance is well-predicted. For SPR, however, the peeling resistance is over-estimated, which suggest that the peeling test should be included in the calibration of the point-connector model for rivets. This corresponds with results found by the developers of the model [12]. A further development of the discussed point-connector model should include reduction of the peeling resistance for rivets.

7.3 Concluding remarks

- A large-scale finite element model developed for self-piercing rivets was calibrated for self-piercing rivets and self-piercing screws by a reverse engineering approach using experimental data from cross tests in three directions.
- The calibrations were validated by simulation of the SLJ and P tests.

- For SPR, predictions of the model corresponded to experimental results for the C-0, C-45, C-90 and SLJ tests. For the peeling test, however, the simulations massively over-predicted the maximum force and the corresponding displacement. To improve the results for rivets, the peeling test should be included in the calibration.
- For SPS, the model was calibrated such that the simulations corresponded to experimental results from the C-0 and C-90 test, at the expense of under-predicting the displacement for maximum force for the C-45 test. It was not possible to calibrate the model such that predictions corresponded to experimental results in all three loading directions simultaneously. The SLJ and peeling tests were well reproduced.
- To improve the model using rivets, the peeling resistance should be reduced.
- For SPS, the point-connector model was not able to reproduce the normalized displacement fracture locus observed in the tests. To adjust the model to better predict the screw behaviour, modifications are necessary for mixed loading modes.

Chapter 8

Component test simulations

To validate the calibrations of the constitutive model and the point connector model, simulations of the CB tests were carried out. The ability of the models to describe a highly complex loading situation with coupling of several physical phenomena is thereby investigated. In addition, studies on the effect of forming history, yield surface and mesh size were performed. Table 8.1 summarizes the program of the numerical simulations of the CB tests.

In Chapter 6 the bending process of the plates was simulated, both using 2D plane strain shell elements with von Mises' yield function, and 3D shell elements with the Barlat yield function. These simulations showed significant plastic strains in the bends, with a strong through-thickness variation. To most accurately represent the physics of the problem, updated values for the equivalent plastic strain field and the corresponding isotropic hardening values from the bending process simulations were mapped to the finite element models of the CB tests. The model was updated using the same protocol as in the P simulation, including two forming history configurations as displayed in Table 8.2. In addition, simulations without initial plastic strains were performed. A 2 mm mesh was applied to investigate the effects of the forming history.

To study the effect of different yield surfaces, simulations were performed with both the Barlat and von Mises' yield functions as well as a high exponent yield function. The high exponent yield function may be regarded as a generalized isotropic yield surface, lying in-between von Mises' and Tresca's surfaces. The high exponent yield surface was obtained by modifying the coefficients in the Barlat yield function; all coefficients in the transformation matrices of Equation (2.29) were fixed to 1, and the exponent m of Equation (2.28) was set to 8.

The simulations investigating the effect of yield surface were performed with a mesh size of 2 mm and 5 mm. For the 2 mm simulations, forming history 2 was applied. The motivation for performing simulations with 5 mm mesh is related to the current standards in the automotive industry, where crash simulations are commonly performed with 5 mm mesh to limit the computational time. The simulations with 5 mm mesh were performed without initial plastic strains, as the mesh was too coarse to accurately

Table 8.1: Numerical program for CB simulations.

	Forming history			Yield surface		
Mesh size	No	1	2	Barlat	High exponent	von Mises
Small shells (2 mm)	x			x		
		x		x		
			x	x		
			x		x	
			x			x
Large shells (5 mm)	x			x		
	x				x	
	x					x

represent the plastic strain field from the forming process. With this mesh size, the geometrical discretization of the CB specimen was believed to be too coarse to correctly represent the actual geometry.

All CB simulations were carried out with explicit time integration using LS-DYNA with the SIMLab Metal Model. A stiffness based hourglass control was employed, and the energy balance was monitored in order to ensure negligible hourglass energy.

The model of the CB specimens with the small mesh size is shown in Figure 8.1, including a contour plot of the initial equivalent plastic strain. The simulations of the CB tests were modelled with nominal geometry (Figure 3.18). Half of the specimen was modelled to reduce the computational time, with symmetry boundary conditions along the symmetry plane. The symmetric buckling patterns observed in the experiments justified this choice. The clamped part of the specimen was modelled as a rigid body using the *MAT_020 material, with constrained displacement in all directions. The impact of the trolley was modelled as a rigid wall impact (*RIGIDWALL_PLANAR_MOVING_FORCES). The rigid wall was chosen to represent the impactor to avoid any discretization error in the contact computations. Half of the trolley mass (197.75 kg) and a velocity of 9.90 m/s were assigned to the rigid wall. The velocity corresponds to the average of the measured velocity in the dynamic CB tests. The simulations were terminated after 18 ms, to obtain higher crushing distance than in the experiments. Contact was modelled using an automatic single surface contact algorithm (*CONTACT_AUTOMATIC_SINGLE_SURFACE) for both sheets to handle self-contact, as well as a two-sided contact algorithm between the sheets (*CONTACT_AUTOMATIC_SURFACE_TO_SURFACE_ID). A friction coefficient of 0.3

Table 8.2: Forming history configurations.

Forming history	Mapped to integration point
1	Same value through the thickness
2	Varying value through the thickness

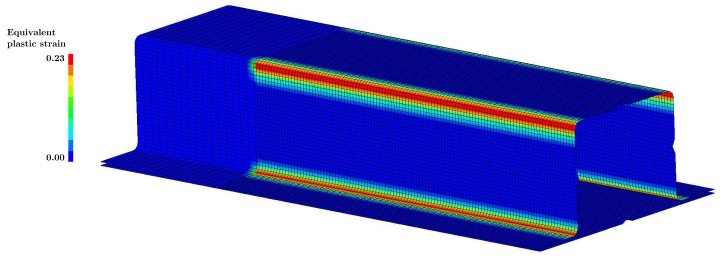

Figure 8.1: The model of the CB specimen with 2 mm mesh. The mapped equivalent plastic strain field for the outermost integration point is indicated.

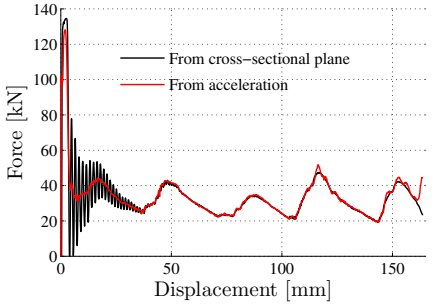

Figure 8.2: Comparison of force calculations in CB simulations.

was used. The point connector model was included, with the placement of the connections according to the nominal geometry of the SPR and SPS CB specimens. The triggering was performed by moving two nodes at each wall inwards or outwards, according to the triggering in the tests.

Displacement and acceleration were extracted from the impactor. The impact force was obtained by multiplying the acceleration with the mass of the impactor. At first, a cross-sectional plane was defined, and the element forces in the plane summed to obtain the force. However, large oscillations, possibly due to stress waves, were present in the force signal. Figure 8.2 compares the two force calculations. As seen, the force calculated from the acceleration coincide with the force from the cross-sectional plane, except for the oscillations. Hence, the force calculated from the acceleration was used.

The mean force was calculated from Equation (4.5), where the energy absorption was calculated according to Equation (4.6).

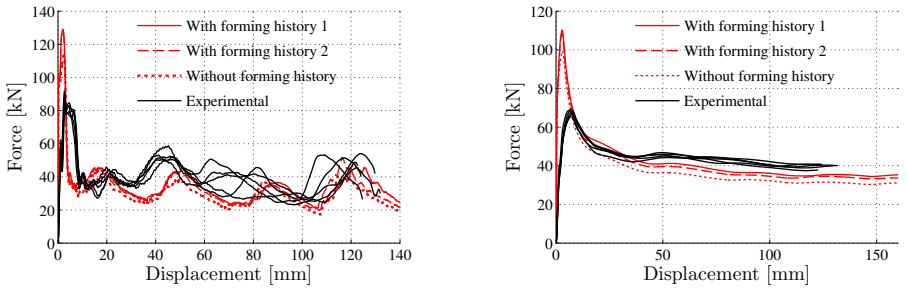

(a) Force. (b) Mean force.

Figure 8.3: Results from simulations of dynamic, riveted crash box tests for varying forming histories. Small mesh size.

(a) Test sample. (b) Forming history 1. (c) Forming history 2. (d) No forming history.

Figure 8.4: Effect of forming history on deformation pattern, SPR.

8.1 Rivets

8.1.1 Effect of forming history, small shells

Figure 8.3 shows the effect of the forming history on the force and mean force level of the SPR crash box. These simulations were carried out using a fine shell model (2 mm) and the Barlat yield function. The response is similar to the experimental data. As seen in Figure 8.3a, an initial peak load of between 110 and 130 kN is reached before the force fluctuates about approximately 40 kN. The initial peak load is highly dependent on the type and size of the triggers. In the simulations, smaller triggers were used than in the physical tests, which may explain why the peak is overly estimated in the simulations. The shape of the local peaks after initiation of the progressive buckling is well reproduced. However, the local maximum forces are slightly under-predicted, and the peaks are located a little later than in the tests. These local peaks correspond to forming of the different lobes. The forces are slightly underestimated throughout the history.

As the mean force is closely related to the force, similar observations are made and a

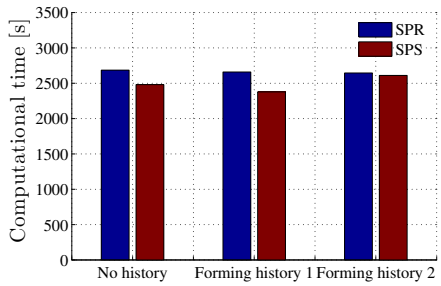

Figure 8.5: Effect of forming history on the computational time.

generally good correlations with the experiments is found (see Figure 8.3b). The initial peak is over-estimated, and during progressive buckling the mean force is slightly lower than in the tests.

The effect of the forming history is significant. Forming history 1 renders best results, while the simulations without forming history gives the lowest predictions. Forming history 1 gives marginally better results than forming history 2. The simulated mean force at 100 mm displacement using forming history 1, forming history 2 and no forming history are 89.5 %, 85.6 % and 79.9 %, respectively, of the average of the mean forces for 100 mm displacements in the experiments. As seen from Figure 8.5, the effect of forming history is however negligible for the computational time.

During progressive buckling, most of the energy is dissipated by the corners of the top-hat specimen. Thus, the energy dissipation, and hence the mean force, are depending on whether the initial hardening is accounted for or not. This may explain why the mean force is under-predicted when the forming history is not taken into account. Another possible explanation for the under-predicted energy absorption is related to the calibration of the hardening. The hardening parameters were calibrated only up to necking. Larger strains might give lower stress values, and therefore lower plastic dissipation, in the simulations than in the experiments.

The deformed specimens in the simulations are compared in Figure 8.4. A picture of an experimental sample is included. As seen, the same deformation mode was triggered in the simulations as in the tests. Minor differences are observable for the folding patterns. For instance, the lobes on the corners are more round in the simulation without forming history, while they have sharper edges in the simulations with forming history 1 and 2. An observation is made for the inward fold in the top sheet above the clamping, this fold is most prominent for the simulations without forming history, and least prominent for the simulation with forming history 2.

In the experiments a stiff response of the sheets near the rivets was observed, such that edges were introduced in the folding pattern of the flanges (see Figure 4.58a). This effect was not seen in the simulations.

From the experimental tests, three deformation modes and one failure mode were found for the rivets (see Section 4.5.1.2). No rivets failed in any of the numerical simulations.

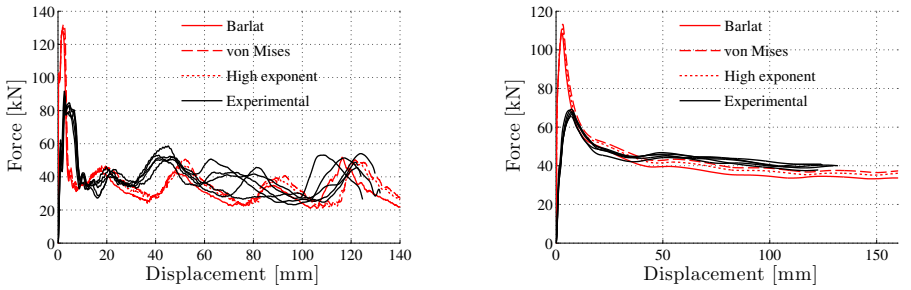

(a) Force. (b) Mean force.

Figure 8.6: Results from simulations of dynamic, riveted crash box tests for varying yield functions with the small mesh size.

(a) Test sample. (b) Barlat. (c) von Mises. (d) High exponent.

Figure 8.7: Effect of yield function on deformation pattern for small shells, SPR.

8.1.2 Effect of the yield surface, small shells

The effect of the yield function on the force and mean force levels was investigated by use of a fine shell mesh (2 mm) and forming history 2. The results are presented in Figure 8.6. Small deviations are found between application of the different yield surfaces. As seen in Figure 8.6a, the peak load is over-estimated, and the force is slightly under-estimated throughout the deformation. The initial peak load is approximately 130 kN for all simulations, and the force during progressive buckling fluctuates about approximately 40 kN. Again, the local peaks are well reproduced, with some under-estimation of the local peak forces as well as the deformation at which they occur. Good results are also obtained for the energy absorption, see Figure 8.6b. The mean force is initially higher than in the experiments, but good agreement is seen for the progressive buckling behaviour.

An effect of the yield function is observed. With respect to the mean force good agreement is seen for von Mises' yield function. The high exponent yield function gives slightly lower response, while the Barlat yield function predicts the lowest response. At 100 mm displacement the mean force is 85.6 %, 95.9 % and 92.9 % of the average experimental result for the Barlat, von Mises' and the high exponent yield surfaces, respectively. How-

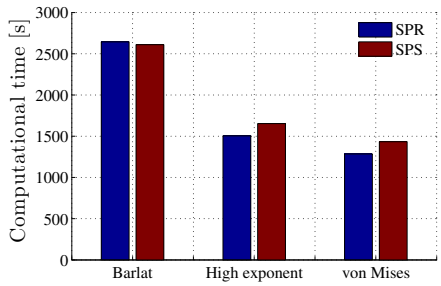

Figure 8.8: Effect of yield function on the computational time for small shells.

ever, up to about 35 mm displacement the Barlat yield function yields best results. When considering the mean force level, application of von Mises' is sufficient.

A possible explanation for the observed differences is related to the equi-biaxial point on the yield surface. In the calibration of the Barlat yield function the biaxial yield stress was not constrained. For von Mises' yield surface, however, the biaxial yield stress equals the uniaxial yield stress ($r_{EqB} = 1$). Recall Figure 5.17, where the difference at the equi-biaxial point is clearly seen. During crushing of the crash boxes, the corners were dominated by a biaxial tensile stress state. Thus, an increase of strength is expected for von Mises' compared to the Barlat yield function, which might explain the observed results.

Although the von Mises' yield function gives the best results in this case, this is not necessarily the case if a fracture criterion is applied. In this case it is believed that an anisotropic yield function is necessary to obtain good results.

The deformed specimens from the simulations are shown in Figure 8.7. A test sample from the experiments is included for comparison. The same deformation mode was seen in all simulations. Only small differences were observed for the different yield functions. As seen before, the inward fold on top of the top sheet above the clamping is most prominent for the Barlat simulation.

No connections failed in these simulations. The point-connector model was not able to capture the fractures of the rivets, probably due to the over-estimated peeling resistance.

Figure 8.8 shows the effect of yield surface on the computational time, also including the simulations with SPS. As seen, the Barlat yield function doubles computational time compared to von Mises' yield function. It should be mentioned, however, that experience has indicated that the computational time for the Barlat yield function is problem dependent. The high exponent yield surface gives slightly increased computational time compared to von Mises'. If the mean force is the main concern, use of von Mises' gives highly reduced cost compared to the Barlat yield function both with respect to the calibration procedure and computational time.

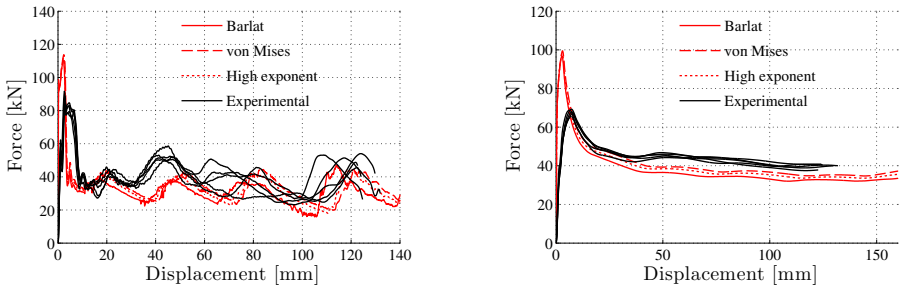

(a) Force. (b) Mean force.

Figure 8.9: Results from simulations of dynamic, riveted crash box tests for varying yield functions with large shells.

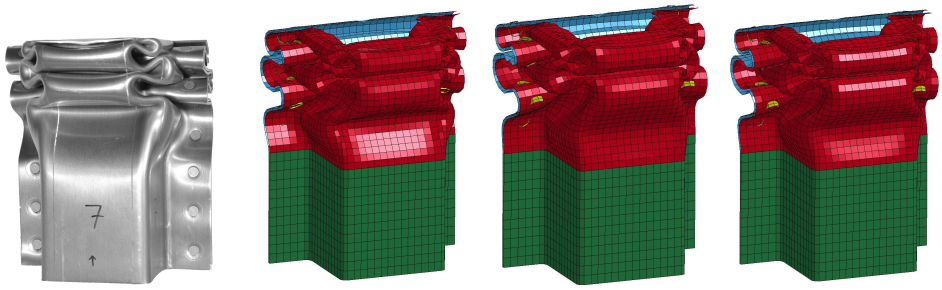

(a) Test sample. (b) Barlat. (c) von Mises. (d) High exponent.

Figure 8.10: Effect of yield function on deformation pattern for large shells, SPR.

8.1.3 Effect of yield surface, large shells

The force-displacement history as well as the mean force evolution from the simulations with large shell elements are shown in Figure 8.9. Generally, a lower force level is predicted by the large shell simulations compared to the small shell simulations. The initial peak load is still overly predicted, with values of approximately 110 kN. The local force peaks during progressive buckling are well reproduced.

Due to the under-predicted force, the mean force level is lower in the simulations than in the experiments. It is seen that von Mises' yield function gives the best result, while the Barlat yield function gives the least good. The mean force at 100 mm displacement for the Barlat, von Mises and high exponent yield functions is 82.0 %, 91.0 % and 87.6 % of the average experimental mean force. It is noteworthy that up to 40 mm displacement, the mean force is satisfactorily predicted for all surfaces. This is probably due to the over-estimated initial peak, which increases the calculated energy absorption.

From section 8.1.1 it was found that including forming history increased the force level. No forming history was included for the large shell simulations, which may partly explain the under-prediction of the force.

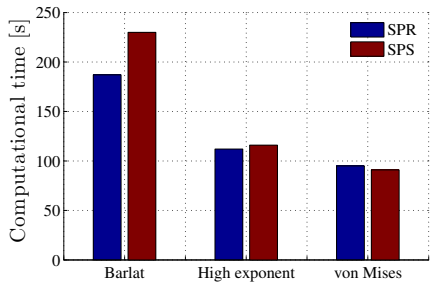

Figure 8.11: Effect of yield function on the computational time for large shells.

It is noted that higher force was predicted for the corresponding 2 mm simulation compared to the 5 mm simulation. By investigating the geometrical representation of the specimen, it is evident that the 5 mm mesh is to coarse to describe the geometry precisely. This is particularly critical at the corners of the hat section, where large plastic deformations an thereby high energy absorption is found. This is believed to contribute to the under-prediction of the force. Figure 8.10 shows the deformed specimens in the large shell simulations.

No connections failed in these simulations. The point-connector model was not able to reproduce the deformation in the connections observed in the tests.

The effect of yield function on the computational time for large shells is presented in Figure 8.11. The results with SPS are also shown. As for the small shells, a significant difference is observed between the Barlat yield function and the von Mises and high exponent yield functions. By comparing with results for the small shells (Figure 8.8), it is observed that the computational times for the large shells are reduced with a factor of 10. Thus, depending on the application, a large amount of computational time is avoided by using von Mises' yield function with large shells. If the mean force is of interest, this leads to an error at approximately 10 %.

8.2 Screws

8.2.1 Effect of forming history, small shells

Figure 8.12 shows the effect of the forming history on the force and mean force level of the SPS crash box. These simulations were carried out using a fine shell model (2 mm) with the Barlat yield function. The computational time was shown in Figure 8.5. As seen in Figure 8.12a the results for the force level are satisfying. The force level is slightly lower in the simulations than in the experiments, but the initial peak is higher. The local peaks during progressive buckling are for these simulations very accurately reproduced, both with respect to the peak forces and the locations. It is seen, however, that the first local peak is occurring slightly too soon.

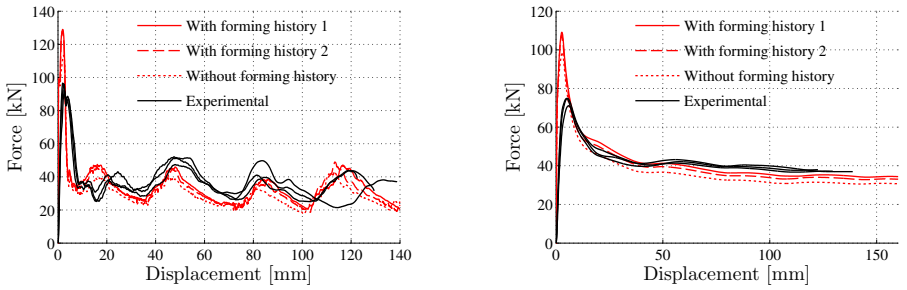

(a) Force. (b) Mean force.

Figure 8.12: Results from simulations of dynamic, screwed crash box tests for varying forming histories. Small mesh size.

(a) Test sample. (b) Forming history 1. (c) Forming history 2. (d) No forming history.

Figure 8.13: Effect of forming history on deformation pattern, SPS.

The results for the mean force are also good, as the post buckling response is well predicted. The effect of forming history on the energy absorption is significant. Forming history 1 renders the closest match, while the simulation without forming history predicts a too low mean force. The mean forces at 100 mm displacement are 91.4 %, 87.3 % and 80.7 % of the average of the experimental data for the simulations with forming history 1, forming history 2 and no forming history, respectively.

The deformed specimens from the simulations are shown in Figure 8.13. As in the simulations with rivet connections the same deformation modes are predicted, and only small differences are observed.

In contrast to the simulations with SPR, fracture of connections was observed in the simulations with SPS. Table 8.3 summarizes the connection fractures in the simulations. The numbering of the connections follows the same system as before (see 4.33), where connection 1 at the front end of the specimen. A small influence of the forming history on the failure is seen for the screws. Connection seven fractured in all simulations. However, while connection three fractured in the simulations with no forming history and forming history 1, connection two fractured in the simulation with forming history 2. Recall

Table 8.3: Effect of forming history on failure of screws.

Connection name	No forming history	Forming history 1	Forming history 2
1			
2			F
3	F	F	
4			
5			
6			
7	F	F	F

Table 4.6, where the observed deformation and failure modes of screws in the dynamic CB tests are summarized. Deformation or failure was often observed in connection two and three, and some times in connection seven in the experiments. These deformations are relatively well predicted by the simulations. However, the observed deformations or fractures of connection one, five and six are not captured by the point-connector model.

8.2.2 Effect of yield surface, small shells

The effect of the yield function on the force and mean force levels are presented in Figure 8.14. The computational time was shown in Figure 8.8. A fine shell mesh (2 mm) was used where the forming history was accounted for. Forming history 2 was applied. The results are very satisfying, and the same trends as before are observed. The initial peak is overly estimated, and the force during progressive buckling is marginally under-estimated. The local peaks are excellently predicted, both with respect to the peak forces and the locations.

Furthermore, the mean forces are also accurately reproduced. A small effect of the yield surface is evident, as von Mises' yield function gives best result and the Barlat yield function the least good. The mean force predicted with von Mises' yield function is indistinguishable with the experimental data for displacement larger than 50 mm. For smaller displacement von Mises' and the high exponent yield function over-predicts the

Table 8.4: Effect of the yield function on failure of screws for small shell elements.

Connection name	Barlat	von Mises	High exponent
1			
2	F	F	F
3		F	F
4			
5			
6			
7	F		F

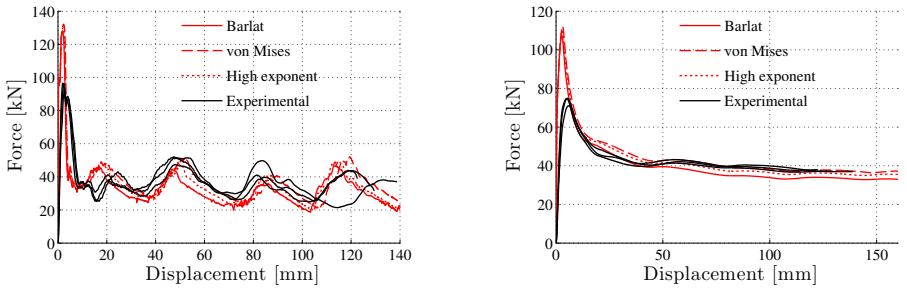

(a) Force. (b) Mean force.

Figure 8.14: Results from simulations of dynamic, screwed crash box tests for varying yield functions. Small mesh size.

(c) Test sample. (d) Barlat. (e) von Mises. (f) High exponent.

Figure 8.15: Effect of yield function on deformation pattern, SPS, small shells.

mean force, while the result with the Barlat is in accordance with experimental data.

Figure 8.15 shows the effect of different yield surfaces on the deformation pattern for the small shell simulations. The same deformation mode is observed in all simulations, with only slight differences. As mentioned in Section 8.1.1 the rivets affected the folding of the flanges of the CB specimens. This effect was less pronounced with screws. Hence, the deformation pattern in the flanges in the simulations with SPS is closer to the pattern observed in the experiments.

Also for these simulations some connections fractured. The observed connection fractures are given in Table 8.4. It is seen that the choice of yield function greatly affects the occurrence of fracture. Connection two failed in all simulations, connection three failed when using von Mises' and the high exponent yield functions, while connection seven failed when using the Barlat and the high exponent yield functions. It was also observed that the connections that fractured were located where the flanges were folded inwards. Again with reference to Table 4.6, it is seen that the deformation or fracture of connections two, three and seven are relatively well predicted by the point-connector model. The deformation of connection one, five and six was not captured.

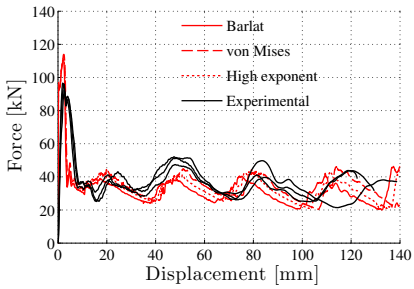

(a) Force.

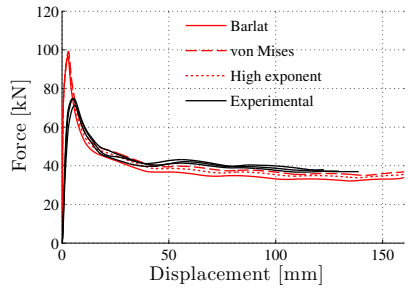

(b) Mean force.

Figure 8.16: Results from simulations of dynamic, screwed crash box tests for varying yield functions. Large shells.

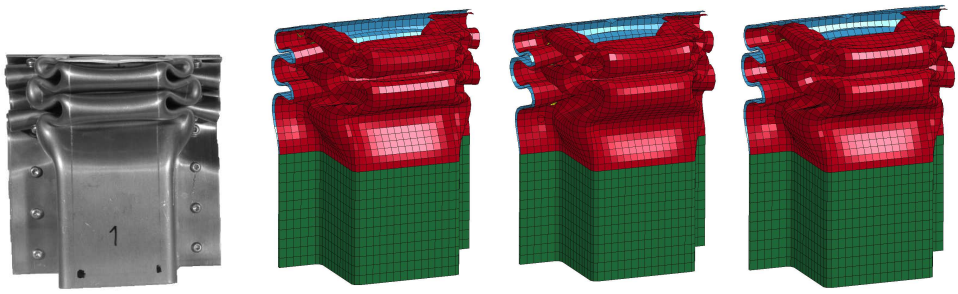

(c) Test sample. (d) Barlat. (e) von Mises. (f) High exponent.

Figure 8.17: Effect of yield function on deformation pattern, SPS, large shells.

8.2.3 Effect of yield surface, large shells

The force-displacement history and mean force from the simulations with large shell elements are plotted in Figure 8.16. The computational time was previously shown in Figure 8.11. A large shell mesh (5 mm) was used. No forming history was accounted for. The results are again satisfactory. As seen in Figure 8.16a, the initial peak is less over-estimated than before, and the force during progressive buckling is generally slightly under-estimated. Despite the coarse mesh, the local peak forces are almost correctly predicted.

The predictions of the mean force are again good, see Figure 8.16b. Up to 40 mm displacement the mean force is well estimated in all simulations. After 40 mm displacement the effect of the different yield functions becomes more pronounced. Best results are obtained using von Mises' yield surface, while the Barlat yield function gives the least good.

Figure 8.17 shows the deformed specimens from the simulations. The same buckling mode is seen, only with small differences. As for the large shell simulations with SPR connections the mesh seems too coarse to describe the geometry of the specimen precisely, particularly in the lobes in the corners.

Table 8.5: Effect of the yield function on failure of screws for large shell elements.

Connection name	Barlat	von Mises	High exponent
1			
2		F	F
3	F	F	F
4			
5		F	
6		F	F
7	F		

On fracture of the SPS connections, a significant effect of the yield surface is found for the large shells. Using the Barlat yield function, fracture was observed in connection three and seven, see Table 8.5. By applying von Mises' fracture was seen in connection two, three, five and six, while for the high exponent yield function fracture occurred in connection two, three and six. The fractures observed with von Mises' and the high exponent yield surface correspond very well with the experimental observations (see Table 4.6), as deformation or fracture was often seen in connections two, three, five and six. The point-connector model seems to predict connection fracture fairly well.

8.3 Concluding remarks

- Simulations of the CB tests were carried out for three different forming histories, three different yield surfaces (the Barlat, von Mises' and the high exponent) and two mesh sizes (2 mm and 5 mm) in order to validate the combined constitutive and point-connector model.
- The same global deformation mode was triggered in all simulations, and only minor differences were seen between the simulations.
- Except for the initial peak, the force was under-predicted with 5-20% in all simulations. The local peaks during progressive buckling were generally well reproduced. It is believed that the higher simulated peak is due to smaller triggering in the simulations than in the experiment. The under-predicted force is believed to be related to energy absorption in the corners of the crash boxes, as well as the calibration of the hardening parameters, which were calibrated only up to necking.
- A significant effect of the forming history was found for both SPR and SPS. Best results were obtained with forming history 1, followed by forming history 2, while significantly under-prediction was seen if no forming history was taken into account. The effect of forming history on the computational was negligible.
- The small shells predicted slightly better results than large shells with respect to the measured force and deformed shape, while the mean force was similar for the two mesh sizes when comparing for the same yield function and forming history.

The computational time for small shells was approximately ten times the time for large shells.

- Considering the effect of yield surface, the force and mean force were best predicted by von Mises', followed by the high exponent yield function, while Barlat under-predicted the forces more than the two other. This is probably related to the yield stress value in the equi-biaxial point, which is lowest for the Barlat yield function. The observation was independent of mesh size. For both small and large shells, the computational time using the Barlat yield function was approximately a factor of two higher than for the von Mises and the high exponent yield functions. It is believed that the differences between the yield functions would have been more pronounced if a fracture criteria was applied.
- Slightly better correspondence between experimental results and simulations was obtained with SPS compared to SPR. The mean force at 100 mm displacement was approximately 2 % higher for simulations with rivets compared to screws, using small shells. The corresponding difference from the experiments was 4 %. The deformed shape from the simulations was very similar, but in the experiments, different shapes of the flanges were observed. The absence of this edged shape of the flanges is believed to be one explanation for lower predicted difference in mean force for SPR compared to SPS in the simulations compared to experimental results.
- No rivets failed in any of the simulations. The point-connector model was not able to reproduce the rivet deformations or failures observed in the experiments. This is believed to be related to the fact that the stiff part of the bottom of the rivet is not modelled in the point-connector model.
- For the screws, however, fracture was found in all simulations. Applying the same yield function and mesh size, but different forming histories, showed fracture in two screws in all tests, though for different positions. It was observed an effect of the applied yield surface on the fracture of screws for both the small and large mesh, but no clear trend. Nevertheless, the Barlat yield function seems to predict least fracture, which is probably related to less energy absorption during the test. In the experiments, highly deformed or fractured screws were most frequently found on screw position 2, 3, 5 or 6. Similarities to this were found in the simulations. Deformation or fracture of connection number four was neither observed in the experiments nor the simulations.

Chapter 9

Conclusion

Self-piercing rivets and self-piercing screws are extensively used by the automotive industry to join aluminium parts in load bearing structures. Finite element simulations are vital in the design process, and the designers are dependent on reliable models. Today, there exist a few models customized for self-piercing rivets but none for self-piercing screws. To improve existing or develop new models, fundamental understanding of the behaviour of the connections is essential. In this thesis, the behaviour of self-piercing screws and self-piercing rivets was investigated through a large number of experiments. Subsequently, numerical models for the material and connections were calibrated, and finite element simulations of all tests were performed, and the results compared to experimental data.

The base material used in this work was a rolled aluminium, 6016 in T4 condition. The self-piercing rivets (5 mm diameter) and self-piercing screws (4 mm diameter) were made of high strength steel and case hardened mild steel, respectively.

Uniaxial tension tests in seven directions, plane strain tension tests in two directions and in-plane single shear tests were performed for the sheet material. An equivalent test program was performed for heat treated material, but the data from these tests was left for later work. Generally, all material tests showed high repeatability.

Cross tests in three loading directions (0, 45 and 90 degrees), single lap-joint tests with two material orientations and peeling tests were performed for rivets and screws. No plastic deformations were observed in the rivets or screws. From the single lap-joint tests, the ductility of the connections with rivets appeared to be dependent of the material orientation of the sheets. The maximum forces using rivets were approximately 50 % higher than for screws, except for in the peeling test. A stiffer overall response of components with rivet connections was observed than with screw connections, due to the large amount of hardening from the riveting process in the bottom sheet. In all tests except the pure normal loading cross test, the rivet failed from the top sheet. The final failure mode was not directly linked to the deformation mode of the rivet. The screws failed from the bottom sheet in all tests, most often by a gradual rotation until pull-out.

Dynamic and static crash box tests were carried out using single-hat section specimens connected to a closing plate using rivets or screws. The same global progressive buckling

mode was observed in all tests, as well as high repeatability for both the force and the mean force. Higher energy absorption in dynamic compared to static tests was mainly explained by inertia effects. Connections were most damaged near the front of the specimens, where the folds were more compressed. An increase of around 4 % was observed for the crash boxes joined with rivets with respect to the ones with screws. A more edged shape of the deformed flanges was found for rivets. Some relative movement between the sheets was observed for the screwed specimens. Deformation and failure modes of the rivets and screws were described. During dynamic tests, 7 % of the screws and 19 % of the rivets failed.

To represent the behaviour of the aluminium sheets, the anisotropic yield function YLD-2004-18P [15] (Barlat) was applied together with the seven parameter Voce isotropic hardening rule and isotropic elasticity. MatPrePost was used to calibrate the constitutive model, using data from the UT tests. For validation, numerical models of the uniaxial tension, plane strain tension and in-plane single shear tests were established and simulations carried out. The results corresponded well with experimental data.

In the preparation of the peeling and crash box test specimens, 90 degree bends were introduced in the sheets. To investigate the effect of the plastic deformations in the bends, the bending process was simulated. Subsequently, the plastic strain field and corresponding hardening terms were mapped into established models of the peeling and crash box specimens.

A large-scale finite element model developed for self-piercing rivets [12] was calibrated for the rivets and screws by a reverse engineering approach. In the calibration procedure, the cross tests in the three directions were simulated and the results compared to the experimental data. The calibrations were validated through simulations of the single lap-joint and peeling tests. For the rivet calibration, the cross tests were well reproduced, and good correspondence was found for the single lap-joint test, but the peeling resistance was massively over-predicted. For screws, a simultaneous fit for the three directions was not achieved. Good correspondence was only obtained for the 0 and 90 degree tests. For the validation, good agreement was obtained for the single lap-joint and peeling tests.

Simulations of the dynamic crash box tests were carried out for three different forming histories, three different yield surfaces (Barlat, von Mises and high exponent) and two mesh sizes (2 mm and 5 mm) in order to investigate the response of the material and point-connector model. The simulations predicted the same global deformation mode as found in the experiments. Except for the initial peak, the force was under-predicted throughout all simulations. A significant increase of mean force was found by including the forming history. Compared to the large shells, small shells predicted slightly better progressive force and deformed shape, while the mean forces were similar. von Mises predicted highest force and the Barlat yield function lowest, which could be related to the yield stress value in the equi-biaxial point. No rivets failed in the simulations, probably due to the high peeling resistance. Fracture of screws was found in all simulations, and the predictions were not equal for different yield surfaces. The computational time was unchanged when including forming history, increased by a factor of 10 from large to small shells, and was doubled using the Barlat compared to von Mises' and the high exponent yield function.

Some considerations regarding future work follows. The point-connector model predicted

good results for rivets, but the peeling resistance should either be reduced, or the peeling test included in the calibration procedure. A more physical prediction of the deformation and fracture mechanisms during bending of the rivet, would probably be obtained if the stiffened part of the bottom sheet was accounted for in the model. For screws, the model was not able to describe a mixed normal and shear loading. For self-piercing screws, modifications of the discussed model or development of a new model is necessary to obtain the required accuracy and reliability. In order to achieve this, a deeper understanding of the fundamental physics and the behaviour of the screws is necessary. It is believed that understanding the fracture mechanisms of the screwed connections is particularly important, as well as analysing the mechanical properties of the screws. Investigations of the effects of the diameter, sheet thickness, sheet material, pre-drilling of top sheet, heat treatment, and dynamic effects are relevant for future work in developing a finite element point-connector model for self-piercing screw connections for use in the automotive industry.

Appendices

Appendix A

Details of experimental setup

A.1 Material tests

The tests were done in accordance with ISO-standards.

Due to a problem with the control panel on the test machine, parts of the material test program had to be performed on another test machine. Hence, two different test setups were used.

In the first test setup a Dartec M 1000 RK 20 kN universal test machine was utilized. An MTS 641.31F-2S extensometer was used with varying gauge lengths according to the test type. An Instron Fast Track 8800 signal amplifier was applied together with an Instron Bluehill logging system which logged force, crosshead displacement and extensometer opening at a logging frequency of 5 Hz.

In the second test setup a Zwick Z030 30 kN universal test machine was used with either a 30 kN or a 5 kN load cell according to the test type. The same extensometer as in setup 1 was used. An HBM Scout 55 amplifier was employed together with a Fluke NetDaq logging system. The same data was logged at the same frequency as in the first test setup.

In the tests UT-WOHT-00-01 through UT-WOHT-75-03 the first test setup was used. In all other material tests the second test setup was used.

A Micromar 40 EW IP65 digital micrometer was employed to measure the exact geometry of the specimens. For the PST and the ISS tests the digital micrometer was incapable of measuring the smallest width of the specimens. Instead a Mahr MarCal 16 EW IP67 digital calliper was used.

A.2 Single connector tests

The riveted C tests were performed using an Instron 8550 100 kN universal biaxial test machine. A Fluke NetDaq logging system was utilized, measuring the load cell force and cross head displacement at a 10 Hz logging frequency. To measure the geometry of the specimens a Marh MarCal 16 EW IP67 digital calliper was employed.

For the screwed C test and all SLJ and P tests a Zwick Z030 30 kN universal test machine with a 30 kN load cell was utilized. An MTS 641.31F-2S extensometer was used with a gauge length of 50 mm. An HBM MVD2555 amplifier was applied together with a Fluke NetDaq logging system which logged force, cross head displacement and extensometer opening at a 10 Hz logging frequency. A Mahr MarCal 16 EW IP67 digital calliper was used to measure the geometry of the specimens, except for the total length where a ruler was used with an assumed accuracy of ± 0.5 mm.

A.3 Component tests

Table A.1: Test setup measurements for the dynamic CB tests.

Specimen name	Nitrogen pressure [bar]	Distance to buffers [mm]	Impact velocity [m/s]	Time to hit buffers [ms]
CB1D-R	6.5	130	9.90	14.20
CB2D-R	6.6	143	9.93	15.60
CB3D-R	6.6	125	9.92	13.53
CB4D-R	6.5	122	9.87	13.40
CB5D-R	6.6	132	9.94	14.40
CB6D-R	6.6	147	9.91	16.13
CB7D-R	6.6	125	9.95	13.53
CB1D-S	6.5	131	9.83	14.20
CB2D-S	6.5	143	9.90	15.20
CB3D-S	6.5	123	9.88	13.33

Appendix B

Geometrical measurements

B.1 Material tests

Table B.1: Measurements before and after UT tests without HT.

Specimen name		Width 1	Width 2	Width 3	Thickness 1	Thickness 2	Thickness 3
UT-WOHT-00-01	*Pre*	5.038	5.035	5.039	1.996	1.992	1.991
	Post	4.665		4.647	1.792		1.783
UT-WOHT-00-02	*Pre*	5.029	5.031	5.027	2.003	2.003	2.002
	Post	4.677		4.666	1.792		1.788
UT-WOHT-00-03	*Pre*	5.034	5.029	5.030	1.991	1.994	1.992
	Post	4.667		4.632	1.790		1.771
UT-WOHT-15-01	*Pre*	5.023	5.023	5.023	2.004	1.998	1.997
	Post	4.719	4.643	4.706	1.766	1.728	1.756
UT-WOHT-15-02	*Pre*	5.030	5.029	5.030	1.995	1.997	1.998
	Post	4.703	4.651	4.735	1.752	1.736	1.763
UT-WOHT-15-03	*Pre*	5.023	5.022	5.022	1.999	2.002	1.995
	Post	4.683	4.651		1.765	1.753	
UT-WOHT-30-01	*Pre*	5.044	5.044	5.046	2.007	2.000	2.000
	Post		4.717	4.753		1.690	1.721
UT-WOHT-30-02	*Pre*	5.046	5.047	5.051	1.998	2.001	2.003
	Post	4.718	4.752	4.777	1.686	1.720	1.751
UT-WOHT-30-03	*Pre*	5.022	5.020	5.021	1.996	1.994	1.994
	Post	4.737	4.687	4.717	1.721	1.685	1.718
UT-WOHT-45-01	*Pre*	5.021	5.024	5.022	1.975	1.972	1.978
	Post	4.757		4.732	1.718		1.710
UT-WOHT-45-02	*Pre*	5.018	5.014	5.014	1.978	1.978	1.980
	Post	4.712	4.714	4.721	1.688	1.697	1.704
UT-WOHT-45-03	*Pre*	5.018	5.018	5.021	1.980	1.982	1.977
	Post	4.755	4.716	4.731	1.707	1.699	1.702
UT-WOHT-60-01	*Pre*	5.028	5.027	5.029	1.984	1.974	1.977
	Post	4.721	4.713		1.730	1.739	
UT-WOHT-60-02	*Pre*	5.015	5.013	5.020	1.973	1.972	1.970
	Post		4.719	4.731		1.728	1.758
UT-WOHT-60-03	*Pre*	5.016	5.018	5.018	1.981	1.989	1.984
	Post	4.723		4.684	1.735		1.717
UT-WOHT-75-01	*Pre*	5.028	5.029	5.028	1.976	1.974	1.977
	Post	4.640	4.538	4.591	1.775	1.741	1.765
UT-WOHT-75-02	*Pre*	5.022	5.022	5.022	1.975	1.976	1.975
	Post		4.560	4.627		1.754	1.772
UT-WOHT-75-03	*Pre*	5.021	5.023	5.027	1.981	1.980	1.978
	Post		4.602	4.641		1.775	1.792
UT-WOHT-90-01	*Pre*	5.030	5.029	5.027	1.980	1.979	1.984
	Post	4.610		4.597	1.814		1.819
UT-WOHT-90-02	*Pre*	5.016	5.027	5.019	1.986	1.988	1.989
	Post	4.531	4.442	4.545	1.805	1.778	1.810
UT-WOHT-90-03	*Pre*	5.015	5.017	5.017	1.990	1.991	1.991
	Post		4.476	4.540		1.792	1.818

Table B.2: Measurements before and after UT tests with HT.

Specimen name		Width 1	Width 2	Width 3	Thickness 1	Thickness 2	Thickness 3
UT-HT-00-01	*Pre*	5.019	5.025	5.024	2.002	2.002	2.003
	Post	4.689	4.609		1.813	1.770	
UT-HT-00-02	*Pre*	5.018	5.017	5.022	1.992	1.996	1.996
	Post	4.677		4.693	1.803		1.815
UT-HT-00-03	*Pre*	5.036	5.041	5.042	1.999	1.995	1.993
	Post		4.619	4.717		1.770	1.800
UT-HT-15-01	*Pre*	5.040	5.041	5.043	1.986	1.984	1.982
	Post	4.715		4.715	1.759		1.765
UT-HT-15-02	*Pre*	5.024	5.023	5.030	1.993	1.992	1.990
	Post		4.662	4.743		1.763	1.786
UT-HT-15-03	*Pre*	5.043	5.042	5.048	1.991	1.993	1.994
	Post		4.646	4.710		1.729	1.780
UT-HT-30-01	*Pre*	5.040	5.029	5.037	1.988	1.983	1.984
	Post	4.737	4.741		1.715	1.718	
UT-HT-30-02	*Pre*	5.020	5.016	5.022	1.995	1.990	1.992
	Post	4.753	4.719		1.736	1.714	
UT-HT-30-03	*Pre*	5.059	5.020	5.028	1.989	1.991	1.989
	Post	4.747	4.710		1.730	1.701	
UT-HT-45-01	*Pre*	5.025	5.025	5.023	2.003	1.991	1.991
	Post		4.763	4.764		1.735	1.739
UT-HT-45-02	*Pre*	5.043	5.046	5.044	1.988	1.986	1.984
	Post		4.751	4.763		1.718	1.716
UT-HT-45-03	*Pre*	5.041	5.042	5.041	1.990	1.988	1.988
	Post	4.767	4.747		1.739	1.711	
UT-HT-60-01	*Pre*	5.026	5.026	5.025	1.980	1.980	1.979
	Post	4.723		4.736	1.744		1.761
UT-HT-60-02	*Pre*	5.038	5.033	5.037	1.982	1.974	1.972
	Post		4.726	4.733		1.751	1.750
UT-HT-60-03	*Pre*	5.022	5.023	5.017	1.984	1.981	1.978
	Post		4.708	4.732		1.743	1.776
UT-HT-75-01	*Pre*	5.049	5.058	5.068	1.978	1.980	1.979
	Post	4.635		4.685	1.781		1.805
UT-HT-75-02	*Pre*	5.017	5.018	5.019	1.980	1.979	1.977
	Post	4.632	4.583		1.793	1.762	
UT-HT-75-03	*Pre*	5.039	5.037	5.046	1.977	1.979	1.978
	Post	4.662		4.688	1.785		1.810
UT-HT-90-01	*Pre*	5.019	5.019	5.017	1.984	1.983	1.987
	Post		4.509	4.598		1.818	1.856
UT-HT-90-02	*Pre*	5.027	5.025	5.028	1.983	1.982	1.981
	Post	4.580		4.623	1.831		1.848
UT-HT-90-03	*Pre*	5.026	5.030	5.031	1.988	1.991	1.989
	Post	4.586		4.645	1.848		1.848

Table B.3: Measurements before and after prestrained UT tests without HT.

Specimen name		Width 1	Width 2	Width 3	Thickness 1	Thickness 2	Thickness 3	ϵ_{nom}
PRE-UT-WOHT-90-03-01	*Pre*	5.015	5.017	5.017	1.980	1.985	1.985	0
	Post	4.951	4.951	4.954	1.967	1.966	1.969	3
PRE-UT-WOHT-90-03-02	*Pre*	5.012	5.012	5.015	1.981	1.983	1.983	0
	Post	4.957	4.947	4.948	1.960	1.965	1.963	3
PRE-UT-WOHT-90-03-03	*Pre*	5.021	5.019	5.021	1.988	1.989	1.990	0
	Post	4.954	4.953	4.958	1.963	1.966	1.969	3
PRE-UT-WOHT-90-06-01	*Pre*	5.015	5.014	5.015	1.985	1.990	1.992	0
	Post	4.865	4.865	4.878	1.946	1.943	1.945	6
PRE-UT-WOHT-90-06-02	*Pre*	5.012	5.012	5.013	1.987	1.988	1.989	0
	Post	4.860	4.860	4.869	1.936	1.936	1.935	6
PRE-UT-WOHT-90-06-03	*Pre*	5.014	5.016	5.017	1.987	1.988	1.991	0
	Post	4.857	4.855	4.858	1.933	1.936	1.932	6
PRE-UT-WOHT-90-10-01	*Pre*	5.013	5.016	5.014	1.984	1.985	1.988	0
	Post	4.773	4.775	4.780	1.902	1.899	1.900	10
PRE-UT-WOHT-90-10-02	*Pre*	5.017	5.019	5.015	1.985	1.986	1.995	0
	Post	4.781	4.757	4.764	1.899	1.900	1.901	10
PRE-UT-WOHT-90-10-03	*Pre*	5.022	5.023	5.031	1.985	1.988	1.987	0
	Post	4.792	4.780	4.792	1.906	1.903	1.904	10

Table B.4: Measurements before and after prestrained UT tests with HT.

Specimen name		Width 1	Width 2	Width 3	Thickness 1	Thickness 2	Thickness 3	ϵ_{nom}
PRE-UT-HT-90-03-01	*Pre*	4.941	4.939	4.949	1.959	1.959	1.961	3
	Post		4.487	4.582		1.793	1.841	-
PRE-UT-HT-90-03-02	*Pre*	4.947	4.942	4.945	1.962	1.955	1.956	3
	Post	4.541		4.561	1.821		1.837	-
PRE-UT-HT-90-03-03	*Pre*	4.953	4.946	4.957	1.962	1.961	1.962	3
	Post	4.554		4.600	1.820	1.840		-
PRE-UT-HT-90-06-01	*Pre*	4.869	4.865	4.882	1.939	1.937	1.944	6
	Post		4.465	4.594		1.791	1.825	-
PRE-UT-HT-90-06-02	*Pre*	4.874	4.864	4.875	1.938	1.937	1.940	6
	Post	4.546		4.596	1.821		1.832	-
PRE-UT-HT-90-06-03	*Pre*	4.857	4.855	4.864	1.935	1.936	1.934	6
	Post	4.503		4.556	1.808		1.814	-
PRE-UT-HT-90-10-01	*Pre*	4.784	4.782	4.785	1.908	1.902	1.905	10
	Post		4.438	4.474		1.774	1.793	-
PRE-UT-HT-90-10-02	*Pre*	4.769	4.765	4.766	1.900	1.900	1.901	10
	Post	4.490		4.486	1.790		1.805	-
PRE-UT-HT-90-10-03	*Pre*	4.782	4.783	4.795	1.908	1.908	1.907	10
	Post		4.425	4.487		1.781	1.787	-

Table B.5: Measurements before PST tests without HT.

Specimen name	Minimum width	Thickness
PST-WOHT-00-01	17.35	1.995
PST-WOHT-00-02	17.35	1.993
PST-WOHT-00-03	17.36	1.997
PST-WOHT-90-01	17.36	1.991
PST-WOHT-90-02	17.29	1.995
PST-WOHT-90-03	17.37	1.995

Table B.6: Measurements before PST tests with HT.

Specimen name	Minimum width	Thickness
PST-HT-00-01	17.36	2.000
PST-HT-00-02	17.33	1.996
PST-HT-00-03	17.39	1.997
PST-HT-90-01	17.34	1.998
PST-HT-90-02	17.35	1.993
PST-HT-90-03	17.38	1.993

Table B.7: Measurements before ISS tests without HT.

Specimen name	Smallest width of shear test area	Thickness
ISS-WOHT-00-01	2.45	1.992
ISS-WOHT-00-02	2.47	1.993
ISS-WOHT-00-03	2.48	2.009
ISS-WOHT-90-01	2.49	1.994
ISS-WOHT-90-02	2.48	1.995
ISS-WOHT-90-03	2.49	1.995

Table B.8: Measurements before ISS tests with HT.

Specimen name	Smallest width of shear test area	Thickness
ISS-HT-00-01	2.46	1.996
ISS-HT-00-02	2.52	1.994
ISS-HT-00-03	2.50	1.990
ISS-HT-90-01	2.46	1.993
ISS-HT-90-02	2.48	1.995
ISS-HT-90-03	2.38	2.002

B.2 Single connector tests

Table B.9: Pre-test measurements of riveted cross tests. The measurements are given in mm and related to Figure 3.11.

Specimen name	Length top sheet	Length bottom sheet	Width top sheet	Width bottom sheet	Measure 1	Measure 2
C-00-R-90-00-01	120.03	120.04	40.16	39.92	60.235	20.115
C-00-R-90-00-02	120.07	119.72	40.06	39.95	59.905	19.835
C-00-R-90-00-03	119.99	119.96	40.04	39.96	59.975	19.935
C-00-R-90-00-04	120.07	119.97	40.06	39.94	60.075	20.005
C-00-R-90-00-05	120.00	119.95	40.09	39.98	59.785	20.095
C-45-R-90-00-01	119.97	120.25	40.19	39.94	59.605	20.045
C-45-R-90-00-02	120.00	119.99	40.22	39.96	59.965	19.905
C-45-R-90-00-03	120.16	120.21	40.07	39.92	60.115	19.975
C-45-R-90-00-04	120.12	120.02	40.06	39.95	59.715	19.795
C-45-R-90-00-05	120.10	120.08	40.20	39.98	59.575	20.245
C-90-R-90-00-01	120.17	119.96	40.22	39.97	59.805	20.205
C-90-R-90-00-02	119.97	119.99	40.16	39.97	59.295	20.675
C-90-R-90-00-03	120.03	119.90	40.20	39.97	60.115	20.145
C-90-R-90-00-04	119.94	120.02	40.05	39.92	59.685	20.025
C-90-R-90-00-05	119.99	120.06	40.06	39.99	60.335	20.055
Average	120.04	120.01	40.12	39.95	59.879	20.070

Table B.10: Pre-test measurements of screwed cross tests. The measurements are given in mm and related to Figure 3.11.

Specimen name	Length top sheet	Length bottom sheet	Width top sheet	Width bottom sheet	Measure 1	Measure 2
C-00-S-90-00-01	120.01	120.03	40.20	40.21	59.50	20.19
C-00-S-90-00-02	120.08	120.08	40.00	40.09	59.70	19.69
C-00-S-90-00-03	120.03	120.12	40.12	40.12	59.92	19.97
C-00-S-90-00-04	120.16	120.03	39.65	40.22	59.91	19.81
C-45-S-90-00-01	120.20	119.94	40.00	40.08	60.02	19.73
C-45-S-90-00-02	120.10	120.06	40.06	40.08	60.36	19.87
C-45-S-90-00-03	120.10	120.03	40.00	40.20	59.44	19.82
C-90-S-90-00-01	120.18	119.92	40.23	40.07	59.68	19.86
C-90-S-90-00-02	120.08	119.98	40.10	40.17	60.10	20.01
C-90-S-90-00-03	120.08	119.99	40.26	40.19	59.66	20.17
C-90-S-90-00-04	120.18	119.95	40.24	40.07	60.16	19.81
C-90-S-90-00-05	120.21	120.02	39.97	40.08	59.67	19.96
C-90-S-90-00-06	120.06	120.03	40.23	40.08	60.00	19.92
Average	120.11	120.01	40.08	40.13	59.86	19.91

Table B.11: Pre-test measurements of riveted SLJ tests. The measurements are given in mm and related to Figure 3.14.

Specimen name	Total length	Width top sheet	Width bottom sheet	Measure 1	Measure 2
SLJ-R-00-00-01	201	40.03	40.05	20.48	19.86
SLJ-R-00-00-02	201	40.07	40.00	21.34	20.44
SLJ-R-00-00-03	201	40.05	40.15	20.50	20.35
SLJ-R-00-00-04	201	40.08	40.04	20.35	20.34
SLJ-R-00-00-05	201	40.04	40.04	19.96	20.36
SLJ-R-90-90-01	200	40.04	40.06	19.51	20.52
SLJ-R-90-90-02	200	40.06	40.30	20.58	19.82
SLJ-R-90-90-03	200	40.17	40.05	20.82	20.02
SLJ-R-90-90-04	200	40.25	40.14	19.95	20.30
SLJ-R-90-90-05	200	40.10	40.17	19.74	19.97
Average	201	40.09	40.10	20.32	20.19

Table B.12: Pre-test measurements of screwed SLJ tests. The measurements are given in mm and related to Figure 3.14.

Specimen name	Total length	Width top sheet	Width bottom sheet	Measure 1	Measure 2
SLJ-S-00-00-01	200	40.17	40.16	19.04	19.63
SLJ-S-00-00-02	200	40.08	40.04	19.89	19.45
SLJ-S-00-00-03	200	40.08	40.08	19.54	19.55
SLJ-S-00-00-04	200	40.20	40.08	19.79	20.04
SLJ-S-00-00-05	200	40.07	40.16	19.85	19.87
SLJ-S-90-90-01	200	40.27	40.27	19.94	20.14
SLJ-S-90-90-02	200	40.18	40.11	19.99	19.95
SLJ-S-90-90-03	200	40.21	40.11	19.63	19.99
Average	200	40.16	40.13	19.71	19.83

Table B.13: Pre-test measurements of riveted peeling tests. The measurements are given in mm and related to Figure 3.16.

Specimen name	Total length	Width top sheet	Width bottom sheet	Measure 1	Measure 2
P-R-90-90-01	167	40.08	40.00	16.34	20.82
P-R-90-90-02	167	40.03	40.05	16.35	20.63
P-R-90-90-03	167	40.03	40.05	15.95	20.47
P-R-90-90-04	167	40.03	39.93	15.31	19.95
P-R-90-90-05	167	40.05	39.99	15.37	19.96
Average	167	40.04	40.00	15.86	20.36

Table B.14: Pre-test measurements of screwed peeling tests. The measurements are given in mm and related to Figure 3.16.

Specimen name	Total length	Width top sheet	Width bottom sheet	Measure 1	Measure 2
P-S-90-90-01	167	40.09	40.11	14.10	20.61
P-S-90-90-02	167	39.92	40.10	14.73	20.23
P-S-90-90-03	167	40.10	40.10	14.28	20.68
Average	167	40.04	40.10	14.37	20.51

B.3 Component tests

Table B.15: Pre-test measurements of riveted crash boxes. The measurements are given in and mm related to Figure 3.18.

Specimen name	Total length	Measure number			
		1	2	3	4
CB1D-R	300	16.78	14.60	14.53	16.45
CB2D-R	301	16.16	15.37	15.80	15.64
CB3D-R	300	16.52	14.63	15.16	17.73
CB4D-R	301	17.36	15.40	15.18	16.75
CB5D-R	300	17.11	14.06	15.23	16.83
CB6D-R	301	17.08	15.21	14.72	18.18
CB7D-R	300	15.18	14.63	15.25	17.22
CB1S-R	301	16.55	15.03	14.53	17.93
CB2S-R	300	19.16	13.83	14.55	17.40
CB3S-R	301	16.50	14.15	15.35	15.29
Average	301	16.84	14.69	15.03	16.94

Table B.16: Pre-test measurements of screwed crash boxes. The measurements are given in mm and related to Figure 3.18.

Specimen name	Total length	Measure number			
		1	2	3	4
CB1D-S	300	14.75	14.95	14.80	15.00
CB2D-S	300	14.80	14.70	15.60	15.25
CB3D-S	300	15.35	14.85	14.65	15.00
CB1S-S	301	15.00	14.60	15.05	15.20
CB2S-S	301	15.00	14.95	15.05	15.15
Average	300	14.98	14.81	15.03	15.12

Table B.17: Buckling mode trigger sizes on crash boxes. The measurements are given in mm and related to Figure 3.19.

Specimen name	Measure number			
	1	2	3	4
CB1D-R	3	3	3	4
CB2D-R	3	3	3	3
CB3D-R	4	4	4	4
CB4D-R	3	4	3	4
CB5D-R	3	3	3	3
CB6D-R	4	3	4	4
CB7D-R	4	4	4	4
CB1S-R	4	4	4	4
CB2S-R	5	4	5	4
CB3S-R	4	4	4	4
CB1D-S	4	4	4	4
CB2D-S	4	4	4	4
CB3D-S	4	4	4	4
CB1S-S	4	5	5	4
CB2S-S	4	5	4	5
Average	3.6	3.8	3.8	3.9

Appendix C

Failure of specimens

C.1 Riveted dynamic component test

Table C.1: Deformation of rivets after dynamic crash box tests.

Rivet name	CB1D-R	CB3D-R	CB4D-R	CB5D-R	CB7D-R
L1	D2	D2	D2	D2	D1, D2
L2	D1, D2	D1	N	N	D1
L3	D1, D3	D1, D3	D1	D1, D3	D1, D3
L4	D1, D3, F1	D1, D3, F1	D2, D3, F1	D1, D3	D1, D3
L5	D1	D1	D1, D3	D1	D1
L6	D1	D1	N	D1, D3	D1, D3
L7	D1	N	N	D1	D1
R1	D1, D2	D1, D2	D1	D2, D3	D2
R2	D1	D1, D3	D1	D1	N
R3	D1	D1	D1, D3	D2, D3	D1, D3
R4	D1, D3, F1	D2	D1, D3, F1	D1, D3	D1, D2, D3
R5	D1	D1	D1	D1	D1
R6	D1	D1	N	D1, D3	D1, D3
R7	N	N	N	D1	D1

C.2 Riveted static component test

Table C.2: Deformation of rivets after quasi-static crash box tests.

Rivet name	CB1S-R	CB2S-R	CB3S-R
L1	D1, D3	D1	D1, D3
L2	D1, D3	D1, D3	D1, D3
L3	D1	N	N
L4	D1, D3	D1, D3	D1, D3
L5	D1	D1	D1
L6	D1, D3	D1, D3	D1
L7	N	D1	D1
R1	D1, D3	D1	D1
R2	D1, D3	D1, D3	D1, D3
R3	D1	N	N
R4	D1, D3	D1, D3	D1, D3
R5	D1	D1	D1, D3
R6	D1, D3	D1, D3	D1
R7	N	D1	D1

C.3 Screwed dynamic component test

Table C.3: Deformation and failure of screws after dynamic crash box tests.

Screw name	CB1D-S	CB2D-S	CB3D-S
L1	N	F1	D1
L2	D1	F3	D1
L3	No head	D1	D1, F2
L4	N	N	N
L5	D1	D1, F2	D1, F1
L6	D1	N	D1
L7	N	D1	N
R1	N	N	F3
R2	D1	D1	D1
R3	D1	D1	D1
R4	N	N	N
R5	D1	F2	D1
R6	D1	D1, F1	D1
R7	N	D1	N

C.4 Screwed static component test

Table C.4: Deformation and failure of screws after quasi-static crash box tests.

Screw name	CB1S-S	CB2S-S
L1	D1	D1
L2	N	N
L3	D1	N
L4	N	D1
L5	D1	N
L6	N	D1
L7	D1	D1
R1	D1	D1, F1
R2	D1	N
R3	N	N
R4	N	D1
R5	No head	N
R6	D1	N
R7	D1	F2

References

[1] A. Tomà, G. Sedlacek, and K. Weinand, "Connections in cold-formed steel," *Thin-walled Structures*, vol. 16, pp. 219–237, 1993.

[2] R. F. Pedreschi and B. P. Sinha, "The potential of press-joining in cold-formed steel structures," *Construction and Building Materials*, vol. 10, pp. 243–250, 1996.

[3] R. Lennon, R. Pedreschi, and B. P. Sinha, "Comparative study of some mechanical connections in cold formed steel," *Construction and Building Materials*, vol. 13, pp. 109–116, 1999.

[4] P. Wung, T. Walsch, A. Ourchane, W. Steward, and M. Jie, "Failure of spot welds under in-plane static loading," *Experimental Mechanics*, vol. 41, pp. 100–106, 2001.

[5] P. Wung, "A force-based failure criterion for spot weld design," *Experimental Mechanics*, vol. 41, pp. 107–113, 2001.

[6] S. H. Lin, J. Pan, S. R. Wu, T. Tyan, and P. Wung, "Failure loads of spot welds under combined opening and shear static loading conditions," *International Journal of Solids and Strucures*, vol. 39, pp. 19–39, 2002.

[7] G. D. Lorenzo and R. Landolfo, "Shear experimental response of new connecting systems for cold-formed structures," *Journal of Constructional Steel Research*, vol. 60, pp. 561–579, 2004.

[8] R. Porcaro, A. G. Hanssen, M. Langseth, and A. Aalberg, "Self-piercing riveting process: An experimental and numerical investigation," *Journal of Materials Processing Technology*, pp. 10–20, 2005.

[9] R. Porcaro, A. G. Hanssen, M. Langseth, and A. Aalberg, "The behaviour of a self-piercing riveted connection under quasi-static loading conditions," *International Journal of Solids and Structures*, pp. 5110–5131, 2006.

[10] R. Porcaro, M. Langseth, A. G. Hanssen, H. Zhao, S. Weyer, and H. Hoopoutra, "Crashworthiness of self-piercing riveted connections," *International Journal of Impact Engineering*, pp. 1251–1266, 2008.

[11] R. Porcaro, A. G. Hanssen, A. Aalberg, and M. Langseth, "Joining of aluminium using self-piercing riveting: Testing, modeling and analysis," *International Journal of Crashworthiness*, pp. 141–154, 2004.

[12] A. G. Hanssen, L. Olovsson, R. Porcaro, and M. Langseth, "A large-scale finite element point-connector model for self-piercing rivet connections," *European Journal of Mechanics A/Solids*, pp. 484–495, 2010.

[13] S. Sommer and J. Maier, "Failure modeling of a self piercing riveted joint using ls-dyna," in *8th European LS-DYNA conference*, 2011.

[14] F. Seeger, M. Feucht, T. Frank, B. Keding, and A. Haufe, "An investigation on spot weld modelling for crash simulation with ls-dyna," in *4. LS-DYNA Anwenderforum, Bamberg*, 2005.

[15] F. Barlat, H. Aretz, J. W. Yoon, M. E. Karabin, J. C. Brem, and R. E. Dick, "Linear-transformation-based anisotropic yield functions," *International Journal of Plasticity*, pp. 1009–1039, 2005.

[16] G. Davies, *Materials for Automobile Bodies*, vol. 1. 200 Wheeler Road, Burlington MA 01803: Elsevier Ltd., 2003.

[17] Audi Service Training, "Self-study programme 456, Audi A8 '10," tech. rep., Audi AG.

[18] Audi Service Training, "Self-study programme 383, Audi TT coupé '07," tech. rep., Audi AG.

[19] Böllhof, "Self-pierce riveting for perfect joints," tech. rep., Böllhof Verbindungstechnik GmbH.

[20] EJOT FDS, "The self piercing and extruding screw for high-strength sheet joints," tech. rep., EJOT.

[21] J. W. D. Callister, *Materials Science and Engineering An Introduction*, vol. 7. Quebecor Versailles: John Wiley & Sons, Inc, 2007.

[22] O. G. Lademo, O. S. Hopperstad, and M. Langseth, "An evaluation of yield criteria and flow rules for aluminium alloys," *International Journal of Plasticity*, vol. 15, pp. 191–208, 1999.

[23] The Aluminum Association, "International alloy designations and chemical composition limits for wrought aluminum and wrought aluminum alloys," tech. rep., The Aluminum Association, Inc.

[24] M. Moore and P. Bate, "Microstructural inhomogeneity and biaxial stretching limits in aluminium alloy AA6016," *Journal of Materials Processing Technology*, vol. 125–126, pp. 258 – 266, 2002.

[25] D. C. Drucker in *Proc. 1st U.S. Natl. Congr. Appl. Mech. New York.*, 1951.

[26] A. Phillips and R. L. Sierakowski, "On the concept of the yield surface," *Acta Mechanica*, vol. 1, pp. 29–35, 1965.

[27] J. F. W. Bishop and R. Hill, "A theory of the plastic distortion of a polycrystalline aggregate under combined stresses," *Philosophical Magazine*, vol. 42, pp. 414–427, 1951.

[28] W. A. Spitzig, R. J. Sober, and O. Richmond, "The effect of hydrostatic pressure on the deformation behavior of maraging and hy-80 steels and its implications for plasticity theory," *Metallurgical Transactions A*, vol. 7A, pp. 1703–1710, 1976.

[29] W. A. Spitzig and O. Richmond, "The effect of pressure on the flow stress of metals," *Acta Metallurgica*, vol. 32, pp. 457–463, 1984.

[30] J. Lubliner, *Plasticity Theory*. Berkeley, CA, USA: Pearson Education, Inc, 2006.

[31] A. G. Hanssen, M. Langseth, and O. S. Hopperstad, "Static and dynamic crushing of circular aluminium extrusions with aluminium foam filler," *International Journal of Impact Engineering*, vol. 24, no. 5, pp. 475 – 507, 2000.

[32] A. G. Hanssen, T. Auestad, T. Tryland, and M. Langseth, "The kicking machine: A device for impact testing of structural components," *International Journal of Crashworthiness*, vol. 8, pp. 385–392, 2003.

[33] V. Tarigopula, M. Langseth, O. S. Hopperstad, and A. H. Clausen, "Axial crushing of thin-walled high-strength steel sections," *International Journal of Impact Engineering*, vol. 32, pp. 847–882, 2006.

[34] M. D. White, N. Jones, and W. Abramowicz, "A theoretical analysis for the quasi-static axial crushing of top-hat and double-hat thin-walled sections," *International Journal of Mechanical Sciences*, vol. 41, pp. 209–233, 1999.

[35] H. Vegter and A. H. v. den Bogaard, "A plane stress yield function for anisotropic sheet material by interpolation of biaxial stress states," *International Journal of Plasticity*, vol. 22, pp. 557–580, 2006.

[36] J. O. Hallquist, *LS-DYNA Theory Manual*. Livermore, CA, USA: Livermore Software Technology Corporation, 2006.